

2

NAVAL POSTGRADUATE SCHOOL

Monterey, California

AD-A236 934



DTIC
ELECTE
JUN 13 1991
S B D

THESIS

EXPERIMENTAL INVESTIGATION OF A
MM-WAVE PLANAR ANTENNA

by

Georgios D. Lambrakakis

June 1990

Thesis Advisor

Ramakrishna Janaswamy

Approved for public release; distribution is unlimited.

91-01873



91 6 11 15M

Unclassified

security classification of this page

REPORT DOCUMENTATION PAGE				
1a Report Security Classification: Unclassified		1b Restrictive Markings		
2a Security Classification Authority		3 Distribution Availability of Report		
2b Declassification Downgrading Schedule		Approved for public release; distribution is unlimited.		
4 Performing Organization Report Number(s)		5 Monitoring Organization Report Number(s)		
6a Name of Performing Organization Naval Postgraduate School	6b Office Symbol (if applicable) 33	7a Name of Monitoring Organization Naval Postgraduate School		
6c Address (city, state, and ZIP code) Monterey, CA 93943-5000		7b Address (city, state, and ZIP code) Monterey, CA 93943-5000		
8a Name of Funding Sponsoring Organization	8b Office Symbol (if applicable)	9 Procurement Instrument Identification Number		
8c Address (city, state, and ZIP code)		10 Source of Funding Numbers		
		Program Element No	Project No	Task No Work Unit Accession No
11 Title (include security classification) EXPERIMENTAL INVESTIGATION OF A MM-WAVE PLANAR ANTENNA				
12 Personal Author(s) Georgios D. Lambrakakis				
13a Type of Report Master's Thesis	13b Time Covered From To	14 Date of Report (year, month, day) June 1990	15 Page Count 138	
16 Supplementary Notation The views expressed in this thesis are those of the author and do not reflect the official policy or position of the Department of Defense or the U.S. Government.				
17 Cosatt Codes		18 Subject Terms (continue on reverse if necessary and identify by block number)		
Field	Group	Subgroup	thesis, word processing, Script, GML, text processing.	
19 Abstract (continue on reverse if necessary and identify by block number) This thesis investigates a new mm-wave Bilateral Slot Line (BSL) antenna and its relation to the Linearly Tapered Slot Antenna (LTSA). The BSL antenna consists of a tapered double-sided slotline and can be viewed as two identical LTSAs sandwiched back to back. Dielectric substrates with permittivities of 2.33 and 6.0 were used to construct these antennas. The theoretical background, the design, and the performance in the frequency range 5-9 GHz of the new microwave integrated circuit antenna is presented. The effects of several parameters such as dielectric constant, stripline and slotline characteristic impedance, antenna structure, and transition scheme on the radiation patterns and return loss were experimentally investigated. Some relationships between the width of stripline and slotline, their characteristic impedance and the dielectric constant are reported. Guidelines are laid down to design the LTSA and BSL antennas.				
20 Distribution Availability of Abstract <input checked="" type="checkbox"/> unclassified unlimited <input type="checkbox"/> same as report <input type="checkbox"/> DTIC users		21 Abstract Security Classification Unclassified		
22a Name of Responsible Individual Ramakrishna Janaswamy		22b Telephone (include Area code) (408) 646-3217	22c Office Symbol EC/Js	

Approved for public release; distribution is unlimited.

Experimental investigation of a mm-wave planar antenna

by

Georgios D. Lambrakakis
Lieutenant , Hellenic Navy
B.S., Naval Academy, 1980

Submitted in partial fulfillment of the
requirements for the degree of

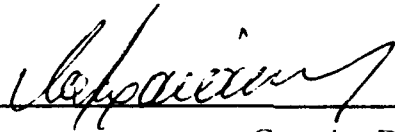
MASTER OF SCIENCE IN ELECTRICAL AND COMPUTER ENGINEERING

from the

NAVAL POSTGRADUATE SCHOOL

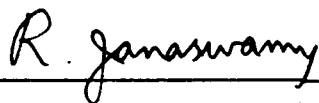
June 1990

Author:

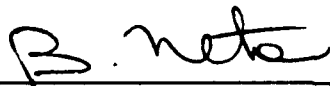


Georgios D. Lambrakakis

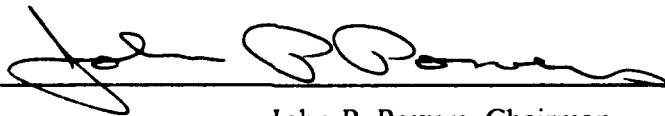
Approved by:



Ramakrishna Janaswamy, Thesis Advisor



Beny Neta, Second Reader



John P. Powers, Chairman,
Department of Electrical and Computer Engineering

ABSTRACT

This thesis investigates a new mm-wave Bilateral Slot Line (BSL) antenna and its relation to the Linearly Tapered Slot Antenna (LTSA). The BSL antenna consists of a tapered double-sided slotline and can be viewed as two identical LTSAs sandwiched back to back. Dielectric substrates with permittivities of 2.33 and 6.0 were used to construct these antennas. The theoretical background, the design, and the performance in the frequency range 5-9 GHz of the new microwave integrated circuit antenna is presented. The effects of several parameters such as dielectric constant, stripline and slotline characteristic impedance, antenna structure, and transition scheme on the radiation patterns and return loss were experimentally investigated. Some relationships between the width of stripline and slotline, their characteristic impedance and the dielectric constant are reported. Guidelines are laid down to design the LTSA and BSL antennas.

Accession For	
NTIS GRA&I	<input checked="" type="checkbox"/>
DTIC TAB	<input type="checkbox"/>
Unannounced	<input type="checkbox"/>
Justification _____	
By _____	
Distribution/	
Availability Codes	
Dist	Avail and/or Special
A-1	



TABLE OF CONTENTS

I. INTRODUCTION	1
A. BACKGROUND	1
II. REVIEW OF CHARACTERISTICS OF END-FIRE TAPERED SLOT AN- TENNA ELEMENT	5
A. BEAMWIDTH, GAIN, DIRECTIVITY	5
B. IMPEDANCE	7
III. COMPUTING CHARACTERISTIC IMPEDANCE	8
A. STRIPLINE CHARACTERISTIC IMPEDANCE	8
B. BILATERAL SLOT LINE CHARACTERISTIC IMPEDANCE	16
IV. DESIGN OF LINEAR TAPERED SLOT ANTENNA AND BILATERAL SLOT LINE ANTENNA	35
A. BACKGROUND	35
B. ANTENNAS ON $\epsilon_r = 6.0$ SUBSTRATE	36
C. ANTENNAS ON $\epsilon_r = 2.22$ SUBSTRATE	38
D. ANTENNA NO.3	39
E. LAUNCHING METHOD	42
F. ANTENNA CONSTRUCTION	42
V. ANALYSIS OF MEASUREMENTS	52
A. BACKGROUND	52
B. EFFECT OF DIELECTRIC CONSTANT AND ANTENNA STRUCTURE	56
1. LTSA	56
2. LTSA, BSL Antenna	69
3. BSL ANTENNA	73
C. EFFECT OF CHARACTERISTIC IMPEDANCE	73
VI. SUMMARY AND CONCLUSION	80

APPENDIX A. LTSA AND BSL ANTENNA RADIATION PATTERNS	82
APPENDIX B. FORTRAN PROGRAM TO CALCULATE THE CHARACTERISTIC IMPEDANCE OF STRIPLINE	123
LIST OF REFERENCES	124
INITIAL DISTRIBUTION LIST	126

LIST OF TABLES

Table 1. DESIGN DATA 41

LIST OF FIGURES

Figure 1. Three types of end-fire tapered slot antennas	3
Figure 2. Configuration of the BSL antenna	4
Figure 3. E-field and the H-field within stripline and bilateral slot line	11
Figure 4. Stripline characteristic impedance versus ϵ_r	12
Figure 5. Stripline characteristic impedance versus $W_{ST}/2d$, for $1.0 \leq W_{ST}/2d \leq 10.0$	13
Figure 6. Stripline characteristic impedance versus $W_{ST}/2d$, for $0.1 \leq W_{ST}/2d \leq 1.0$	14
Figure 7. Plot of $Z_{ST}\sqrt{\epsilon_r}$ versus $W_{ST}/2d$	15
Figure 8. Configuration of BSL and simplified BSL	17
Figure 9. Coordinate transformation	18
Figure 10. Bilateral slotline characteristic impedance versus $\sqrt{\epsilon_r - 1} \frac{d}{\lambda_o}$	29
Figure 11. Plot of ϵ_{eff} versus $\sqrt{\epsilon_r - 1} \frac{d}{\lambda_o}$	30
Figure 12. Bilateral slotline characteristic impedance versus $\sqrt{\epsilon_r - 1} \frac{d}{\lambda_o}$	31
Figure 13. Dispersion characteristic of bilateral slotline for $\epsilon_r = 6.0$	32
Figure 14. Comparison of ϵ_{eff} between BSL and single-sided slotline	33
Figure 15. Comparison of Z_o between BSL and single-sided slotline	34
Figure 16. Geometry of antenna No.1	44
Figure 17. Stripline characteristic impedance versus $W_{ST}/2d$ for impedance near 50 ohm and $\epsilon_r = 6.0$	45
Figure 18. Slotline characteristic impedance versus W_{BSL}/d for impedance near 70 ohm and $\epsilon_r = 6.0$	46
Figure 19. Slotline characteristic impedance versus W_{BSL}/d for impedance near 50 ohm and $\epsilon_r = 2.22$	47
Figure 20. Slotline characteristic impedance versus W_{BSL}/d for impedance near 50 ohm and $\epsilon_r = 6.0$	48
Figure 21. Cross sectional view of the coaxial line to stripline transition.	49
Figure 22. (A) Positive mask of slotline, and (B) positive mask of stripline for antenna No.3.	50
Figure 23. Geometry of antenna No.3C	51
Figure 24. Total return loss TDR of antenna No.2C	54
Figure 25. Return loss TDR of antenna No.2C due to reflections at the junction of the stripline and the BSL	55

Figure 26. 3-dB beamwidth and side lobe level (S.L.L.) as a function of frequency .	58
Figure 27. Total return loss (FDR) as a function of frequency	59
Figure 28. Total return loss (TDR) as a function of frequency	60
Figure 29. 3-dB beamwidth and side lobe level (S.L.L.) as a function of frequency .	61
Figure 30. Total return loss for antenna No. 1B	62
Figure 31. Total return loss (FDR) as a function of frequency	63
Figure 32. Total return loss (TDR) as a function of frequency	64
Figure 33. Return loss due to junction alone as a function of frequency	66
Figure 34. 3-dB beamwidth and side lobe level (S.L.L.) as a function of frequency .	67
Figure 35. Total return loss (A) and return loss due to junction only (B) as a function of frequency	68
Figure 36. 3-dB beamwidth and side lobe level (S.L.L.) as a function of frequency .	70
Figure 37. 3-dB beamwidth and side lobe level (S.L.L.) as a function of frequency .	71
Figure 38. 3-dB beamwidth as a function of frequency	72
Figure 39. 3-dB beamwidth and side lobe level (S.L.L.) as a function of frequency .	75
Figure 40. 3-dB beamwidth and side lobe level (S.L.L.) as a function of frequency .	76
Figure 41. 3-dB beamwidth and side lobe level (S.L.L.) as a function of frequency .	77
Figure 42. FDR plots for antenna No.3C	78
Figure 43. TDR plots for antenna No.3C	79
Figure 44. Radiation patterns of antenna No.1A at 5 GHz	83
Figure 45. Radiation patterns of antenna No.1A at 6 GHz	84
Figure 46. Radiation patterns of antenna No.1A at 7 GHz	85
Figure 47. Radiation patterns of antenna No.1A at 8 GHz	86
Figure 48. Radiation patterns of antenna No.1A at 9 GHz	87
Figure 49. Radiation patterns of antenna No.1B at 5 GHz	88
Figure 50. Radiation patterns of antenna No.1B at 6 GHz	89
Figure 51. Radiation patterns of antenna No.1B at 7 GHz	90
Figure 52. Radiation patterns of antenna No.1B at 8 GHz	91
Figure 53. Radiation patterns of antenna No.1B at 9 GHz	92
Figure 54. Radiation patterns of antenna No.1CO at 5 GHz	93
Figure 55. Radiation patterns of antenna No.1CO at 6 GHz	94
Figure 56. Radiation patterns of antenna No.1CO at 7 GHz	95
Figure 57. Radiation patterns of antenna No.1CO at 8 GHz	96
Figure 58. Radiation patterns of antenna No.1CO at 9 GHz	97
Figure 59. E-plane and H-plane radiation patterns of antenna No.1C at 5 GHz . .	98

Figure 60. E-plane and H-plane radiation patterns of antenna No.1C at 6 GHz	.. 99
Figure 61. E-plane and H-plane radiation patterns of antenna No.1C at 7 GHz	. 100
Figure 62. E-plane and H-plane radiation patterns of antenna No.1C at 8 GHz	. 101
Figure 63. E-plane and H-plane radiation patterns of antenna No.1C at 9 GHz	. 102
Figure 64. Radiation patterns of antenna No.2A at 5 GHz 103
Figure 65. Radiation patterns of antenna No.2A at 6 GHz 104
Figure 66. Radiation patterns of antenna No.2A at 7 GHz 105
Figure 67. Radiation patterns of antenna No.2A at 8 GHz 106
Figure 68. Radiation patterns of antenna No.2A at 9 GHz 107
Figure 69. Radiation patterns of antenna No.2B at 5 GHz 108
Figure 70. Radiation patterns of antenna No.2B at 6 GHz 109
Figure 71. Radiation patterns of antenna No.2B at 7 GHz 110
Figure 72. Radiation patterns of antenna No.2B at 8 GHz 111
Figure 73. Radiation patterns of antenna No.2B at 9 GHz 112
Figure 74. Radiation patterns of antenna No.2C at 5 GHz 113
Figure 75. Radiation patterns of antenna No.2C at 6 GHz 114
Figure 76. Radiation patterns of antenna No.2C at 7 GHz 115
Figure 77. Radiation patterns of antenna No.2C at 8 GHz 116
Figure 78. Radiation patterns of antenna No.2C at 9 GHz 117
Figure 79. Radiation patterns of antenna No.3C at 5 GHz 118
Figure 80. Radiation patterns of antenna No.3C at 6 GHz 119
Figure 81. Radiation patterns of antenna No.3C at 7 GHz 120
Figure 82. Radiation patterns of antenna No.3C at 8 GHz 121
Figure 83. Radiation patterns of antenna No.3C at 9 GHz 122

ACKNOWLEDGEMENT

I would like to give special thanks to Professor R. Janaswamy, who guided me from the beginning of this work; Professor B. Neta whose comments and criticism helped to complete this thesis; Mr Joseph Mosko and his staff for helping me to carry out the experiment; Lt D. Dariotis HN and Lt C. Cameron USN.

I would also like to dedicate this thesis to my wife, Vasso, and my daughter, Maria, who encouraged me from the beginning.

Finally, I wish to thank the Hellenic Navy for providing the opportunity to study at NPS.

I. INTRODUCTION

In recent years planar microwave integrated circuits have found wide applications in mm-wave and microwave subsystems. Some of their advantages are light weight, compatibility with integrated circuits, ease of mounting on aircraft and spacecraft, and compact size. [Ref. 1: p. 525]

A. BACKGROUND

The wideband microwave and millimeter-wave antennas belong to the class of travelling wave antenna. The travelling-wave antennas are divided into two main groups called the 'leaky-wave antennas' and the 'surface-wave antennas' [Ref. 2: p. 1393]. In the first type, the antenna structure propagates a travelling-wave with a phase velocity v_{ph} greater than the speed of light, and the main beam occurs in the direction different from endfire. On the other hand, the 'surface-wave antenna' propagates a travelling wave with a phase velocity less than the speed of light in vacuum, $v_{ph} \leq c$. This kind of antenna produces endfire radiation. [Ref. 2: p. 1393]

The present research is focused on the (end-fire) Linear Tapered Slot Antenna (LTSA) [Ref. 3: p. 365] and on the Bilateral Slot Line (BSL) antenna [Ref. 4: p. 2]. The latter is a new antenna which was recently introduced to the family of 'surface-wave' antennas. An example of 'leaky-wave antennas' is the logarithmic-periodic spiral antenna [Refs. 5, 6]. The Tapered Slot Antenna (TSA) [Ref. 2: p. 1392] is an example of 'surface-wave' antenna.

A TSA has a tapered slot of thin metal on one side of a dielectric substrate. Figure 1 illustrates three TSAs with different taper shapes, the LTSA [Refs. 1, 3], CWSA (Constant Width Slot Antenna) [Ref. 3: p. 1393], and the Vivaldi antenna [Ref. 7: p. 101]. Figure 2 shows the Bilateral Slot Line antenna, that has two identical slots on the opposite sides of a dielectric substrate and arranged one on top of the other without any lateral displacement [Ref. 4: p. 2].

TSAs have important advantages which make them popular in several applications:

- Narrow beamwidth (3-dB beamwidth close to 15° and 10-dB beamwidth close to 30°) [Ref. 3: p. 365].
- High antenna gain [Ref. 3: p. 365].
- Wider bandwidth than the typical broadside antenna (log-periodic and spiral type antennas are not included). [Ref. 3: p. 366]

- Very inexpensive to fabricate. [Ref. 3: p. 366]
- Little impedance variation with respect to the frequency. Also they could be relatively easy integrated with other components in microwave integrated circuits [Ref. 1: p. 525].

The primary research questions to be addressed in this research are:

- Can wide-band feeding structures be designed to feed the tapered slot antenna?
- Can alternate structures and accompanying feed networks be devised for the tapered slot antenna?
- If alternate structures could be found, can guidelines be laid down to design the antennas?

Chapter 1 gives an overview of characteristics of the tapered-slot antenna element and introduces the BSL antenna. In Chapter 2 we explain in detail the design procedure to compute the characteristic impedance of stripline and bilateral slotline. Using data from Chapter 3 and some empirical relations from Chapter 2, we proceed step by step to design the antennas that we are going to examine. The procedure is summarized in Chapter 4. Chapter 5 focuses on the analysis of the experimental results. Finally Chapter 6 summarizes the conclusions of the investigation.

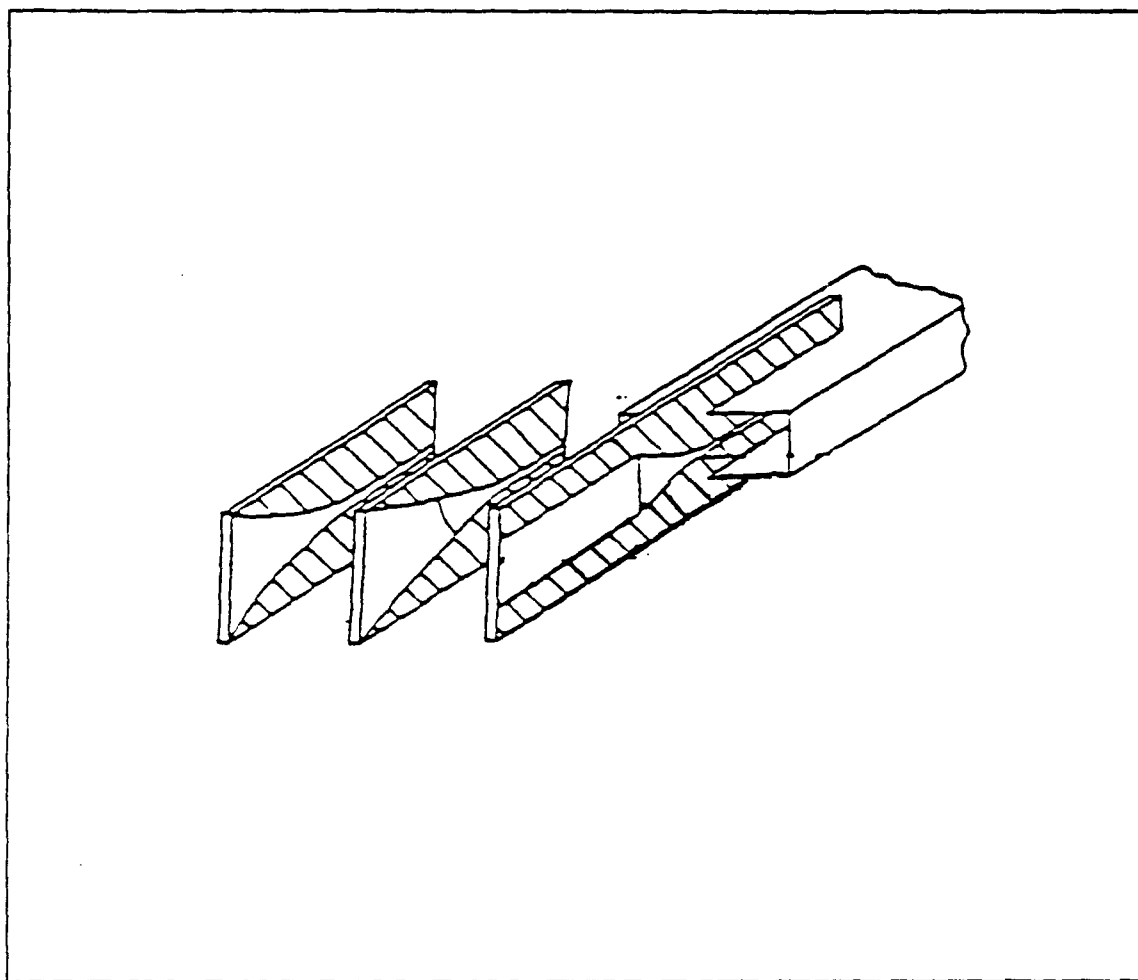


Figure 1. Three types of end-fire tapered slot antenna: From left to right Vivaldi, LTSA, CWSA. From [Ref. 2: p. 1392]

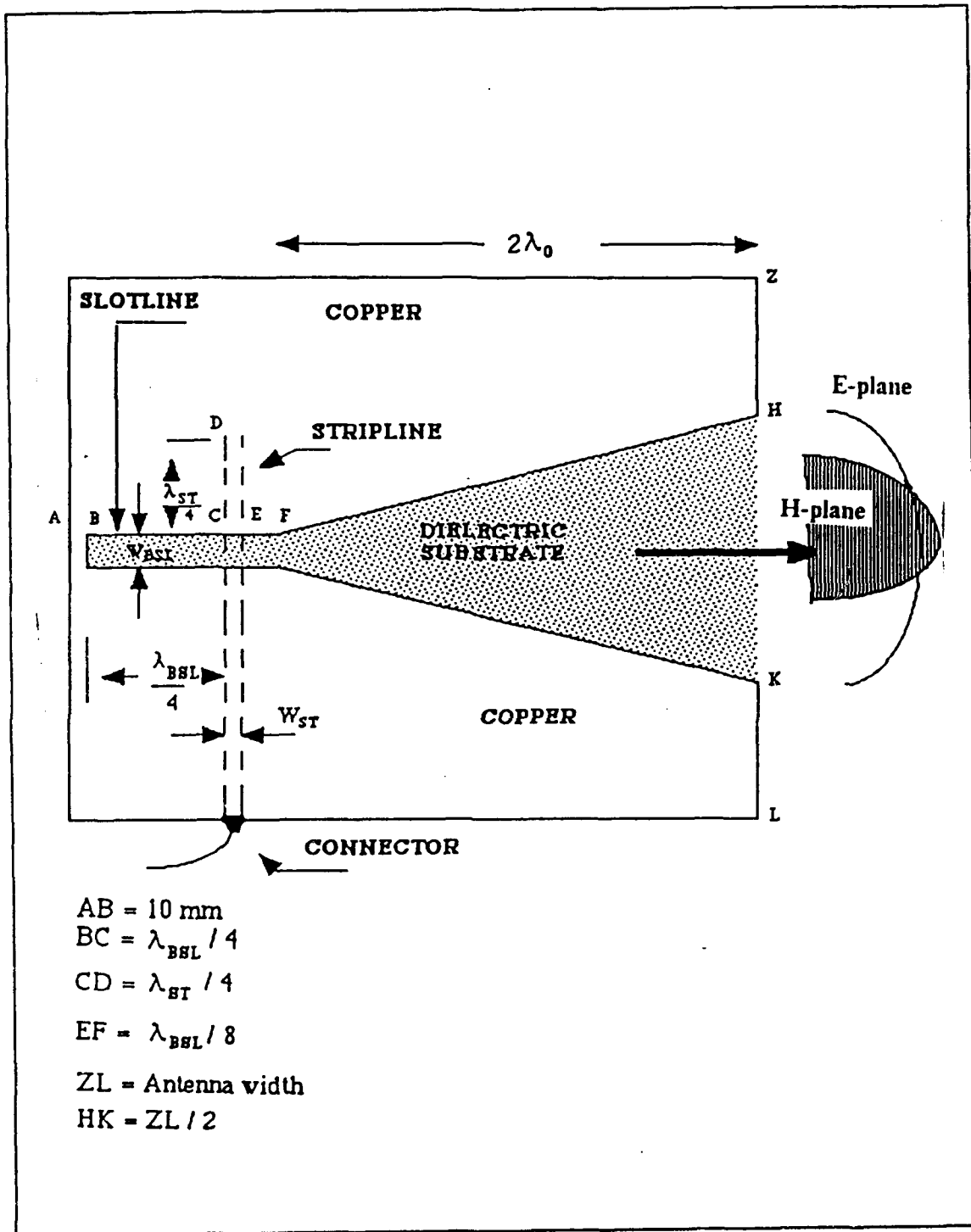


Figure 2. Configuration of the BSL antenna

II. REVIEW OF CHARACTERISTICS OF END-FIRE TAPERED SLOT ANTENNA ELEMENT

As mentioned in the previous Chapter, the TSA belongs to the class of slow-wave (surface-wave) travelling wave antennas. In this Chapter we will give discuss the salient features of the tapered slot antenna.

A. BEAMWIDTH, GAIN, DIRECTIVITY

The classic Tapered Slot Antenna (TSA) produces fairly symmetric radiation patterns having approximately equal beamwidths in the E-plane and the H-planes. The above symmetry of radiation pattern is independent of antenna symmetry, but the beam pattern becomes asymmetric and the level of side lobes increases as the substrate thickness increases. Figure 2 depicts the cross-sectional view and the E-plane and H-plane of a LTSA and BSL antenna.[Ref. 2: p. 1392, and Ref. 3: pp. 366-377]

There is a good agreement between theory and experiment for thin dielectric substrates in the case where the substrate thickness $2d$ normalized to free space wave length is nearly 0.05 and for substrate permittivities less than 3. As substrates becomes thicker (especially for substrates with high permittivity), we will expect less agreement between theory and experiment. [Ref. 6: p. 376, and Ref. 8]

According to the theory of travelling wave antennas, the beamwidth becomes narrow and the directivity increases as the length of the antenna increases [Refs. 3, 6, 7]. Also we can expect a 3-dB beamwidth varying from 50° to 20° for effective radiating lengths from $2\lambda_0$ to $12\lambda_0$ [Ref. 9: p. 1].

The tapered slot antenna can viewed as a flared slotline. The characteristic impedance Z_{SL} of a slotline increases with the slot width. The slotline behaves as a transmission line if the slotline width is less than about $0.4\lambda_0$, where λ_0 is the free-space wavelength [Ref. 1: p. 525, and Ref. 10]. The TSAs are developed by increasing the width of slotline gradually (linearly, exponentially or combination of these two) from the feed-end point so that, at the open-end (mouth of slot), the slot width becomes greater than $0.4\lambda_0$, consequently allowing the slotline to radiate [Ref. 1: p. 525]. Reference 3 states that, for effective radiation to occur, the slot width W_{ST} at the open-end should be at least one-half of a free-space wavelength. Consequently, at low frequencies, the radiation from the antenna will be interrupted or reduced, while at high frequencies, the

antenna performance is limited by the substrate thickness d . The thickness should be much smaller than a quarter of wavelength [Ref. 9: p. 1]:

$$d < \frac{\lambda_o}{4\sqrt{\epsilon_r - 1}} \quad (1)$$

We also note from [Ref. 3: p. 366] that, for the LTSA, the directivity increases and the beamwidth decreases as the total antenna length L normalized to the free-space wavelength, λ_o , increases.

A useful term, the effective dielectric thickness, d_{eff} , of the substrate normalized to the free-space wavelength λ_o , was coined by the author of [Ref. 3: p. 366], and is defined as:

$$\frac{d_{eff}}{\lambda_o} = \sqrt{(\epsilon_r - 1)} \frac{d}{\lambda_o} \quad (2)$$

where d is the actual substrate thickness. As the effective thickness of the antenna decreases, the beamwidth increases and vice versa [Ref. 3: p. 360]. The substrate plays the role of support for the antenna. Substrate permittivity has a big influence on the E-plane and H-plane patterns. As a rule of thumb, it is easier to obtain an acceptable antenna performance by using substrates with a small thickness or low permittivity [Ref. 6: pp. 375-377].

So far there is no design information for slotlines having 50 ohm characteristic impedance on low-permittivity substrates. The present research is going to investigate the use of 50 ohm slotline on low-permittivity substrates.

Reference 5 dealing with Vivaldi antenna reports that the H-plane beamwidth decreases approximately linearly with the reciprocal square root of the antenna length L , while E-plane beamwidth decreases approximately linearly with the reciprocal of the mouth width of the antenna, and, for certain flare angle ($2\alpha = 8.4^\circ$), the beamwidths are approximately equal to 20° . Typical LTSAs have flare angle 2α varying in the range 5° - 12° . The H-plane beamwidth is more or less independent of the flare angle 2α , while the E-plane beamwidth narrows as the flare angle increases [Ref. 3: p. 367 and 9: p. 2].

Comparing different TSAs on the same substrate and having the same antenna aperture and length, the beamwidth is narrowest for the CWSA, followed by the LTSA, and then the Vivaldi. Also, the sidelobes are highest for CWSA, followed by the LTSA, and the Vivaldi. [Ref. 3: p. 367]

B. IMPEDANCE

The calculation of impedance at the feed point and the input impedance of an infinite coplanar biconical structure without dielectric was first developed by R. Carrel in 1958 using the conformal mapping technique [Ref. 11]. Reference 2 stated that in general there is a good agreement between measured data for typical LTSA and the above theory. The good agreement, for impedance, between [Ref. 11] (a TSA without dielectric) and [Ref. 2: p. 1398] (a LTSA with dielectric) is based on the fact that the substrate used was very thin (0.13 mm). As a matter of fact, a LTSA antenna with a thin dielectric has impedance which is essentially frequency independent and the conformal mapping method is also valid for a TSA with a thin substrate [Ref. 2: p. 1398]. Also [Refs. 2, 3] predicted that the detailed shape of the feed region of LTSA is unlikely to change the impedance much. Typical impedances of TSAs are in the neighborhood of 80 ohms. The fact that the impedance remains almost constant makes the TSA increasingly popular in the mm-wave community [Ref. 3: p. 367].

Recently, the spectral domain analysis (Spectral Galerkin's method) was utilized by R. Janaswamy [Ref. 4: p. 1] to analyze the even mode in a bilateral slotline. The slot width required to produce 80 ohms on low dielectric constant substrates is extremely narrow leading to fabrication difficulties. To overcome this, we have fabricated the antennas using bilateral slotline which would result in wider slots. More details of bilateral slotline characteristics are given in Chapter 3.

III. COMPUTING CHARACTERISTIC IMPEDANCE

A. STRIPLINE CHARACTERISTIC IMPEDANCE

An extremely useful guide for computing the stripline characteristic impedance Z_{ST} is the paper written by I.J. Bahl and R. Garg [Ref. 12]. In this section, the method to compute Z_{ST} is outlined and data for the stripline characteristic impedance is presented. A stripline consists of a strip conductor which is placed between two conducting ground planes and filled with dielectric. The purpose of the conducting ground planes is to restrict the field which is created by exciting the center strip conductor. Dielectric is used to reduce the physical size of transmission line for any operating frequency. [Ref. 12: p. 90]

The stripline of Fig. 3A propagates a transverse electromagnetic mode (TEM) since field lines between strip and ground are contained entirely in the dielectric substrate. The bilateral slot line shown in Fig. 3B propagates a non-TEM mode. The phase velocity v is the speed with which the phase of the wave travels in the direction of propagation and is given by the following equations [Ref. 12: p. 90]

$$v = \frac{c}{\sqrt{\epsilon_r}} = c \frac{\lambda_{ST}}{\lambda_0} \quad (3)$$

where ϵ_r is the dielectric constant relative to air of the medium between the two copper conductors and $c = 3 \times 10^8$ m/sec is the velocity of light in vacuum.

The characteristic impedance for the TEM mode is defined as

$$Z_{ST} = \frac{1}{vC} \quad (4)$$

where C is the capacitance per unit length of the stripline.

Cohn [Ref. 13], using a conformal mapping technique, derived an equation for stripline capacitance with zero strip thickness and obtained a very accurate equation for the characteristic impedance:

$$Z_{ST} = \frac{30\pi}{\sqrt{\epsilon_r}} \frac{K(k)}{K'(k)} \text{ ohms} \quad (5)$$

where $k = \text{sech}\left(\frac{\pi}{2} \frac{W_{ST}}{2d}\right)$ and $k' = \tanh\left(\frac{\pi}{2} \frac{W_{ST}}{2d}\right)$, $2d$ is the plate spacing, and W_{ST} is the stripline width. The function $K(k)$ is a complete elliptic function of the first kind given by [Ref. 14]

$$K(k) = \int_0^{\frac{\pi}{2}} \frac{dx}{\sqrt{1 - k^2 \sin^2 x}} \quad (6)$$

and $K'(k)$ is the complementary function given by

$$K'(k) = K(k') = K(\sqrt{1 - k^2}), \quad \text{or} \quad (7)$$

$$K(k') = \int_0^{\frac{\pi}{2}} \frac{dx}{\sqrt{1 - k'^2 \sin^2 x}} \quad (8)$$

Reference 12 derived an accurate expression for the ratio $\frac{K(k)}{K'(k)}$ with accuracy of 8 ppm. It is given by

$$\frac{K(k)}{K'(k)} = \left[\frac{1}{\pi} \ln \left(\frac{2(1 + \sqrt{k'})}{1 - \sqrt{k'}} \right) \right]^{-1} \quad \text{for } 0 \leq k \leq 0.7 \quad (9)$$

and

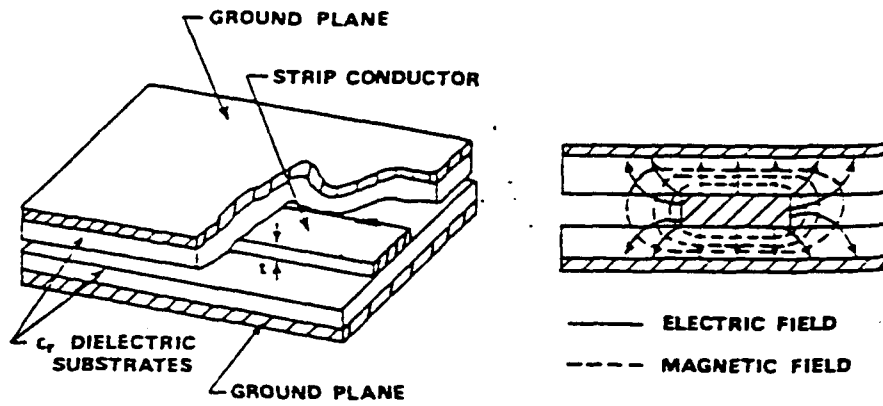
$$\frac{K(k)}{K'(k)} = \frac{1}{\pi} \ln \left(2 \frac{1 + \sqrt{k}}{1 - \sqrt{k}} \right) \quad \text{for } 0.7 < k \leq 1.0 \quad (10)$$

Since we are going to use thin conductor for the stripline, the assumption that the strip thickness is zero is valid. The above formulas are used to develop the stripline characteristics. Similar design guidelines for thick stripline of non-zero conductor thickness are also given in the same reference.

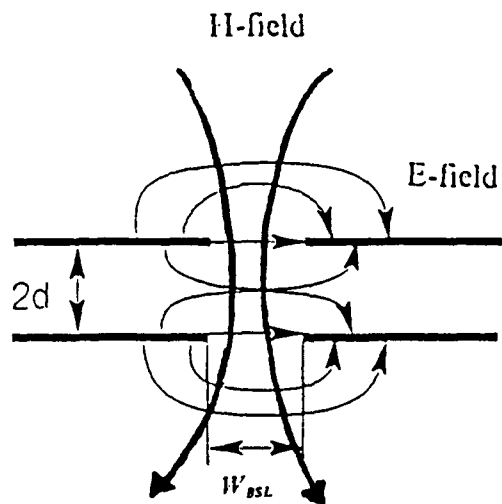
A computer program was developed to calculate the stripline characteristic impedance for some most commonly encountered dielectric substrates of $\epsilon_r = 2, 3, 4, 5, 6, 7, 8, 9,$ and 10 . The results are plotted in Figs. 4 through 7 in such a way as to enable a designer to easily extract accurate data. (The notation ER on Fig. 6 stands for ϵ_r).

Figure 4 illustrates the effects of changing the dielectric constant on the characteristic impedance for some specific values of $\frac{W_{ST}}{2d} = 0.1, 0.2, 1.0, 2.0, 5.0,$ and 10.0 . One should note that for a given $\frac{W_{ST}}{2d}$ the stripline characteristic impedance Z_{ST} decreases as the dielectric constant increases. Also one notes that the rate of change of characteristic impedance is larger for $\frac{W_{ST}}{2d} \leq 1.0$ (Fig. 6), while for $\frac{W_{ST}}{2d} \geq 1.0$ (Fig. 5), the change becomes smaller and reaches an asymptotic value beyond $\frac{W_{ST}}{2d} = 5.0$. Moreover the difference in characteristic impedance between two substrates having $\frac{W_{ST}}{2d} \geq 5.0$ is negligible. For example, a substrate with $\frac{W_{ST}}{2d} = 5.0$ has $Z_{ST} = 10$ ohms, while a second substrate with $\frac{W_{ST}}{2d} = 10.0$ has $Z_{ST} = 9.5$ ohm.

Figure 5 shows the effects of changing the ratio $\frac{W_{ST}}{2d}$ on the characteristic impedance for $\epsilon_r = 2, 3, 4, 5, 6, 7, 8, 9,$ and 10 . We can see that the maximum impedance that one can achieve is 46 ohm and occurs when $\epsilon_r = 2.0$ and $\frac{W_{ST}}{2d} = 1.0$. Since most striplines have characteristic impedance in the range $50 \text{ ohms} \leq Z_{ST} \leq 80 \text{ ohms}$, the ratio $\frac{W_{ST}}{2d}$ should be less than 1.0, as illustrated in Fig. 6. It is seen, for the above region of Z_{ST} , that for a dielectric constant $\epsilon_r = 2.22$, we have $0.4 \leq \frac{W_{ST}}{2d} \leq 0.9$. For higher permittivity, the corresponding region of $\frac{W_{ST}}{2d}$ becomes narrower. For $\epsilon_r = 10$, we have $0.1 \leq \frac{W_{ST}}{2d} \leq 0.18$. Variation of $Z_{ST}\sqrt{\epsilon_r}$ versus $\frac{W_{ST}}{2d}$ is shown in Fig. 7. From Fig. 7 one can observe that the maximum value of $Z_{ST}\sqrt{\epsilon_r}$ is 66 ohms for $\frac{W_{ST}}{2d} = 1.0$.



(A). Geometry of stripline. From [Ref. 12: p. 90]



(B). Geometry of the bilateral slot line. After [Ref. 15]

Figure 3. E-field and the H-field within stripline and bilateral slot line

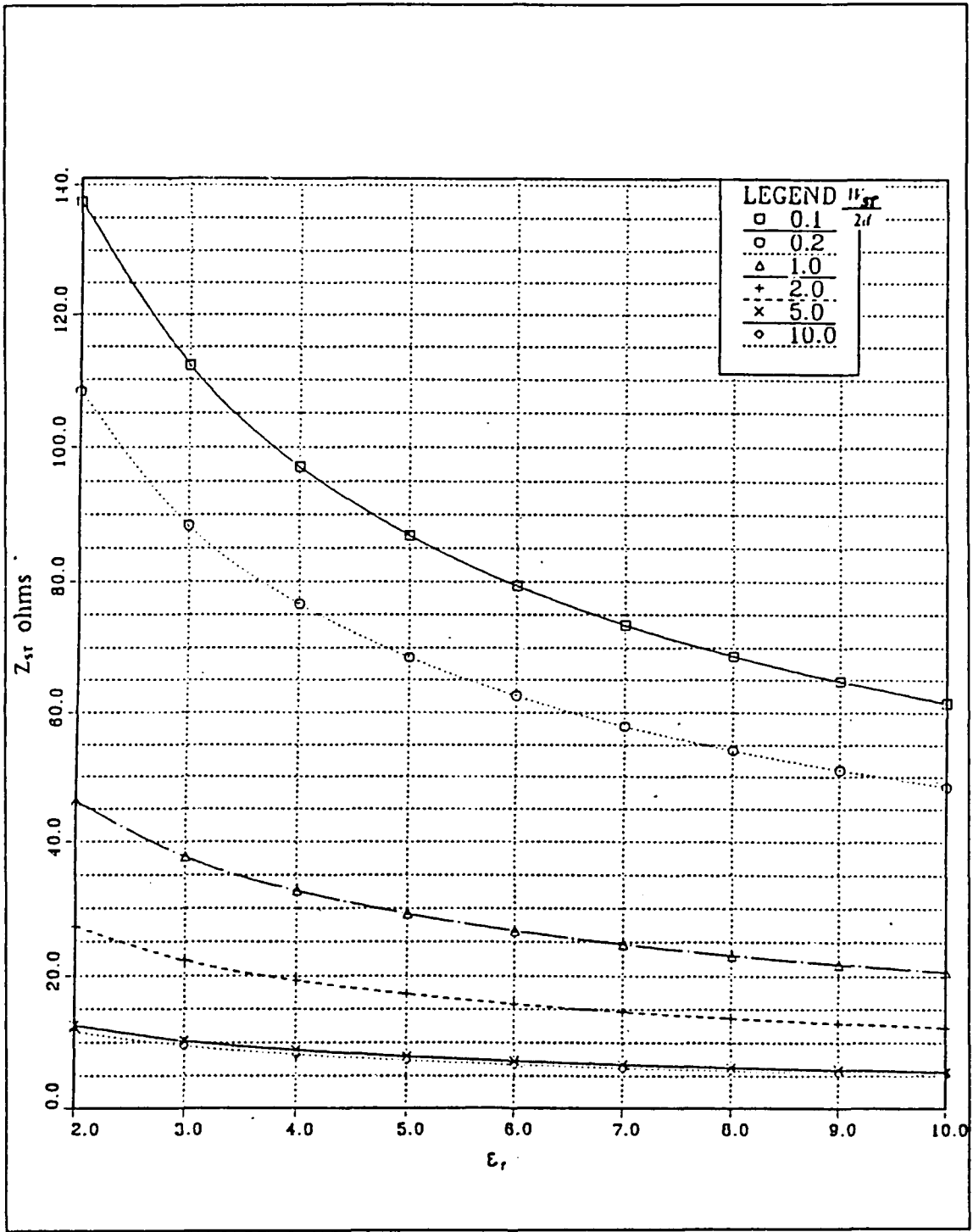


Figure 4. Stripline characteristic impedance versus ϵ_r .

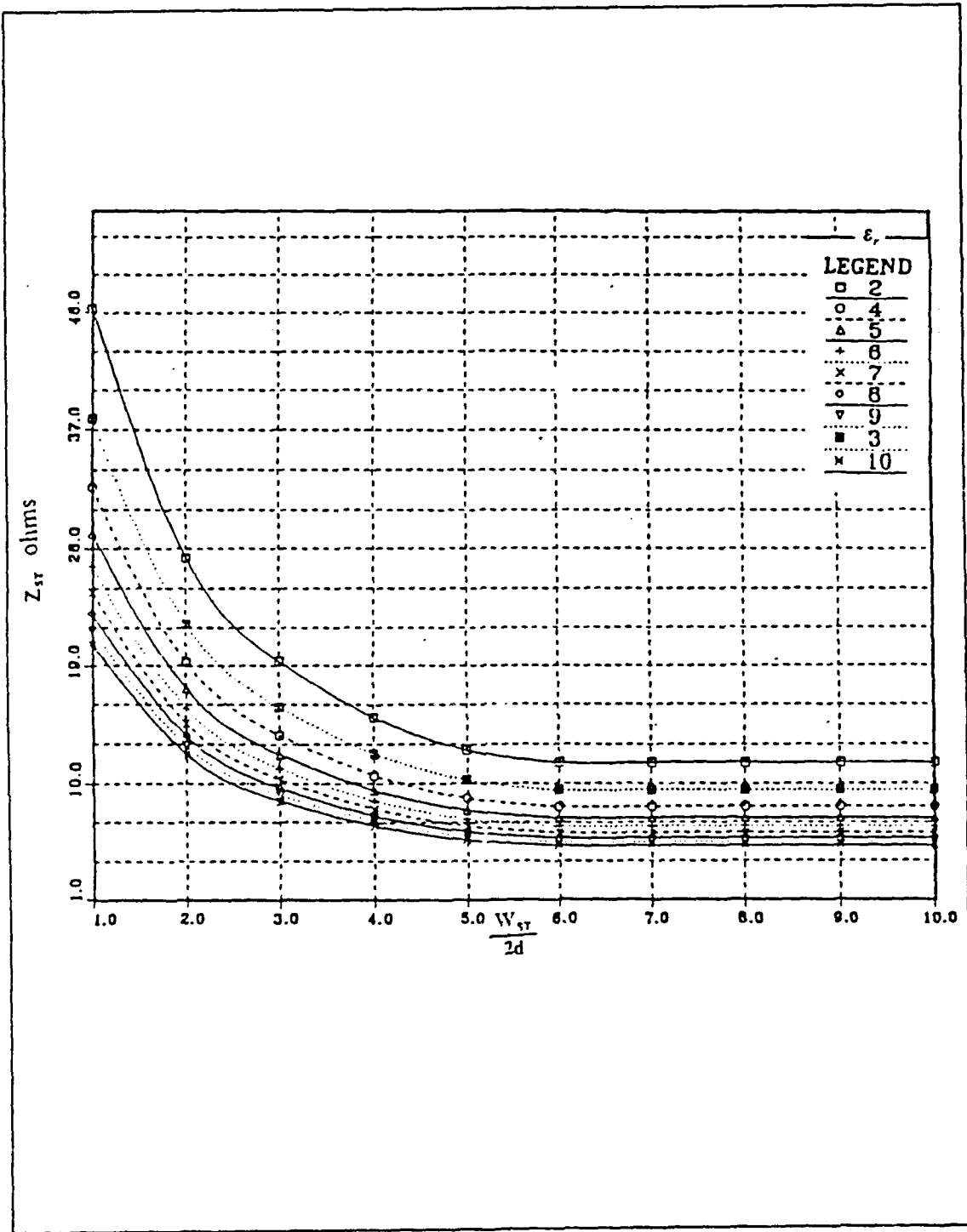


Figure 5. Stripline characteristic impedance versus $W_{ST}/2d$, for $1.0 \leq W_{ST}/2d \leq 10.0$

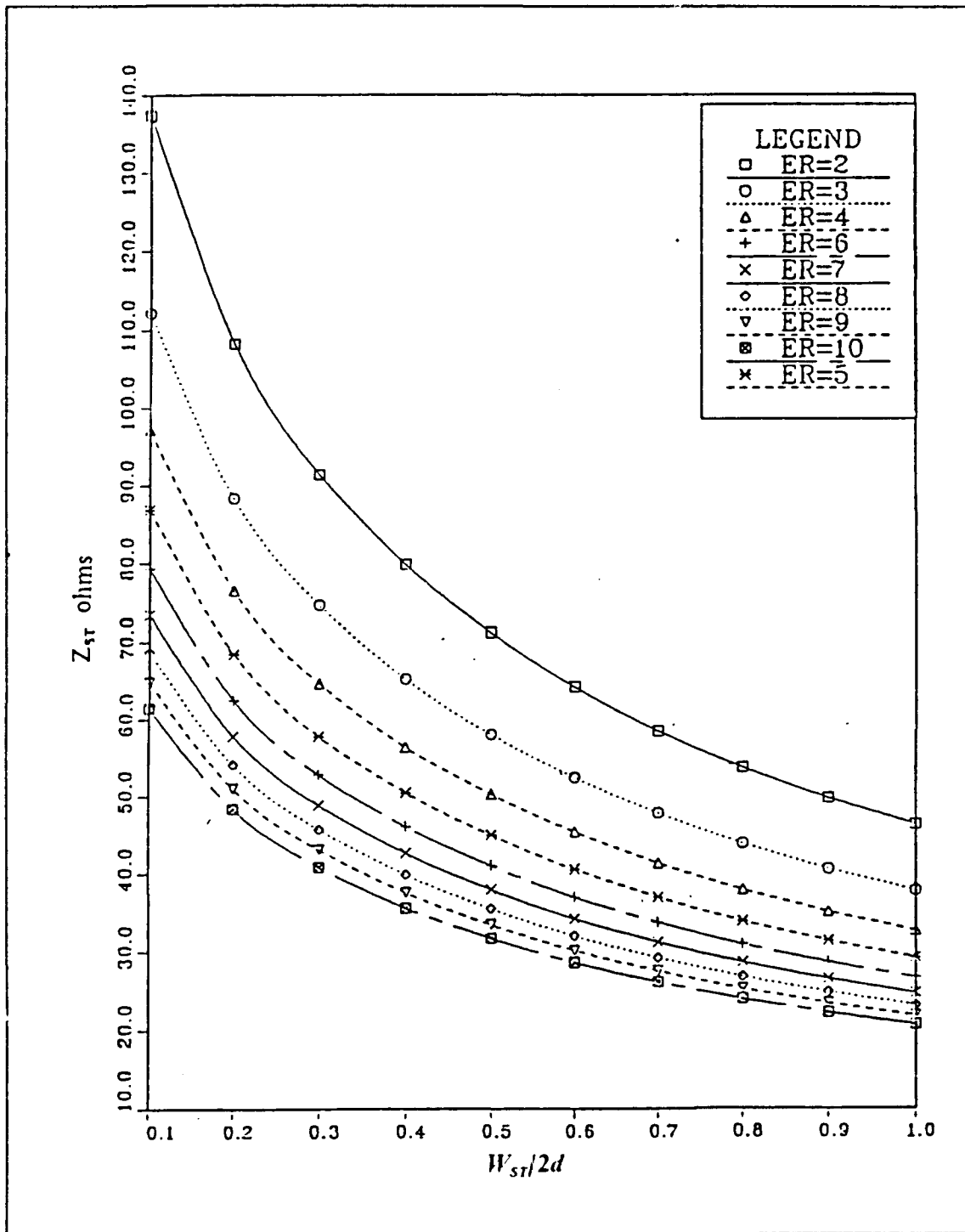


Figure 6. Stripline characteristic impedance versus $W_{ST}/2d$, for $0.1 \leq W_{ST}/2d \leq 1.0$

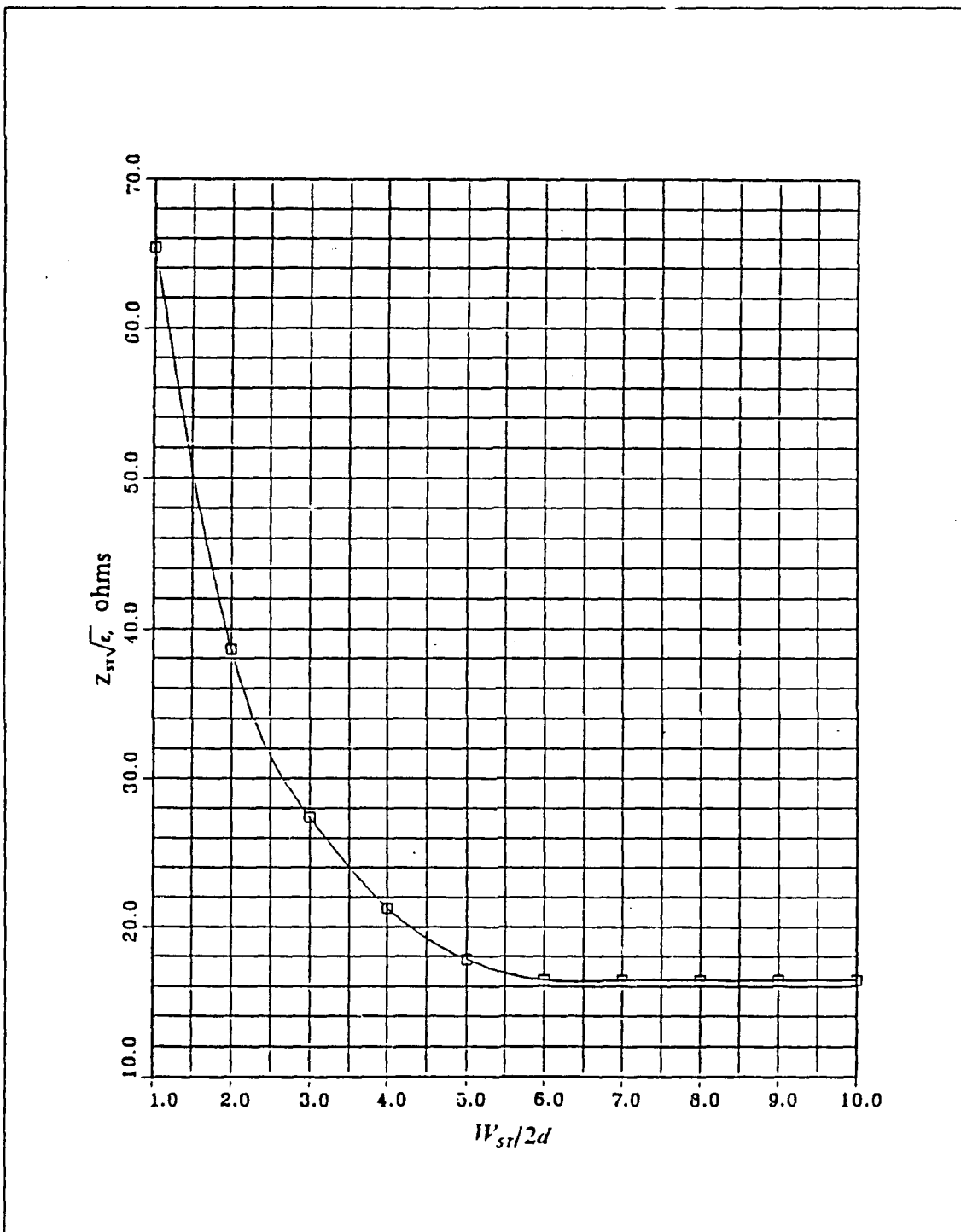


Figure 7. Plot of $Z_{ST}\sqrt{\epsilon_r}$ versus $W_{ST}/2d$

B. BILATERAL SLOT LINE CHARACTERISTIC IMPEDANCE

The geometry of a Bilateral Slot Line (BSL) is shown in Fig. 8A. Since BSL is a symmetric structure, it can support two modes, an even mode and an odd mode. The electric and the magnetic fields in a BSL are shown in Fig. 3B. The electric fields in the upper slot and lower slot have equal magnitude but opposite sign in the case of the odd mode; while in the case of the even mode, the slot electric field is exactly the same in both slots. A perfect magnetic conductor can be placed in the plane of symmetry for the even mode. Considering the above fact, the author of [Refs. 4, 15] simplified the BSL structure to one which consists of a single-side slot of width w backed by a magnetic conductor.

We will reproduce here for the sake of clarity from [Ref. 4] the steps involved in the determination of the bilateral slotline characteristics. For the sake of analytical simplicity, coordinate transformations as shown in Fig. 9 are introduced.

The coordinates (u,v) are related to (x,z) coordinates via:

$$\begin{bmatrix} \vec{u} \\ \vec{v} \end{bmatrix} = \begin{bmatrix} -\cos \theta & \sin \theta \\ \sin \theta & \cos \theta \end{bmatrix} \begin{bmatrix} \vec{x} \\ \vec{z} \end{bmatrix} \quad (11)$$

The inverse relation is

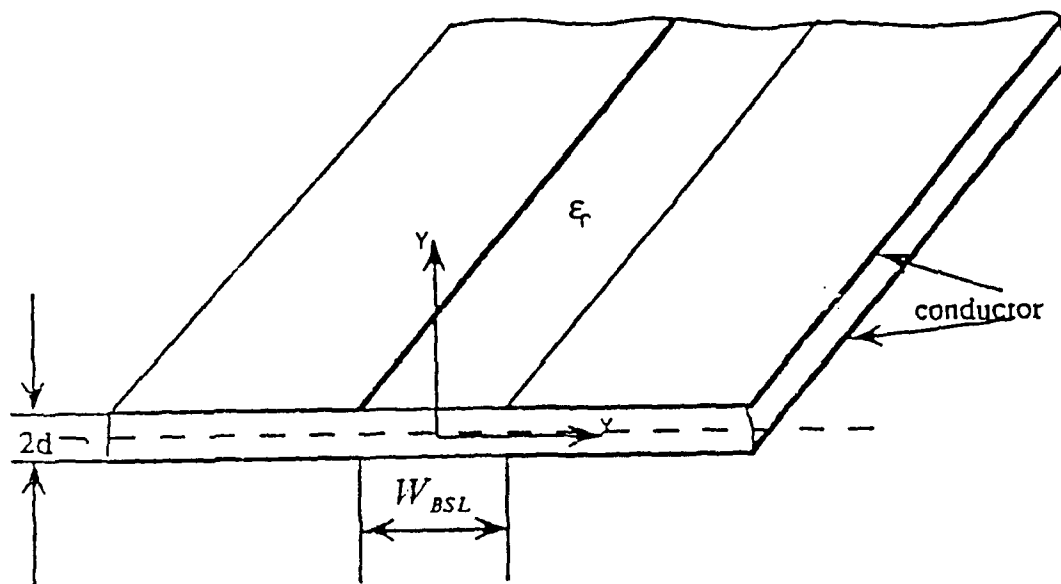
$$\begin{bmatrix} \vec{x} \\ \vec{z} \end{bmatrix} = \begin{bmatrix} -\cos \theta & \sin \theta \\ \sin \theta & \cos \theta \end{bmatrix} \begin{bmatrix} \vec{u} \\ \vec{v} \end{bmatrix} \quad (12)$$

In the above equations, $\cos \theta = \frac{\alpha}{\sqrt{\alpha^2 + \beta^2}}$ and $\sin \theta = \frac{\beta}{\sqrt{\alpha^2 + \beta^2}}$. An $e^{j(\omega t - \beta z)}$ time and z dependence is assumed of all field quantities, where β is the unknown propagation constant and ω is the radian frequency. The fields are transformed into the Fourier transform domain as

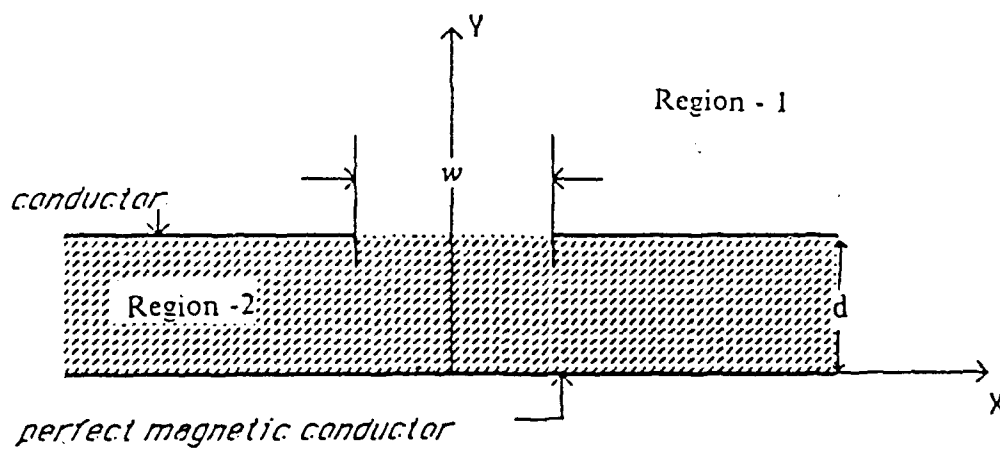
$$\begin{aligned} E_{yi} &= \frac{1}{2\pi} \int_{-\infty}^{\infty} \tilde{E}_{yi} e^{-j\alpha x} d\alpha \\ H_{yi} &= \frac{1}{2\pi} \int_{-\infty}^{\infty} \tilde{H}_{yi} e^{-j\alpha x} d\alpha \end{aligned} \quad (13)$$

where a tilde (-) above a quantity denotes its Fourier transform and α is the transform variable.

The y component of the electric field in region i is [Ref. 15]



(A) Geometry configuration of BSL. From [Ref. 4: p. 12]



(B) Simplified BSL. After [Ref. 15]

Figure 8. Configuration of BSL and simplified BSL

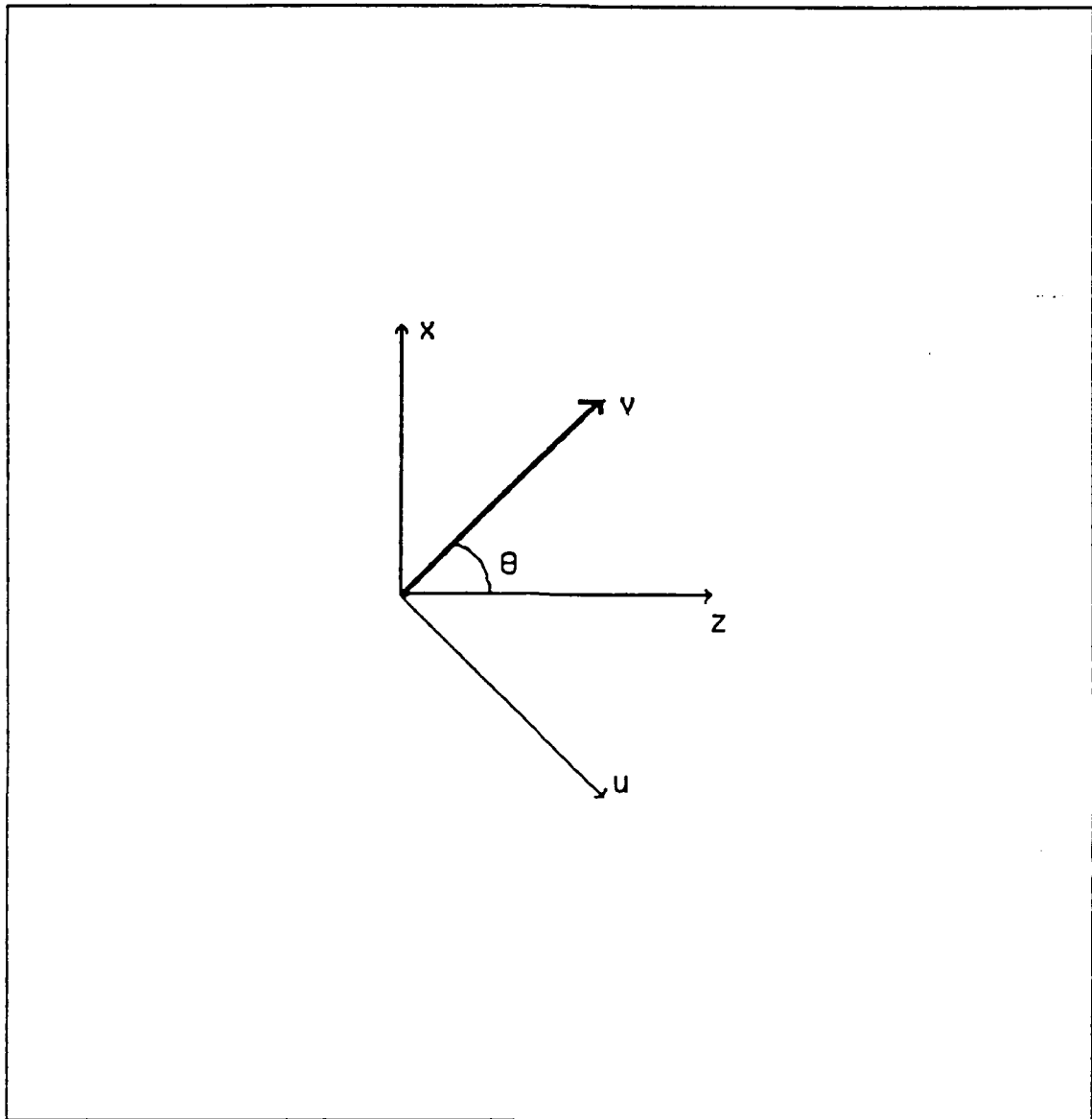


Figure 9. Coordinate transformation

$$E_{yi} = \frac{1}{j\omega\epsilon_i} \left(\frac{\partial^2}{\partial y^2} + k_i^2 \right) \Psi_i^e$$

$$\tilde{E}_{yi} = \frac{1}{j\omega\epsilon_o\epsilon_{ri}} \left(\frac{\partial^2}{\partial y^2} + k_i^2 \right) \tilde{\Psi}_i^e = \frac{1}{j\omega\epsilon_o\epsilon_{ri}} (\gamma_i^2 + k_i^2) \tilde{\Psi}_i^e. \quad (14)$$

Using the fact that $\gamma_i^2 = \alpha^2 + \beta^2 - k_i^2$, the last equation becomes

$$\tilde{E}_{yi} = \frac{\alpha^2 + \beta^2}{j\omega\epsilon_0\epsilon_{ri}} \tilde{\Psi}_i^e = \frac{\alpha^2 + \beta^2}{\hat{y}} \tilde{\Psi}_i^e \quad (15)$$

where $\hat{y} = j\omega\epsilon_0\epsilon_{ri}$.

The subscript $i = 1, 2$ designates region 1 (air) or 2 (dielectric substrate). In the above equations, γ_i is the propagation constant in the y-direction and k_i is the wavenumber in the region i . The scalar potentials $\tilde{\Psi}_i^e$ and $\tilde{\Psi}_i^h$ for the TM_y and TE_y fields respectively are given in terms of the fields as

$$\begin{aligned} \tilde{\Psi}_i^e &= \frac{j\omega\epsilon_0\epsilon_{ri}}{\alpha^2 + \beta^2} \tilde{E}_{yi} \\ \tilde{\Psi}_i^h &= \frac{j\omega\mu_0}{\alpha^2 + \beta^2} \tilde{H}_{yi} \end{aligned} \quad (16)$$

The superscript "e" designates the electric part of transverse magnetic field, and "h" designates the magnetic part of transverse electric field. Also ϵ_0 and μ_0 are the permittivity and permeability of vacuum.

The general expressions for the fields of a TM_y mode in region i (see Fig. 8B) are [Ref. 15]

$$\begin{aligned} E_{xi} &= \frac{1}{j\omega\epsilon_0\epsilon_{ri}} \frac{\partial^2}{\partial x \partial y} \Psi_i^e \\ \tilde{E}_{xi} &= \frac{1}{j\omega\epsilon_0\epsilon_{ri}} (-j\alpha) \frac{\partial}{\partial y} \tilde{\Psi}_i^e \\ &= \frac{-j\alpha}{\alpha^2 + \beta^2} \frac{\partial}{\partial y} \tilde{E}_{yi} \\ \tilde{E}_{zi} &= \frac{-j\beta}{\alpha^2 + \beta^2} \frac{\partial}{\partial y} \tilde{E}_{yi} \end{aligned} \quad (17)$$

$$\begin{aligned} \tilde{H}_{xi} &= j\beta \frac{j\omega\epsilon_0\epsilon_{ri}}{\alpha^2 + \beta^2} \tilde{E}_{yi} \\ \tilde{H}_{zi} &= -j\alpha \frac{j\omega\epsilon_0\epsilon_{ri}}{\alpha^2 + \beta^2} \tilde{E}_{yi} \end{aligned} \quad (18)$$

The total vector magnetic field is given by

$$\begin{aligned}\tilde{H}_i &= \frac{j(\omega\epsilon_0\epsilon_{ri})}{\sqrt{\alpha^2 + \beta^2}} \left[\frac{\beta}{\sqrt{\alpha^2 + \beta^2}} \hat{x} - \frac{\alpha}{\sqrt{\alpha^2 + \beta^2}} \hat{z} \right] \tilde{E}_{yi} \\ &= -j \frac{j\omega\epsilon_0\epsilon_{ri}}{\sqrt{\alpha^2 + \beta^2}} \hat{u} \tilde{E}_{yi}\end{aligned}\quad (19)$$

Using equations (17) the fields \tilde{E}_{xi} , \tilde{E}_{zi} for the TM_y mode can be combined as

$$\begin{aligned}\tilde{E}_{xi} \hat{x} + \tilde{E}_{zi} \hat{z} &= \frac{-j}{\sqrt{\alpha^2 + \beta^2}} \left[\frac{\alpha}{\sqrt{\alpha^2 + \beta^2}} \hat{x} + \frac{\beta}{\sqrt{\alpha^2 + \beta^2}} \hat{z} \right] \frac{\partial}{\partial y} \tilde{E}_{yi} \\ &= \frac{-j}{\sqrt{\alpha^2 + \beta^2}} (\hat{x} \sin \theta + \hat{z} \cos \theta) \frac{\partial}{\partial y} \tilde{E}_{yi}\end{aligned}\quad (20)$$

The total transformed electric field \tilde{E}_i in the region i is then

$$\tilde{E}_i = - \frac{j}{\sqrt{\alpha^2 + \beta^2}} \frac{\partial}{\partial y} \tilde{E}_{yi}\quad (21)$$

Thus, for the TM_y mode, only \tilde{E}_{yi} , \tilde{E}_{vi} , and \tilde{H}_{vi} exist.

Similar expressions could be obtained for the TE_y mode as

$$\tilde{E}_i = +j \frac{j\omega\mu_0\mu_{ri}\hat{u}}{\sqrt{\alpha^2 + \beta^2}} \tilde{H}_{yi}\quad (22)$$

$$\tilde{H}_i = - \frac{j}{\sqrt{\alpha^2 + \beta^2}} \frac{\partial}{\partial y} \tilde{H}_{yi}\quad (23)$$

For the TE_y mode, only \tilde{H}_{yi} , \tilde{E}_{vi} , and \tilde{H}_{vi} exist.

The transformed fields and the propagation constant along y-axis in each region of the bilateral slot line are given by [Ref. 15]

Region - 1, (air)

$$\gamma_1^2 = \alpha^2 + \beta^2 - k_o^2 = \gamma_o^2\quad (24)$$

where γ_1 is the y-directed propagation constant in the region 1 and $k_o = \omega\sqrt{\epsilon_o\mu_o}$ is the free space wavenumber.

For the case of TM_y , we have

$$\tilde{E}_{y1} = A_1(\alpha)e^{-\gamma_0(y-d)} \quad (25)$$

Using the above equation in equation (21) and (2), we have

$$\tilde{E}_{v1} = \frac{j\gamma_0}{\sqrt{\alpha^2 + \beta^2}} A_1(\alpha)e^{-\gamma_0(y-d)} \quad (26)$$

$$\tilde{H}_{u1} = \frac{\omega\epsilon_0}{\sqrt{\alpha^2 + \beta^2}} A_1(\alpha)e^{-\gamma_0(y-d)} \quad (27)$$

and for the TE_y mode,

$$\tilde{H}_{y1} = B_1(\alpha)e^{-\gamma_0(y-d)} \quad (28)$$

$$\tilde{H}_{v1} = \frac{+j\gamma_0}{\sqrt{\alpha^2 + \beta^2}} B_1(\alpha)e^{-\gamma_0(y-d)} \quad (29)$$

Region-2

$$\gamma_2 = \sqrt{\alpha^2 + \beta^2 - \epsilon_r k_0^2} \quad (30)$$

For the TM_y mode, we have

$$\begin{aligned} \tilde{E}_{y2} &= A_2 \sinh \gamma_2 y \\ \tilde{E}_{v2} &= -\frac{j\gamma_2 A_2}{(\alpha^2 + \beta^2)^{1/2}} \cosh \gamma_2 y \\ \tilde{H}_{u2} &= \frac{\omega\epsilon_0\epsilon_r}{(\alpha^2 + \beta^2)^{1/2}} A_2 \sinh \gamma_2 y \end{aligned} \quad (31)$$

where A_2 is an unknown coefficient and γ_2 is the propagation constant in the region 2.

Imposing the continuity of the tangential electric field at $y=d$, we have

$$A_1 = -\frac{\gamma_2}{\gamma_0} A_2 \cosh \gamma_2 d. \quad (32)$$

The transformed electric surface current \tilde{J} , residing on the interface $y=d$ as a function of transformed magnetic field is

$$\tilde{J}_v = \tilde{H}_{u1} - \tilde{H}_{u2} \quad (33)$$

Combining equation (27), equation (30) and equation (32), we have

$$\begin{aligned} \tilde{J}_v &= -j\omega\epsilon_o \left(\frac{1}{\gamma_o} + \frac{\epsilon_r \tanh \gamma_2 d}{\gamma_2} \right) \tilde{E}_v \\ &= G_{22} \tilde{E}_v. \end{aligned} \quad (34)$$

From the last equation we extract the Green's function G_{22} as [Ref. 4: p. 4]

$$G_{22} = -j\omega\epsilon_o \left(\frac{1}{\gamma_o} + \frac{\epsilon_r \tanh \gamma_2 d}{\gamma_2} \right). \quad (35)$$

One can note that if we use the transform domain, the resulting Green's function has a relatively simple form, and it is easy to handle numerically.

For the TE_y , we have

$$\begin{aligned} \tilde{H}_{y2} &= B_2 \cosh \gamma_2 y \\ \tilde{H}_{v2} &= -\frac{j\gamma_2 B_2}{(\alpha^2 + \beta^2)^{1/2}} \sinh \gamma_2 y \\ \tilde{E}_{u2} &= \frac{-\omega\mu_o}{(\alpha^2 + \beta^2)^{1/2}} B_2 \cosh \gamma_2 y \end{aligned} \quad (36)$$

where B_2 is unknown coefficient.

Imposing the continuity of the magnetic field \tilde{H} , on the interface $y=d$, we obtain

$$B_1 = B_2 \cosh \gamma_2 d. \quad (37)$$

The transformed surface current \tilde{J}_u in the u direction, in terms of \tilde{H}_{v2} and \tilde{H}_{v1} , is

$$\tilde{J}_u = \tilde{H}_{v2} - \tilde{H}_{v1} \quad \text{at } y = d. \quad (38)$$

Combining equation (23) and (35) we have

$$\tilde{J}_u = \frac{j}{\omega\mu_o} (\gamma_o + \gamma_2 \tanh \gamma_2 d) \tilde{E}_u = G_{11} \tilde{E}_u \quad (39)$$

where the Green's function G_{11} is

$$G_{11} = \frac{j}{\omega\mu_0} (\gamma_0 + \gamma_2 \tanh \gamma_2 d). \quad (40)$$

Once again we end up with a simple formula for the Green's function in the transformed domain.

Using the standard spectral domain approach, the slot electric field E_x, E_z are related to the electric surface currents J_x, J_z as follows [Ref. 4: p. 4]. In the u, v coordinates the relation between surface currents and the tangential fields is

$$\begin{aligned} \tilde{J}_v &= G_{22} \tilde{E}_v \\ \tilde{J}_u &= G_{11} \tilde{E}_u \end{aligned} \quad (41)$$

Using the transformation between the u-v and the x-z coordinates, we obtain

$$\begin{bmatrix} \tilde{J}_x \\ \tilde{J}_z \end{bmatrix} = \frac{1}{(\alpha^2 + \beta^2)} \begin{bmatrix} \beta^2 G_{11} + \alpha^2 G_{22} & \alpha\beta(G_{22} - G_{11}) \\ \alpha\beta(G_{22} - G_{11}) & \alpha^2 G_{11} + \beta^2 G_{22} \end{bmatrix} \begin{bmatrix} \tilde{E}_x \\ \tilde{E}_y \end{bmatrix} \quad (42)$$

Rewriting the various Green's function as

$$\begin{aligned} G_{xx} &= \frac{(\alpha^2 G_{22} + \beta^2 G_{11})}{(\alpha^2 + \beta^2)} \\ G_{zz} &= \frac{(\alpha^2 G_{11} + \beta^2 G_{22})}{(\alpha^2 + \beta^2)} \\ G_{xz} = \tilde{G}_{zx} &= \alpha\beta \frac{(G_{22} - G_{11})}{(\alpha^2 + \beta^2)}, \end{aligned} \quad (43)$$

we express equation 42 in a matrix form as

$$\begin{pmatrix} G_{xx} & G_{xz} \\ G_{zx} & G_{zz} \end{pmatrix} \begin{pmatrix} \tilde{E}_x(\alpha) \\ \tilde{E}_z(\alpha) \end{pmatrix} = \begin{pmatrix} \tilde{J}_x(\alpha) \\ \tilde{J}_z(\alpha) \end{pmatrix} \quad (44)$$

Equation 44 is solved by the method of moments. The tangential electric fields are expanded in sets of basis functions of the form

$$\tilde{E}_x(x) \approx \sum_{n=1}^N a_n f_n(x), \quad \tilde{E}_z(x) \approx \sum_{m=1}^M b_m g_m(x) \quad (45)$$

The Fourier transform of the slot electric field is

$$\tilde{E}_x(\alpha) = \sum_{n=1}^N a_n \tilde{f}_n(\alpha), \quad \tilde{E}_z(\alpha) = \sum_{n=1}^M b_n \tilde{g}_n(\alpha) \quad (46)$$

where a_n , and b_n are unknown coefficients.

The basis functions chosen here are [Refs. 4: p. 4, 16]

$$f_n(x) = \frac{2}{\pi w} \frac{T_{2(n-1)}\left(\frac{2x}{w}\right)}{\sqrt{1 - (2x/w)^2}} \quad |x| \leq \frac{w}{2}$$

$$= 0 \quad |x| > \frac{w}{2} \quad (47)$$

$$g_m(x) = \frac{2}{\pi w} \sqrt{1 - \left(\frac{2x}{w}\right)^2} U_{2m-1}\left(\frac{2x}{w}\right) \quad |x| \leq \frac{w}{2}$$

$$= 0 \quad |x| > \frac{w}{2} \quad (48)$$

where the $T_n(x)$, $U_n(x)$ are the Tchebycheff polynomials of order n of first and second kind respectively.

The Fourier transform of $f(x)$ is found using the tables in [Ref. 17: p. 836] as

$$\tilde{f}_n(\alpha) = (-1)^{n-1} J_{2(n-1)}(\alpha) \quad (49)$$

In the same way the $\tilde{g}_n(\alpha)$ is found to be [Ref. 17: p. 836]

$$\tilde{g}_m(\alpha) = j (-1)^{m-1} 2m \frac{J_{2m}\left(\frac{\alpha w}{2}\right)}{\left(\frac{\alpha w}{2}\right)}, \quad (50)$$

where $J_n(x)$ is the Bessel function of order n and argument x .

Substitution of equation (45) and equation (46) into equation (44) yields

$$G_{xx} \tilde{E}_x + G_{xz} \tilde{E}_z = \sum_1^N A_n \tilde{f}_n(\alpha) G_{xx} + \sum_1^M B_n \tilde{g}_n(\alpha) G_{xz} = \tilde{J}_x(\alpha) \quad (51)$$

$$G_{zx} \tilde{E}_x + G_{zz} \tilde{E}_z = \sum_1^N A_n \tilde{f}_n(\alpha) G_{zx} + \sum_1^M B_n \tilde{g}_n(\alpha) G_{zz} = \tilde{J}_z(\alpha) \quad (52)$$

Multiplying equation (51) by $\tilde{f}_m(\alpha)$, $m=1,2,\dots,N$ and equation (52) by $\tilde{g}_n(\alpha)$, $n=1,2,\dots,M$ and then integrating the resulting equations, after some rearrangement, we have the following two equations:

$$\sum_{n=1}^N A_n \int_{-\infty}^{\infty} \tilde{f}_n(\alpha) \tilde{f}_m(\alpha) G_{xx} d\alpha + \sum_1^M B_n \int_{-\infty}^{\infty} \tilde{g}_n(\alpha) \tilde{f}_m(\alpha) G_{xz} d\alpha = \int_{-\infty}^{\infty} \tilde{f}_m(\alpha) \tilde{J}_x(\alpha) d\alpha \quad (53)$$

$$\sum_{n=1}^N A_n \int_{-\infty}^{\infty} \tilde{f}_n(\alpha) \tilde{g}_m(\alpha) G_{xz} d\alpha + \sum_1^M B_n \int_{-\infty}^{\infty} \tilde{g}_n(\alpha) \tilde{g}_m(\alpha) G_{zz} d\alpha = \int_{-\infty}^{\infty} \tilde{g}_m(\alpha) \tilde{J}_z d\alpha. \quad (54)$$

The right side of equation (53) is equal to $\frac{1}{2\pi} \int_{-\infty}^{\infty} f_m(x) J_x(x) dx$. This is equal to zero because $f_m(x)$ and $J_x(x)$ occur in disjoint domains. Similarly the right-hand side of equation (54) is zero. Hence we obtain [Ref. 15],

$$\sum_{n=1}^N A_n \int_{-\infty}^{\infty} \tilde{f}_n(\alpha) \tilde{f}_m(\alpha) G_{xx} d\alpha + \sum_1^M B_n \int_{-\infty}^{\infty} \tilde{g}_n(\alpha) \tilde{f}_m(\alpha) G_{xz} d\alpha = 0 \quad (55)$$

$$\sum_{n=1}^N A_n \int_{-\infty}^{\infty} \tilde{f}_n(\alpha) \tilde{g}_m(\alpha) G_{xz} d\alpha + \sum_1^M B_n \int_{-\infty}^{\infty} \tilde{g}_n(\alpha) \tilde{g}_m(\alpha) G_{zz} d\alpha = 0. \quad (56)$$

We now let

$$P_{mn} = \int_{-\infty}^{\infty} \tilde{f}_m(\alpha) \tilde{f}_n(\alpha) G_{xx} d\alpha \quad m = 1, 2, \dots, N, \quad n = 1, \dots, N \quad (57)$$

$$\begin{aligned}
Q_{mn} &= \int_{-\infty}^{\infty} \tilde{f}_m(\alpha) \tilde{g}_n(\alpha) G_{xz} d\alpha, \quad m = 1, 2, \dots, N, \quad n = 1, \dots, M \\
&= \int_{-\infty}^{\infty} \tilde{g}_m(\alpha) \tilde{f}_n(\alpha) G_{xz} d\alpha, \quad m = 1, 2, \dots, M, \quad n = 1, 2, \dots, N \\
R_{mn} &= \int_{-\infty}^{\infty} \tilde{g}_m(\alpha) \tilde{g}_n(\alpha) G_{zz} d\alpha, \quad m = 1, 2, \dots, M, \quad n = 1, 2, \dots, M
\end{aligned} \tag{58}$$

The quantities P_{mn} , Q_{mn} , R_{mn} are functions of β , which is still unknown. Equation (55) and (56) can then be rewritten as

$$\begin{aligned}
\sum_{n=1}^N A_n P_{mn} + \sum_{l=1}^M B_l Q_{ml} &= 0 \\
\sum_{n=1}^N A_n Q_{nm} + \sum_{l=1}^M B_l R_{ml} &= 0
\end{aligned} \tag{59}$$

The above equations in matrix form is [Ref. 4: p. 4]

$$\begin{bmatrix} P & Q \\ Q^T & R \end{bmatrix} \begin{bmatrix} A_1 \\ \cdot \\ A_N \\ B_1 \\ \cdot \\ B_M \end{bmatrix} = \vec{0} \tag{60}$$

and the wave number β as a function of a free-space wave number k_0 is the the solution of the determinantal equation

$$\det \begin{bmatrix} P & Q \\ Q^T & R \end{bmatrix} = 0. \tag{61}$$

Formulation for the characteristic impedance.

Reference 4 derived an accurate formula for the characteristic impedance of BSL using the spectral Galerkin's method and the following definition of characteristic impedance

$$Z_{BSL} = \frac{|V_{BSL}|^2}{2P_f} \quad (62)$$

where V_{BSL} is the voltage across the slot and P_f is the real part of the complex power carried by each slot. The factor of 2 in the denominator of the last equation is due to the fact that an equal amount of power exists in the lower slot.

The voltage V_{BSL} in terms of the transverse electric field is given by [Ref. 4: p. 12]

$$V_{BSL} = \int_{-w/2}^{w/2} E_x dx = \tilde{E}_x(\alpha = 0) = \tilde{E}_x(0). \quad (63)$$

The complex power flow in the z direction is given by [Ref. 4: p. 12]:

$$\begin{aligned} P_f &= \int_{x=-\infty}^{\infty} \int_y (\vec{E} \times \vec{H}^*) \cdot \hat{z} dx dy \\ &= \frac{1}{2\pi} \int_y \int_{\alpha=-\infty}^{\infty} (\tilde{E} \times \tilde{H}^*) \cdot \hat{z} d\alpha dy. \end{aligned} \quad (64)$$

Equation 64 can be expressed in the form

$$P_f = \frac{1}{2\pi} \iint_{\alpha, y > 0} (\tilde{E}_x \tilde{H}_y^* - \tilde{E}_y \tilde{H}_x^*) d\alpha dy. \quad (65)$$

Characteristics for dielectric substrates $\epsilon_r = 2.22$ and $\epsilon_r = 6.0$ that we will use in our research are plotted in Fig. 10-13. Figure 10 and Fig. 12 display the characteristic impedance of bilateral slotline for $\epsilon_r = 2.22$ and $\epsilon_r = 6.0$ respectively, while Fig. 11 and Fig. 13 show the respective data for $\epsilon_{eff} = (\frac{\beta}{k_0})^2$. Figures 14 and 15 depict the comparison between the effective dielectric constant and characteristic impedance of a bilateral slotline with that of a single-sided slotline for $\epsilon_r = 2.22$ and $\frac{W}{d} = 0.08$. We should observe that the bilateral slotline is preferred to the single-sided slotline for the following reasons [Ref. 4: pp. 3-24]:

1. bilateral slotline has relatively less dispersion than the single-sided slotline,
2. the characteristic impedance of bilateral slotline is approximately 50% of that of single-sided slotline as it is illustrated in Fig. 15, and

3. the slot width to achieve a certain impedance is larger for bilateral slotline than the single-sided slotline. The last reason partially overcomes the fabrication problem associated with etching narrow slots on low permittivity substrate.

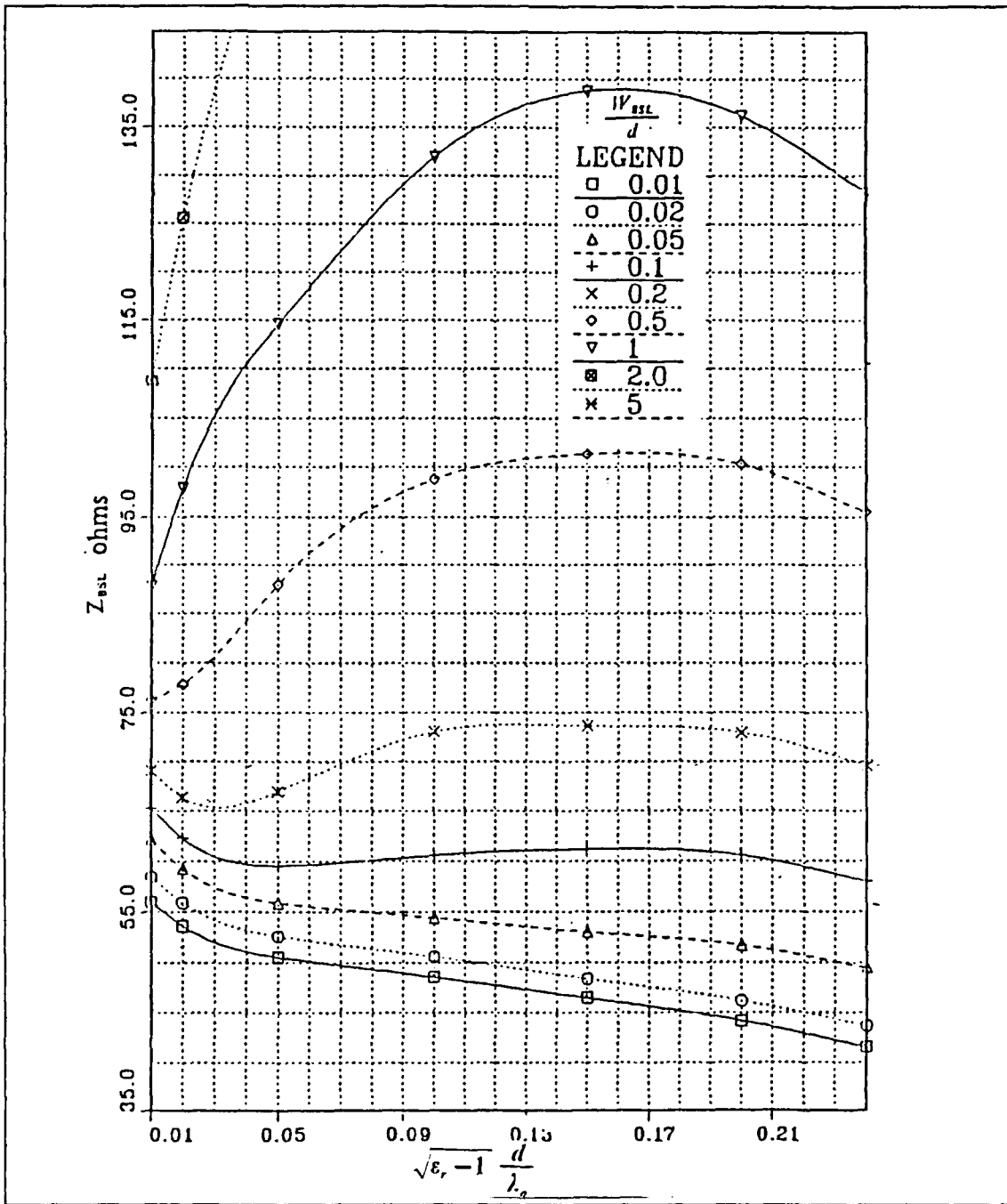


Figure 10. Bilateral slotline characteristic impedance versus $\sqrt{\epsilon_r - 1} \frac{d}{\lambda_0}$: For $\epsilon_r = 2.22$. After [Ref. 4: p. 14]

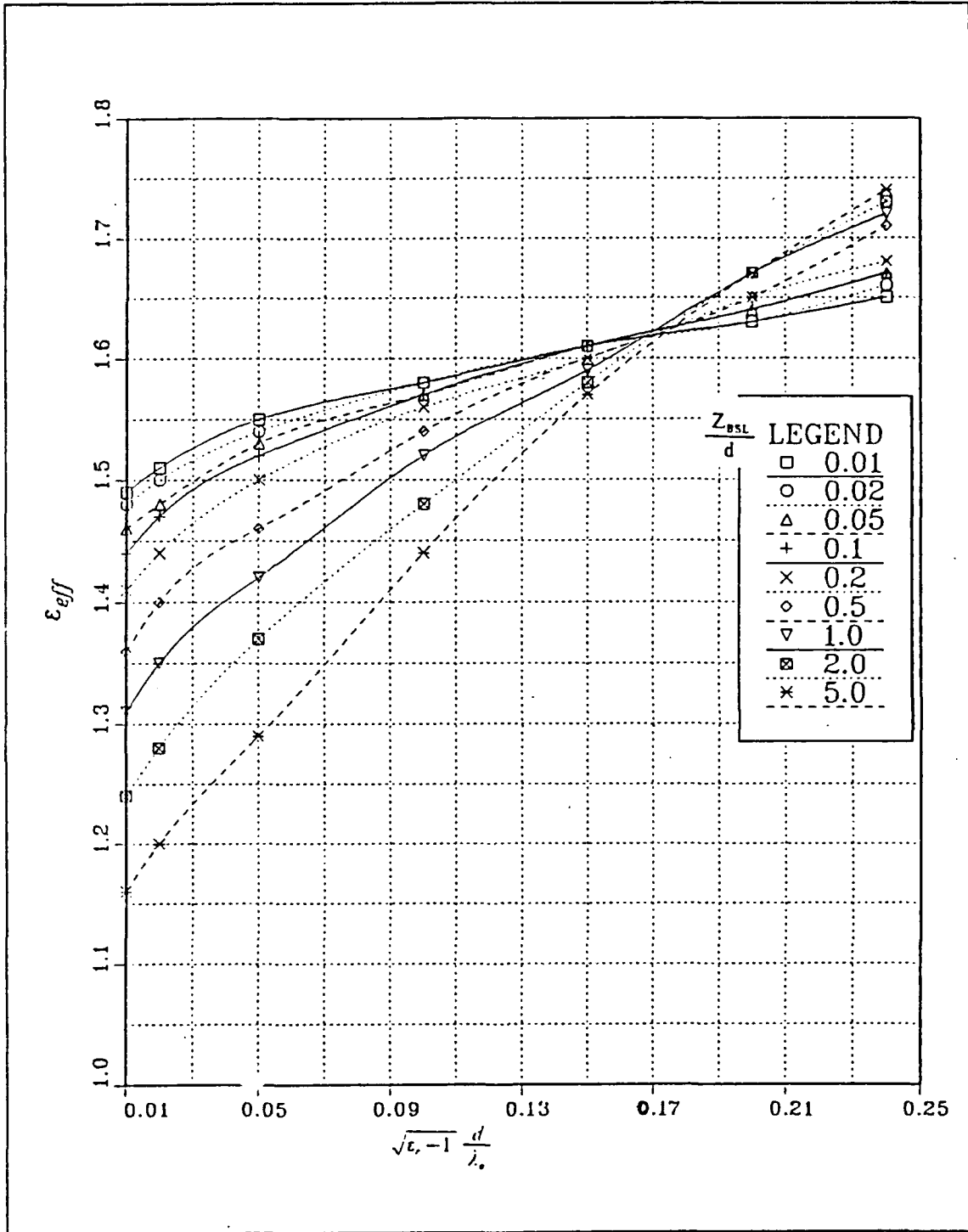


Figure 11. Plot of ϵ_{eff} versus $\sqrt{\epsilon_r} - 1 \frac{d}{\lambda_0}$: For $\epsilon_r = 2.22$. After [Ref. 4: p. 13]

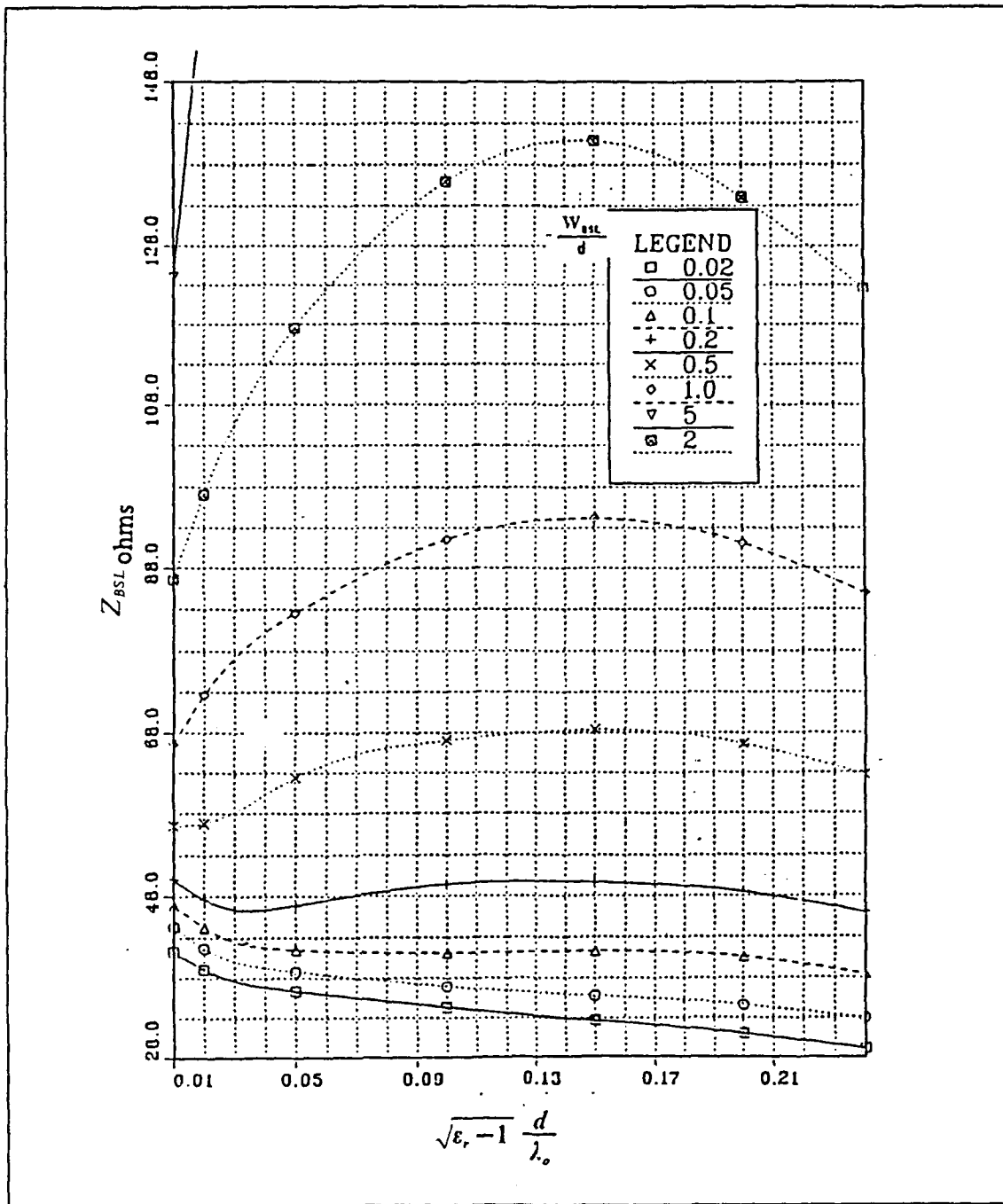


Figure 12. Bilateral slotline characteristic impedance versus $\sqrt{\epsilon_r - 1} \frac{d}{\lambda_0}$: For $\epsilon_r = 6.0$. After [Ref. 4: p. 18]

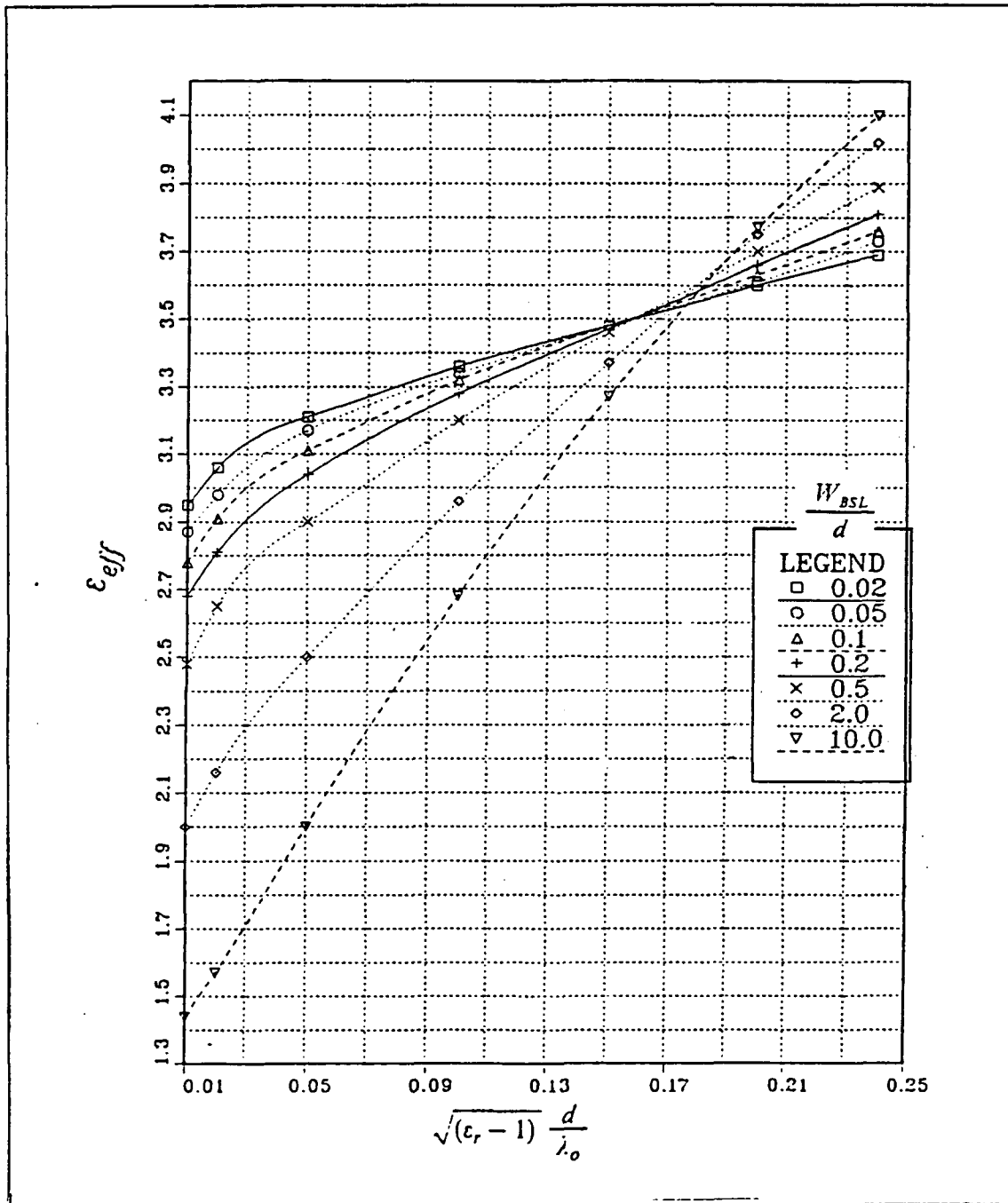


Figure 13. Dispersion characteristic of bilateral slotline for $\epsilon_r = 6.0$: After [Ref. 4: p. 17]

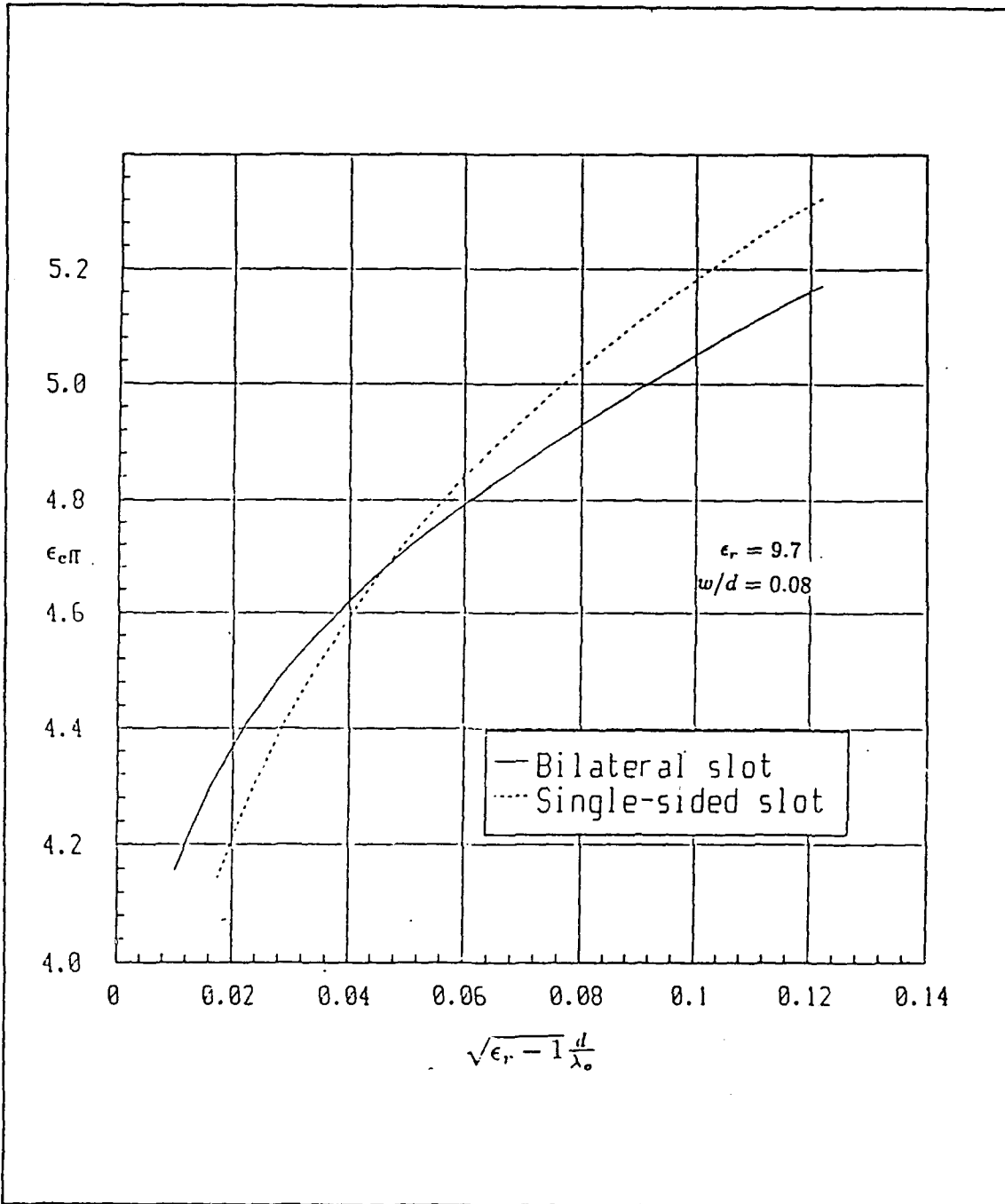


Figure 14. Comparison of ϵ_{eff} between BSL and single-sided slotline: $\epsilon_r = 9.7$ and $w/d = 0.08$. From [Ref. 4: p. 23]

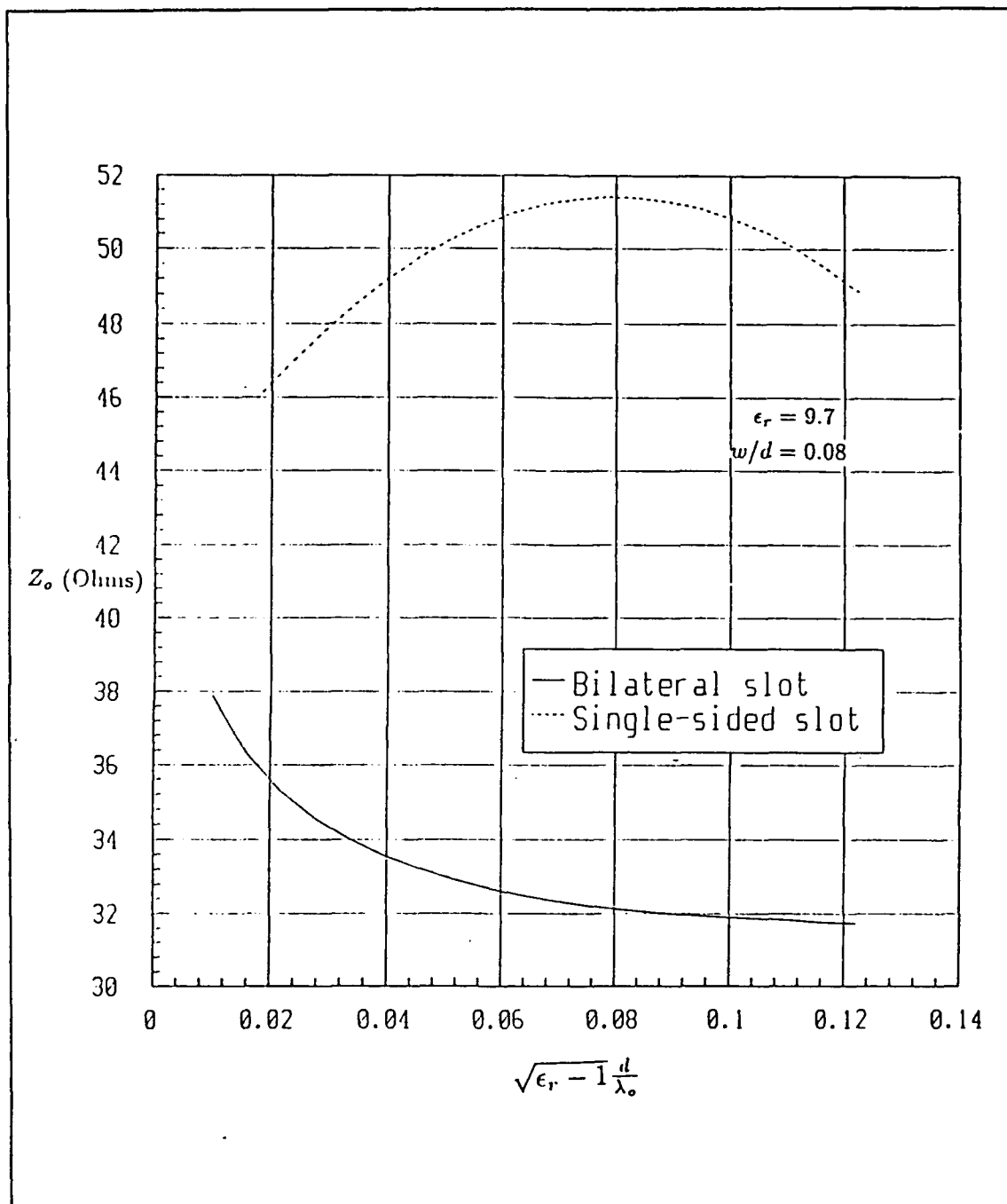


Figure 15. Comparison of Z_0 between BSL and single-sided slotline: $\epsilon_r = 9.7$ and $w/d = 0.08$. From [Ref. 4: p. 24]

IV. DESIGN OF LINEAR TAPERED SLOT ANTENNA AND BILATERAL SLOT LINE ANTENNA

A. BACKGROUND

Early slotline antennas were fed by means of microstrip-to-slotline transitions. The network could have undesirable radiation especially when used in array applications. Also the width of the feed line is extremely narrow leading to fabrication difficulties. The proposed structure, using a bilateral slot line, reduces the feed radiation problem. A stripline is used to energize the antenna (see Fig. 2). The BSL antennas and the LTSA were designed by gradually widening the slotline in a linear tapered shape over a length $2\lambda_o$ from the point $\lambda_{BSL}/8$ away from the junction so that the width of slotline at the front-end is equal one-half of antenna width.

We kept the flare angle 2α constant and equal to 12° which is almost optimum [Ref. 18] and where a symmetric beamwidth usually occurs [Ref. 2]. The operating range of frequency is determined by the ratio of total antenna thickness $2d$ to free-space wavelength, $2d/\lambda_o$. Antenna No.2 was designed using dielectric constant 2.22, but was implemented with dielectric constant 2.33. A copper-deposited 3.15 mm thick RT Duroid 5870 ($\epsilon_r = 2.33$) was used for antenna No.2 and 1.27 mm thick Duroid 6006 ($\epsilon_r = 6.0$) was used for the rest. The antenna patterns were measured in the frequency range 5-9 GHz in steps of 1 GHz.

In all the antennas, we used $\frac{2d}{\lambda_o} = 0.02$ or 0.03 for the lower and the upper limit of operating frequencies respectively. The total antenna length L is given by

$$L = (2\lambda_o + \frac{\lambda_{BSL}}{8} + W_{ST} + \frac{\lambda_{BSL}}{4} + 1.0) \text{ cm.} \quad (66)$$

We have designed three BSL antennas in order to examine the performance of these antennas for different substrates and different slotline-to-stripline matching impedances. In the transition we used, the bilateral slot line etched on both sides of the antenna crosses the stripline conductor perpendicularly as seen in Fig. 2.

B. ANTENNAS ON $\epsilon_r = 6.0$ SUBSTRATE

In order to study the effect of the various antenna structures and the effect of existence or not of extra substrate at the back-end and front-end of the antenna, four types of antennas were fabricated. The first was a single-sided Linear Tapered Slot Antenna LTSA, labelled No.1A. The second labelled No.1B is a Bilateral Slot Line (BSL) antenna with extra dielectric substrate at the back-end and the front-end, as shown in Fig. 16A. The BSL antenna was fabricated by arranging two identical antennas of type No.1A, one on top of the other without any lateral displacement. Antenna No.1CO, shown in Fig. 16B, was fabricated by cutting only the front-end extra substrate and leaving the back-end substrate of antenna No.1B. The last type, No.1C, was a BSL antenna (Fig. 16c) and was fabricated by removing the extra substrate of the antenna No.1CO.

The extra substrate at the front-end was 6.5 mm long and was 3.0 mm at the back-end. All antennas had a width of 36.57 mm and a thickness of approximately 1.273 mm.

A stripline with characteristic impedance 50 ohms ($Z_{ST} = 50$ ohms) was used in order to match a bilateral slotline having characteristic impedance 70 ohm, ($Z_{BSL} = 70$ ohm). The main unknown parameters are the width W_{BSL} of the BSL and W_{ST} , the width of stripline.

The chosen dielectric substrate of antenna No.1 had a dielectric constant $\epsilon_r = 6.0$ and a substrate thickness $d = 0.635$ mm. This results in a BSL antenna having a thickness of 0.127 cm.

From the empirical relationship between substrate thickness $2d$ and free-space wavelength λ_o , $\frac{2d}{\lambda_o} = 0.03$, the corresponding free-space wavelength λ_o was found as 4.233 cm which corresponds to a frequency 7.087 GHz. For $\lambda_o = 4.233$ cm and permittivity $\epsilon_r = 6.0$, the stripline wavelength λ_{ST} is found, from the equation

$$\lambda_{ST} = \frac{\lambda_o}{\sqrt{\epsilon_r}}, \quad (67)$$

to be $\lambda_{ST} = 1.73$ cm.

Figure 17 shows the characteristic impedance of a stripline for $\epsilon_r = 6.0$ in the range $0.3 \leq \frac{W_{ST}}{2d} \leq 0.4$. For $Z_{ST} = 50$ ohm, the ratio of the stripline width to total thickness is found to be $\frac{W_{ST}}{2d} = 0.338$.

Figure 18 shows the plot between Z_{BSL} and $\frac{W_{BSL}}{d}$ for $\epsilon_r = 6.0$ in the vicinity of 70 ohm. The ratio of BSL width to the substrate width for $Z_{BSL} = 70$ ohm and $\epsilon_r = 6.0$ is found to be $\frac{W_{BSL}}{d} = 0.77$, resulting in $W_{BSL} = 0.049$ cm.

For $\lambda_o = 4.233$ cm and $\epsilon_{eff} = 2.662$, the BSL wavelength λ_{BSL} is found from the following equation

$$\lambda_{BSL} = \frac{\lambda_o}{\sqrt{\epsilon_{eff}}} \quad (68)$$

to be $\lambda_{BSL} = 2.59$ cm.

The stripline crosses the BSL in a perpendicular angle and extends into an open circuit a quarter of the strip wavelength. Also the BSL extends a quarter-slot-wavelength beyond the crossing point and terminates into a short circuit as shown in Fig. 2.

The antennas were developed by increasing the width of BSL gradually to $\frac{\lambda_{BSL}}{8}$ away from the feed end to the front end of the antenna to form an opening angle $2\alpha = 12^\circ$. As the width of the slotline increases, the electromagnetic waves move faster since the effective dielectric constant decreases for increasing slot widths, as shown in Fig. 11 and Fig. 13. The speed of the em wave inside the slotline c_{BSL} is given by

$$c_{BSL} = \frac{c}{\sqrt{\epsilon_{eff}}}, \quad (69)$$

where c is the speed of light in vacuum.

The final design data for antenna No.1 are as follows :

1. $\lambda_o = 4.233$ cm
2. $f_o = 7.087$ GHz
3. $\lambda_{BSL} = 2.59$ cm = $0.6\lambda_o$
4. $\lambda_{ST} = 1.73$ cm = $0.41\lambda_o$
5. $W_{BSL} = 0.049$ cm = $0.0116\lambda_o$
6. $W_{ST} = 0.043$ cm = $0.01\lambda_o$
7. $Z_{BSL} = 70$ ohms
8. $Z_{ST} = 50$ ohms
9. $\epsilon_r = 6.0$
10. Substrate thickness $d = 0.0635$ cm

11. Total antenna length $L = 10.454 \text{ cm} = 2.47\lambda_o$
12. Antenna width $W = 3.657 \text{ cm}$
13. Antenna mouth $\frac{W}{2} = 1.83 \text{ cm} = 0.432\lambda_o$
14. Total substrate thickness $2d = 0.127 \text{ cm}$
15. Length of linearly tapered slot $2\lambda_o = 8.466 \text{ cm}$
16. Flare angle $2\alpha = 12^\circ$

C. ANTENNAS ON $\epsilon_r = 2.22$ SUBSTRATE

To investigate the behavior of antennas on different substrates, three other antennas were built on a lower ϵ_r substrate. The single Linear Tapered Slot antenna was labelled No.2A, the BSL antenna with extra substrate, No.2B, and the last one without extra substrate, No.2C. The extra substrate was 2mm long both at the back-end and the front-end. The antenna had a total width of 38.68 mm and a total substrate thickness approximately 3.15 mm. Antenna No.2 was implemented with $\epsilon_r = 2.33$ while, in its design procedure, an $\epsilon_r = 2.22$ was used.

The design procedure is almost the same as of antenna No.1. The only difference being that $\frac{2d}{\lambda_o} = 0.07$ was used instead of 0.03 for the following reason. With $\frac{2d}{\lambda_o} = 0.03$ the free-space wavelength λ_o is 10.5 cm, and the corresponding antenna length is $L = 2\lambda_o + \frac{\lambda_{BSL}}{8} + W_{ST} + \frac{\lambda_{BSL}}{4} + 1.0 = 25.3 \text{ cm}$. For masking purposes, we enlarged the original model by a ratio 2:1 in order to have a precise design. However, the enlarged model was out of range of the plotter paper in the design work-station. To decrease the structure size, we had to decrease the wavelength as well, thus, resulting in a larger $\frac{2d}{\lambda_o}$. With $\frac{2d}{\lambda_o} = 0.07$, the free-space wavelength λ_o is 4.5 cm, and the actual antenna had a length 11.65 cm, and the enlarged model had a length 19.74 cm which was well within the plotter's paper range.

Using the same design equations as in antenna No.1, we ended up with the following data for antenna No.2 :

1. $\lambda_o = 4.5 \text{ cm}$
2. $f_o = 6.67 \text{ GHz}$
3. $\lambda_{BSL} = 3.71 \text{ cm} = 0.824\lambda_o$
4. $\lambda_{ST} = 3.02 \text{ cm} = 0.67\lambda_o$
5. $W_{BSL} = 0.041 \text{ cm} = 0.0092\lambda_o$
6. $W_{ST} = 0.2598 \text{ cm} = 0.058\lambda_o$
7. $\epsilon_r = 2.33$

8. $Z_{BSL} = 70$ ohms
9. $Z_{ST} = 50$ ohms
10. Substrate thickness $d = 0.1575$ cm
11. Total antenna length $L = 11.65$ cm $= 2.59\lambda_0$
12. Antenna width $W = 3.87$ cm
13. Antenna mouth $\frac{W}{2} = 1.935$ cm $= 0.43\lambda_0$
14. Total substrate thickness $2d = 0.315$ cm
15. Length of linearly tapered slot $2\lambda_0 = 9$ cm
16. Flare angle $2\alpha = 12^\circ$

Once again we used a 50 ohm stripline to 70 ohm bilateral slot line transition scheme at the operation frequency f_0 of 6.67 GHz.

D. ANTENNA NO.3

To study the effect of choosing impedances other than 50 ohm stripline to 70 ohm bilateral slotline in the transition, we designed antenna No.3 having 50 ohms for both the stripline and BSL. Our initial goal was to design and build the antenna using a low dielectric constant ($\epsilon_r = 2.22$) substrate having a thickness $d = 0.1575$ cm. Figure 19 illustrates Z_{BSL} as a function of $\frac{W_{BSL}}{d}$ for $\epsilon_r = 2.22$ for values of Z_{BSL} near 50 ohms. Following the standard design procedure as before, we came up with $W_{ST} = 0.1$ mm and $W_{BSL} = 9.53 \times 10^{-4}$ mm which is practically impossible to build. Data for $\epsilon_r = 6.0$ is shown in Fig. 20. For $\epsilon_r = 6.0$, we have $W_{BSL} = 0.1841$ mm which is practically manageable. For this reason, antenna No.3 was designed for $\epsilon_r = 6.0$.

We used the same characteristic impedance for BSL and stripline. Again using the same design procedure as in the previous two antennas, we obtained the following design data :

1. $\lambda_0 = 4.233$ cm
2. $f_0 = 7.087$ GHz
3. $\lambda_{BSL} = 2.5$ cm $= 0.59\lambda_0$
4. $\lambda_{ST} = 1.73$ cm $= 0.41\lambda_0$
5. $W_{BSL} = 0.0178$ cm $= 0.0042\lambda_0$
6. $W_{ST} = 0.043$ cm $= 0.01\lambda_0$
7. $Z_{BSL} = 50$ ohms
8. $Z_{ST} = 50$ ohms

9. $\epsilon_r = 6.0$
10. Substrate thickness $d = 0.0635$ cm
11. Total antenna length $L = 10.45$ cm $= 2.47\lambda_0$
12. Antenna width $W = 3.59$ cm
13. Antenna mouth $\frac{W}{2} = 1.795$ cm $= 0.43\lambda_0$
14. Total substrate thickness $2d = 0.127$ cm
15. Length of linearly tapered slot $2\lambda_0 = 8.466$ cm
16. Flare angle $2\alpha = 12^\circ$

The artwork for antennas No.1 and No.2 were designed using TOUCHTONE program. First, enlarged versions of the antennas were cut on a special film, called rubylith, and the final negatives with the actual model size were developed by the NPS Photo Lab. Antenna No.3 was fabricated at the Naval Weapons Center, China Lake.

Table 1 summarizes the design data for the three antennas.

Table 1. DESIGN DATA

Design data	ANT. No.1	ANT. No.2	ANT. No.3
Free space wavelength, λ_o	4.233 cm	4.5 cm	4.233 cm
Design frequency	7.089 GHz	6.670 GHz	7.089 GHz
BSL wavelength, λ_{BSL}	2.59 cm = 0.60 λ_o	3.71 cm = 0.824 λ_o	2.50 cm = 0.59 λ_o
Stripline wavelength, λ_{ST}	1.73 cm = 0.41 λ_o	3.02 cm = 0.67 λ_o	1.73 cm = 0.41 λ_o
BSL Width, W_{BSL}	0.043 cm = 0.01 λ_o	0.041 cm = 0.0092 λ_o	0.018 cm = 0.0042 λ_o
Stripline Width, W_{ST}	0.043 cm = 0.01 λ_o	0.259 cm = 0.058 λ_o	0.043 cm = 0.01 λ_o
BSL characteristic impedance, Z_{BSL}	70 ohms	70 ohms	50 ohms
Stripline characteristic impedance, Z_{ST}	50 ohms	50 ohms	50 ohms
Dielectric substrate, ϵ_r	6.0	2.33	6.0
Substrate thickness, d.	0.0635 cm	0.1575 cm	0.0635 cm
Total antenna length, L.	10.45 cm = 2.47 λ_o	11.65 cm = 2.59 λ_o	10.45 cm = 2.47 λ_o
Antenna width, W.	3.657 cm	3.870 cm	3.590 cm
Antenna mouth	1.83 cm = 0.432 λ_o	1.94 cm = 0.430 λ_o	1.79 cm = 0.430 λ_o
Total substrate thickness, antenna thickness, 2d.	0.127 cm	0.315 cm	0.127 cm
Length of linearly tapered slot, $2\lambda_o$	8.466 cm	9.000 cm	8.466 cm
Flare angle.	12 °	12 °	12 °

E. LAUNCHING METHOD

Howe [Ref. 19] describes in detail several methods for launching a wave into a stripline. A stripline is not a usual transmission line medium for use in system interconnection, therefore a problem arises, namely how to transform from a transmission line into stripline configuration. Since most striplines are used in broadband systems or low-power receiving systems, waveguide transition is not a proper way. A possible solution to the problem is given by a coaxial line transducer which consists of a coaxial probe.

As was discussed before, stripline propagates a TEM mode, and the best transition scheme is that which will guarantee lossless transition from the TEM mode of coaxial line to the TEM mode of stripline. The best transition scheme is the coaxial stripline launch configuration, having the same characteristic impedance equal to 50 ohm. In all the antennas, a coaxial stripline launcher was utilized. The size of coaxial probe-launcher was chosen so that the center conductor of coaxial line was compatible direct, without any interface step, to the stripline. This scheme results in a low VSWR and gives usually excellent broadband matching. Figure 21 illustrates a coaxial stripline launcher.

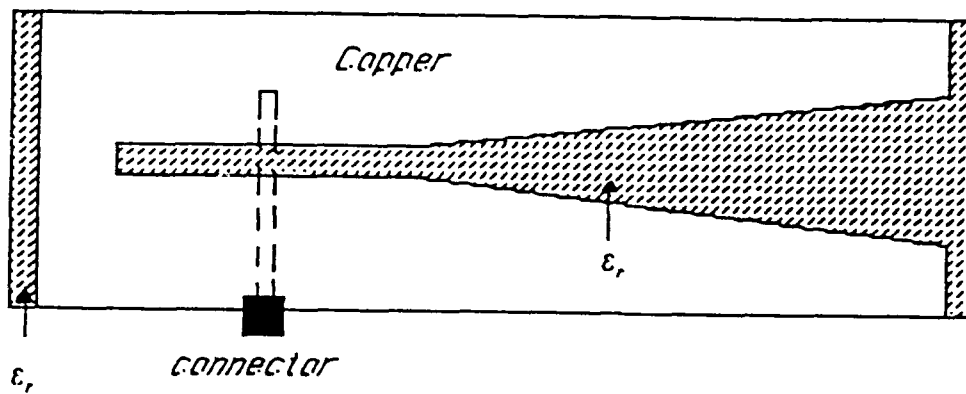
F. ANTENNA CONSTRUCTION

A photolithographical method for fabricating the stripline and bilateral slotline was used. For the construction of stripline and bilateral slot line, it is essential to have high accuracy since a small construction error in the width of strip or slotline can cause a change in characteristic impedance.

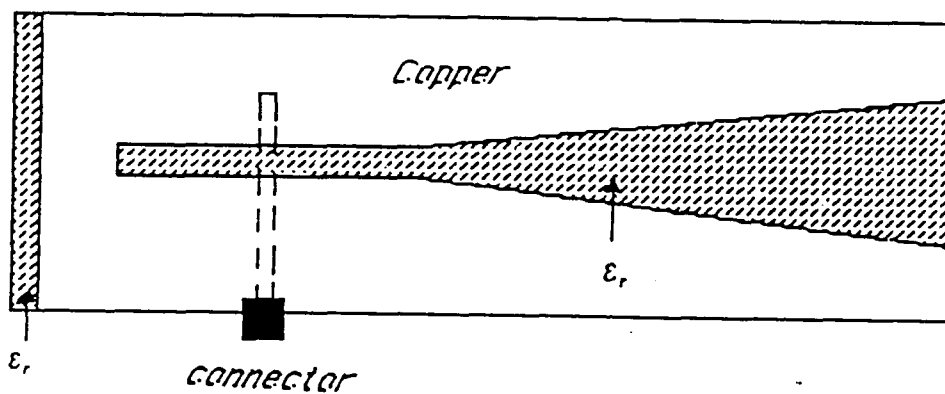
The photolithographical method is economical and provides high accuracy and is commonly used in microwave circuit design. The construction of an antenna consisted of the following phases [Ref. 20: p. 30]

- The desired real size of antenna was plotted by using the available CAD software. The antenna model was cut on a thin film called rbylith. (In this research the actual model was enlarged by the ratio 2:1 in order to avoid inaccuracies during the plotting).
- A real-size negative film was made at the Photo Lab at NPS by reducing the plotting design by ratio 1:2. Figure 22A illustrates the real-size negative of bilateral slotline and Fig. 22B the positive of a stripline for antenna No.3C. Figure 23 depicts the top view and side view of the antenna No.3C.
- Photosensitive emulsion was coated on the copper board and exposed through the negative mask.

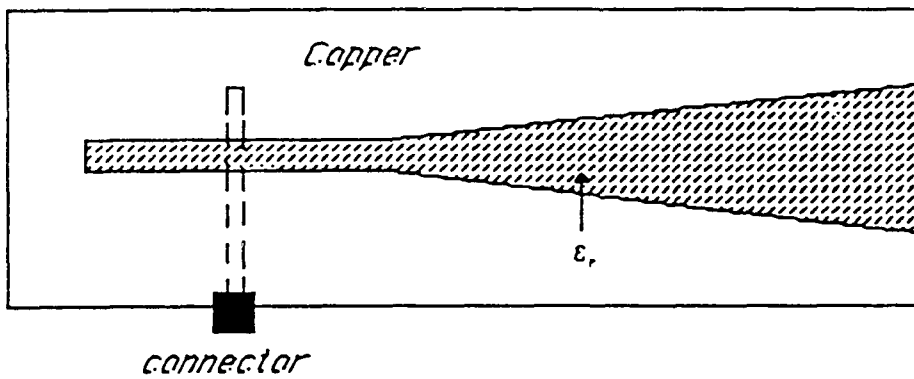
- The board was then agitated through the etcher in order to remove unwanted copper.
- Lastly the board was removed and cleaned using acetone.



(A).No.1A, No.2B



(B).No.1C0



(C).No.1C

Figure 16. Geometry of antenna No.1

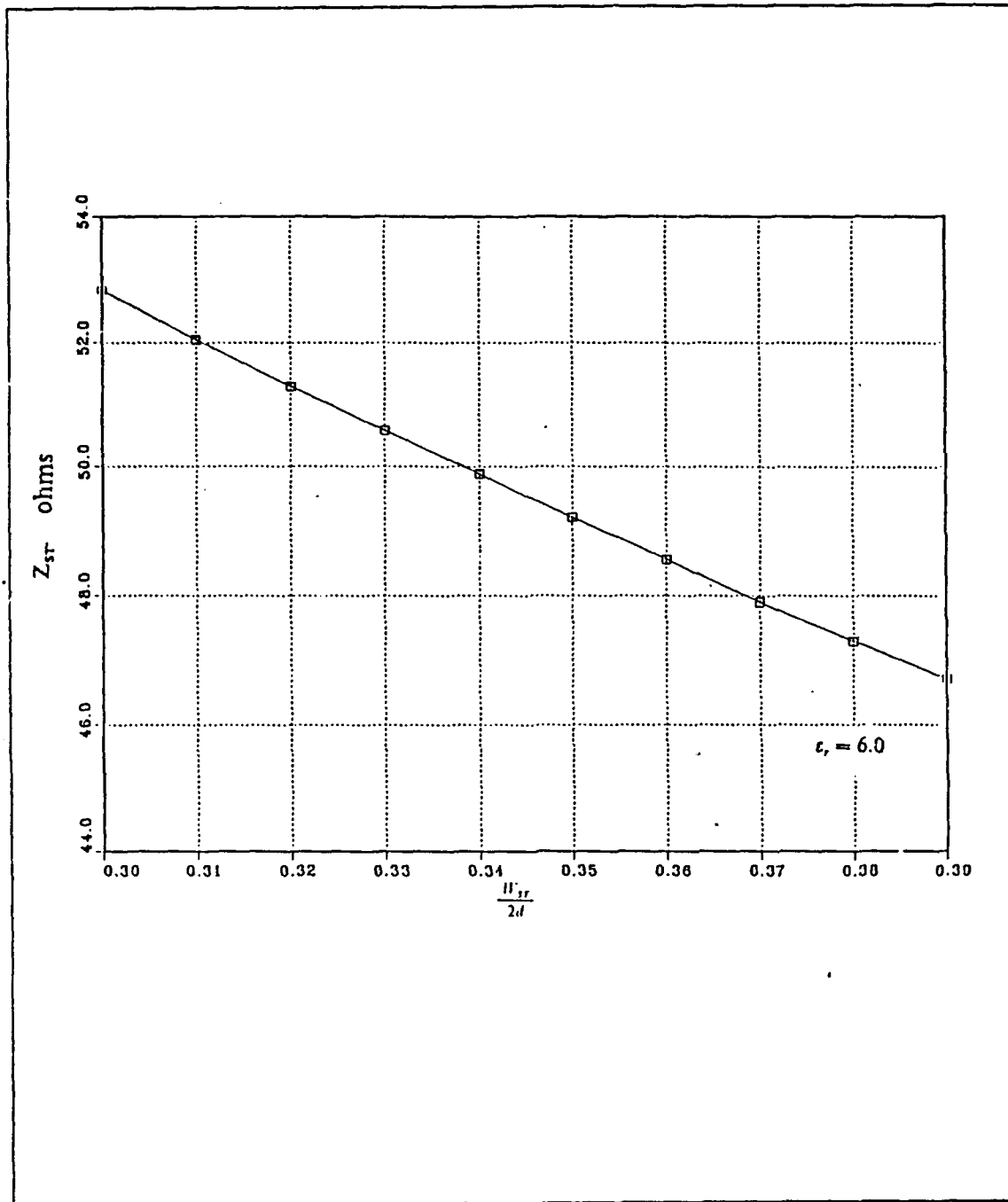


Figure 17. Stripline characteristic impedance versus $W_{sr}/2d$ for impedance near 50 ohm and $\epsilon_r = 6.0$

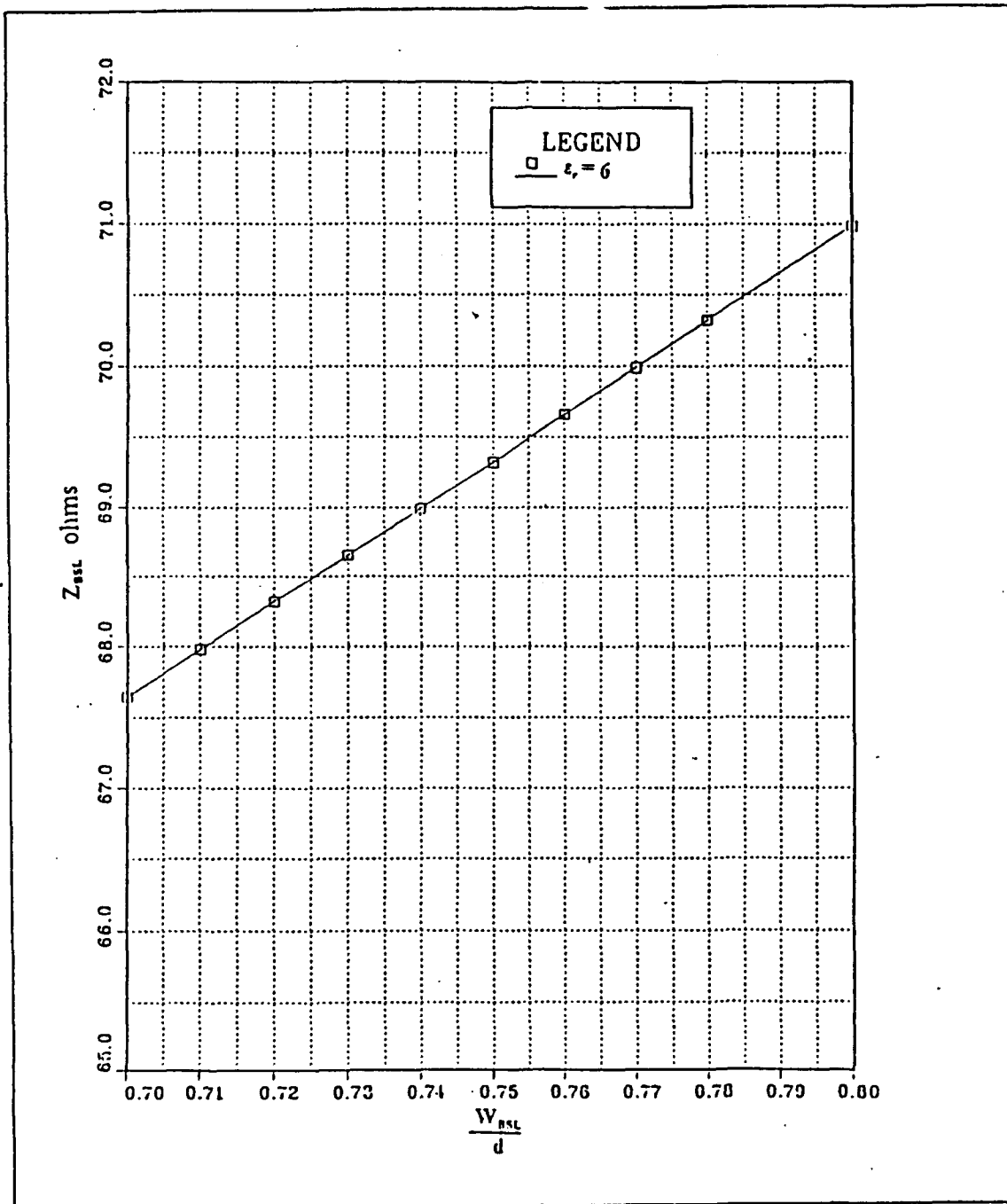


Figure 18. Slotline characteristic impedance versus W_{BSL}/d for impedance near 70 ohm and $\epsilon_r = 6.0$

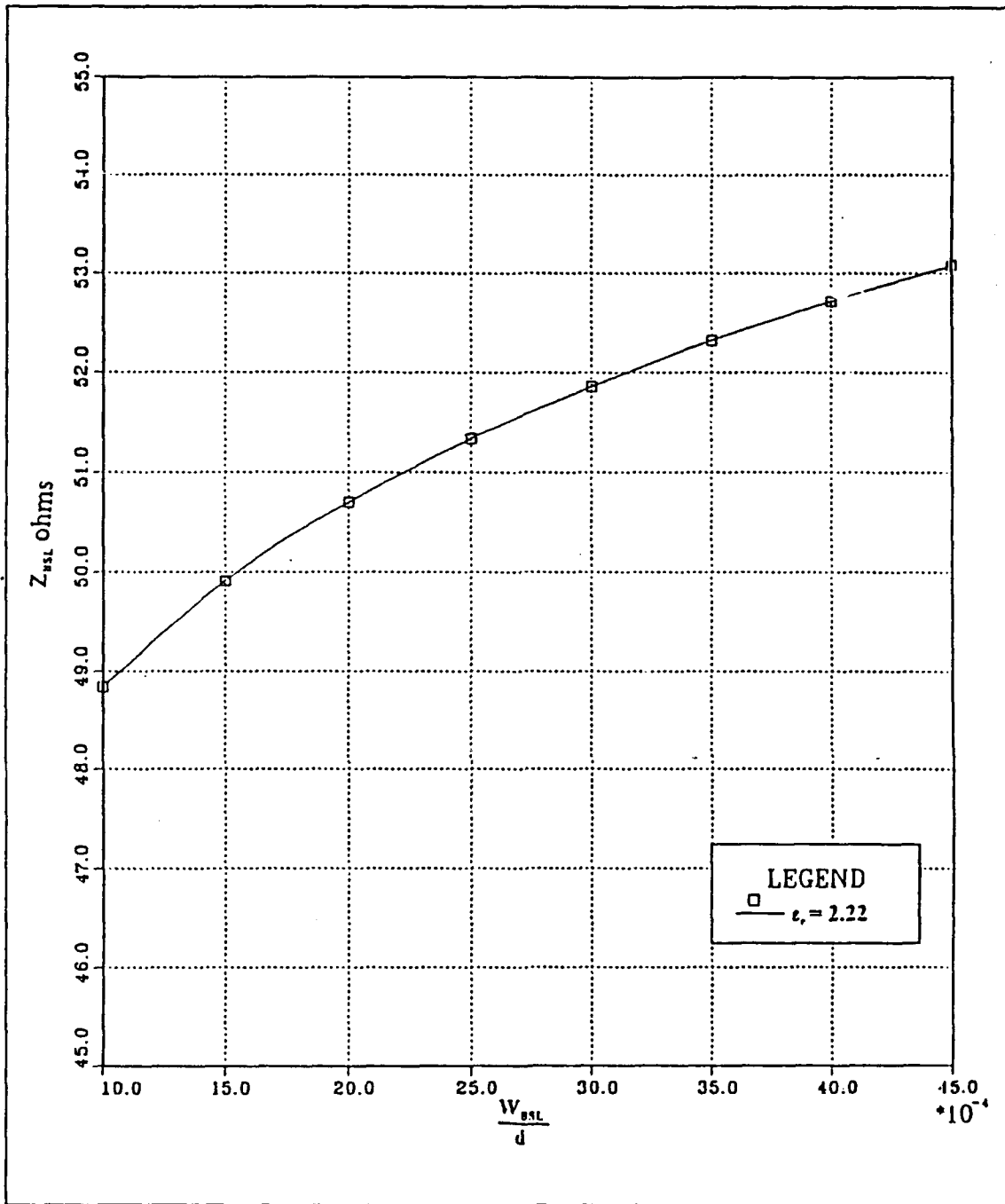


Figure 19. Slotline characteristic impedance versus W_{BSL}/d for impedance near 50 ohm and $\epsilon_r = 2.22$

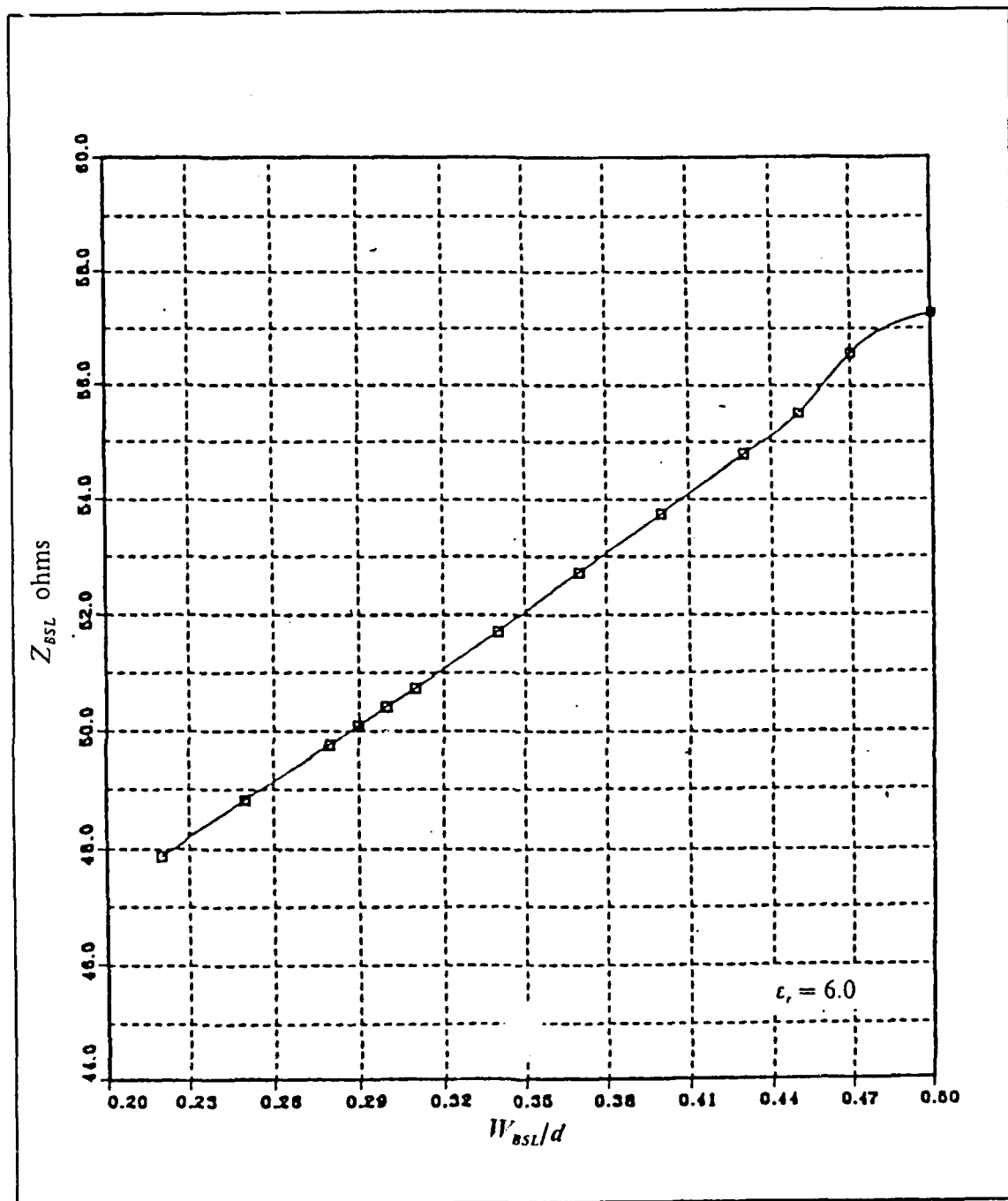


Figure 20. Slotline characteristic impedance versus W_{BSL}/d for impedance near 50 ohm and $\epsilon_r = 6.0$

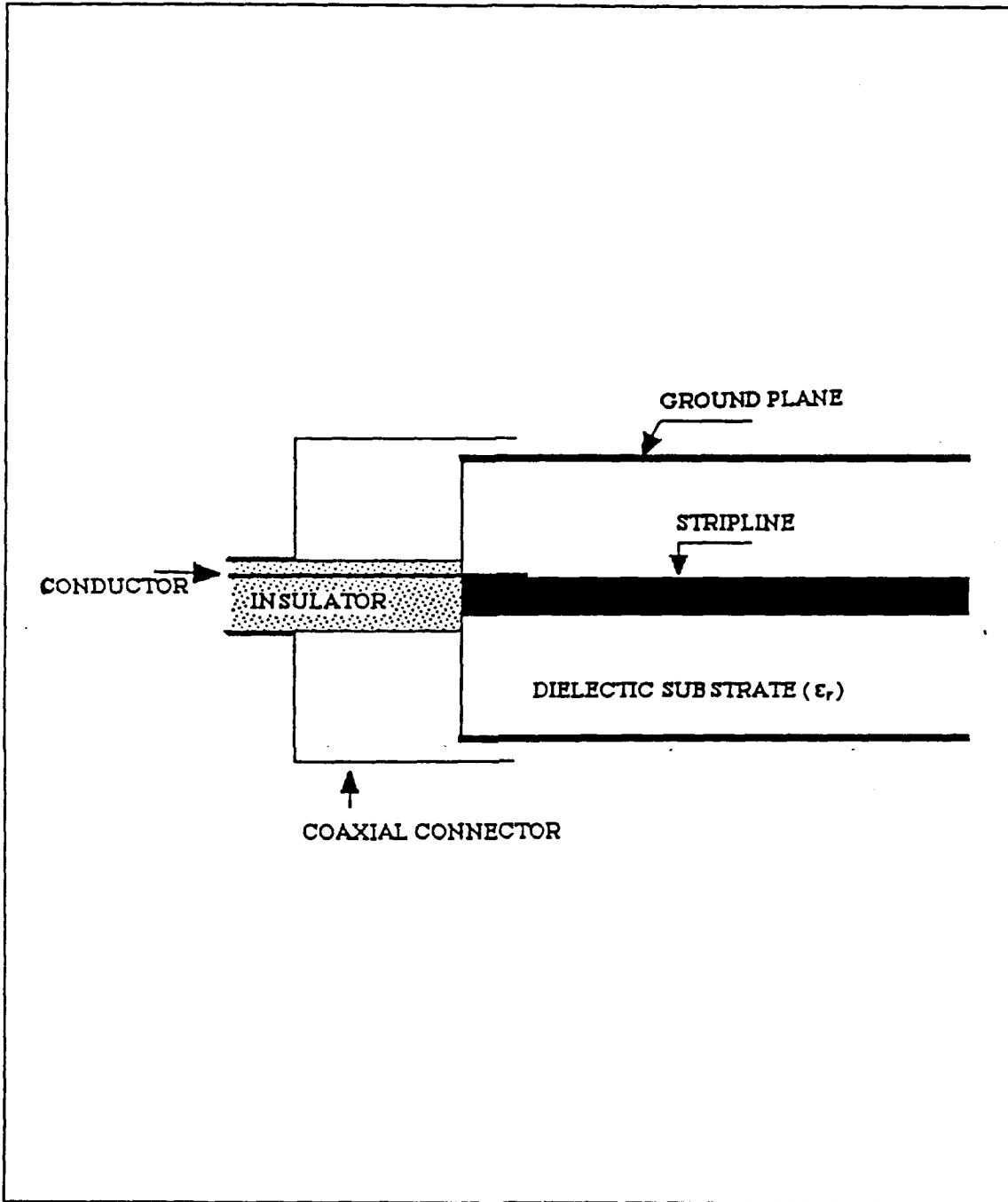
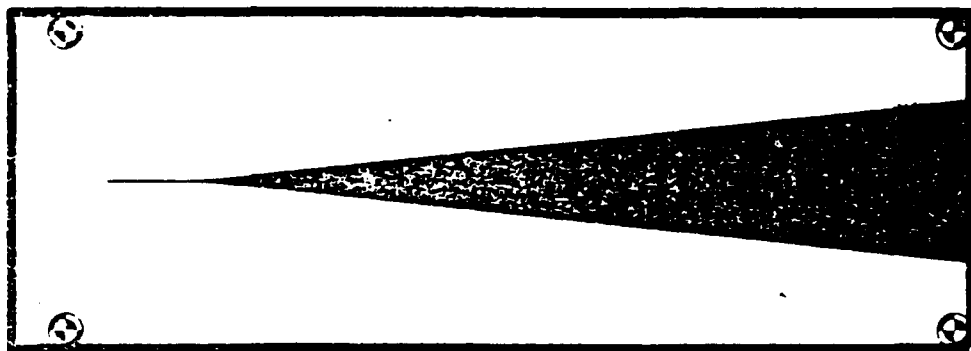


Figure 21. Cross sectional view of the coaxial line to stripline transition.

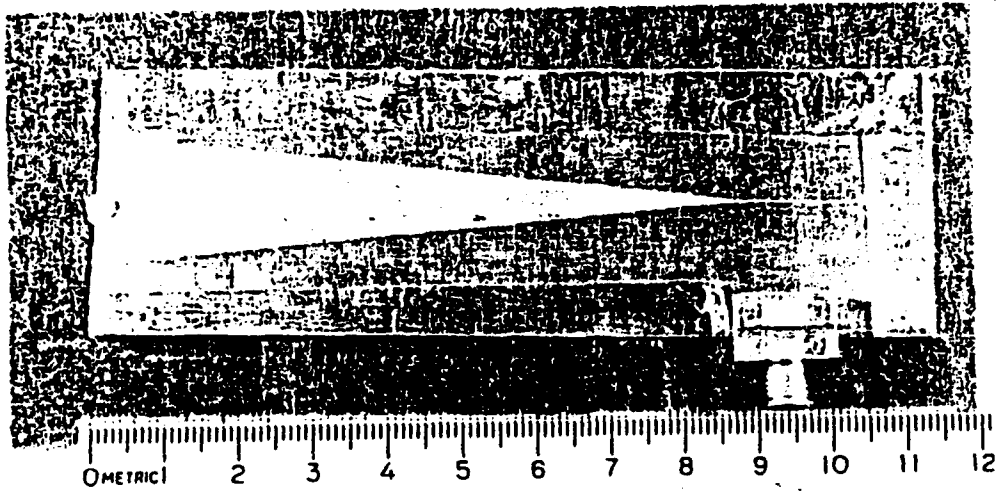


(A)

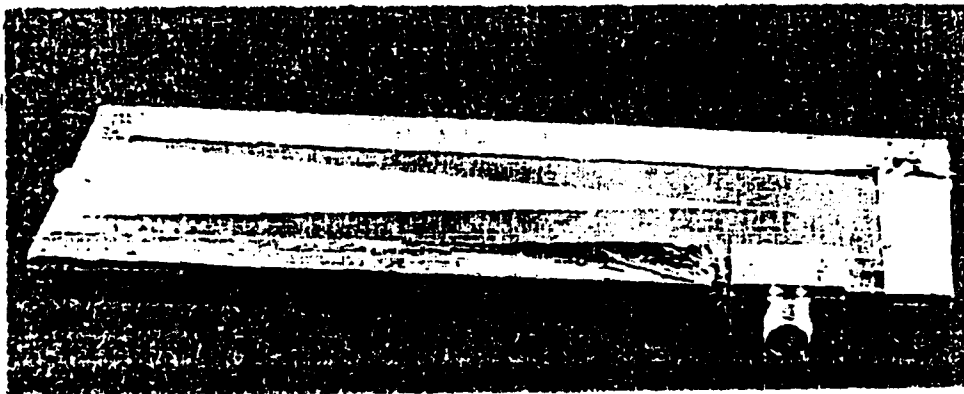


(B)

Figure 22. (A) Positive mask of slotline, and (B) positive mask of stripline for antenna No.3.



(A).Top view of antenna No.3C



(B).Side view of antenna No.3C

Figure 23. Geometry of antenna No.3C

V. ANALYSIS OF MEASUREMENTS

A. BACKGROUND

As it was mentioned before, we will investigate experimentally the behavior of various types of antennas. We summarize here the physical characteristics of the antennas from the previous chapter.

- No.1A: Single-sided LTSA on 25 mil $\epsilon_r = 6.0$, substrate. Dielectric substrate extends beyond the metal along the antenna length by 0.65 cm at the widest slot and by 0.3 cm at the apex (Fig. 16A). The transition is a 50 ohm microstrip line to 70 ohm slotline.
- No.1B: Double-sided LTSA on $\epsilon_r = 6.0$, having 50 mils total substrate thickness. Dielectric substrate extends beyond the metal along the antenna length by 0.65 cm at the widest slot and by 0.3 cm at the apex (Fig. 16A). The transition is a 50 ohm stripline to 70 ohm bilateral slotline.
- No.1CO: Double-sided LTSA on $\epsilon_r = 6.0$, having 50 mils total substrate thickness. Dielectric substrate extends only beyond the apex by 0.3 cm, and 50 ohm stripline to 70 ohm bilateral slotline is used (Fig. 16B).
- No.1C: Double-sided LTSA on $\epsilon_r = 6.0$, having 50 mils total substrate thickness. Dielectric flushed with metal edges. Transition uses 50 ohm stripline to 70 ohm bilateral slot line (Fig. 16C).

Geometry configuration of the following antennas is similar to that of antenna No.1.

- No.2A: Single-sided LTSA on 60 mil $\epsilon_r = 2.33$, substrate. Dielectric substrate extends beyond the metal along the antenna length by 0.2 cm at the widest slot and at the apex. A 50 ohm microstrip to 70 ohm slotline is used.
- No.2B: Double-sided LTSA on $\epsilon_r = 2.33$, having 120 mils total substrate thickness. Dielectric substrate extends beyond the metal along the antenna length by 0.2 cm at the widest slot and at the apex. A 50 ohm stripline to 70 ohm bilateral slot line is used.
- No.2C: Double-sided LTSA on $\epsilon_r = 2.33$, having 120 mils total substrate thickness. A 50 ohm stripline to 70 ohm bilateral slot line is used.
- No.3C: Double-sided LTSA on $\epsilon_r = 6.0$, having 50 mils total substrate thickness. Dielectric flushed with metal edges. A 50 ohm stripline to 50 ohm bilateral slot line is used.

In each of the above cases, the return loss over a frequency band and the radiation pattern in the principal planes were measured. Return loss measurements were carried out using a Hewlett Packard HP-8510B network analyzer. Frequency Domain Reflectometer (FDR) plots were also obtained using the same analyzer. As an example, Fig. 25 shows the (Time Domain Reflectometer) TDR data for antenna No.2C. Re-

flections due to the microstrip line - slotline junction were extracted out from the TDR data as follows: The TDR graph was multiplied by a rectangular pulse with appropriate width so that the remaining TDR graph contains only the required return loss as shown in Fig. 25. The frequency version of data in Fig. 24 and Fig. 25 are depicted in Fig. 35A and Fig. 35B, respectively. (We have to note that the symbols seen in Fig. 24 have no correlation to those shown in Fig. 2). From Fig. 24 we may say that segment A'B' of the TDR plot corresponds to the return loss due to the connector. Segment C'D' is due to reflections at the junction of the stripline and the slotline and those due to the end of stripline (point D in Fig. 2) and the end of the slotline (point B in Fig. 2). Also, segment E'F' is due to reflections at the antenna mouth. The above statements were verified experimentally by putting a movable reflecting barrier at the position of the connector, the junction, and the antenna mouth. It is also verified theoretically as follows:

The electromagnetic wave travels inside the stripline of antenna No.2C with speed

$$v_{ST} = \frac{c}{\sqrt{\epsilon_r}} = \frac{3 \times 10^{10}}{\sqrt{2.33}} = 1.966 \times 10^{10} \text{ cm/s} . \quad (70)$$

The round trip distance between the connector and the junction of the stripline and the slotline is $2 \times 2.45 \text{ cm} = 4.9 \text{ cm}$. The e/m wave takes 0.25 ns to travel this distance, and this time corresponds to the first peak of segment C'D' as is shown in Fig. 24. The ϵ_{eff} of the bilateral slotline at the apex is 1.5, while at the antenna mouth it is 1.2. The approximation for the average ϵ_{eff} , is $\epsilon_{aveff} = (1.5 + 1.2)/2 = 1.35$. The wave travels the round trip distance between the junction of the stripline and the slotline and the antenna mouth with an average speed v_{av} .

$$v_{av} = \frac{c}{\sqrt{\epsilon_{aveff}}} = \frac{3 \times 10^{10}}{\sqrt{1.35}} = 2.58 \times 10^{10} \text{ cm/s} . \quad (71)$$

The roundtrip distance is $2 \times 9.6 = 19.2 \text{ cm}$ and the time it takes for the pulse to travel this distance at v_{av} is approximately 0.74 ns. This is very close to that of the first peak in the segment E'F' observed in Fig. 24.

All measurements were done by using the test antenna as a receiving antenna in free reflection environment. A transmitter at a distance of about 60 meters placed the receiving antenna in the far-field zone. In order to minimize influences from reflection of the base where the test antenna is mounted, the base was covered by a thick absorbing

material. All measurements were performed in the Naval Weapons Center in China Lake, CA.

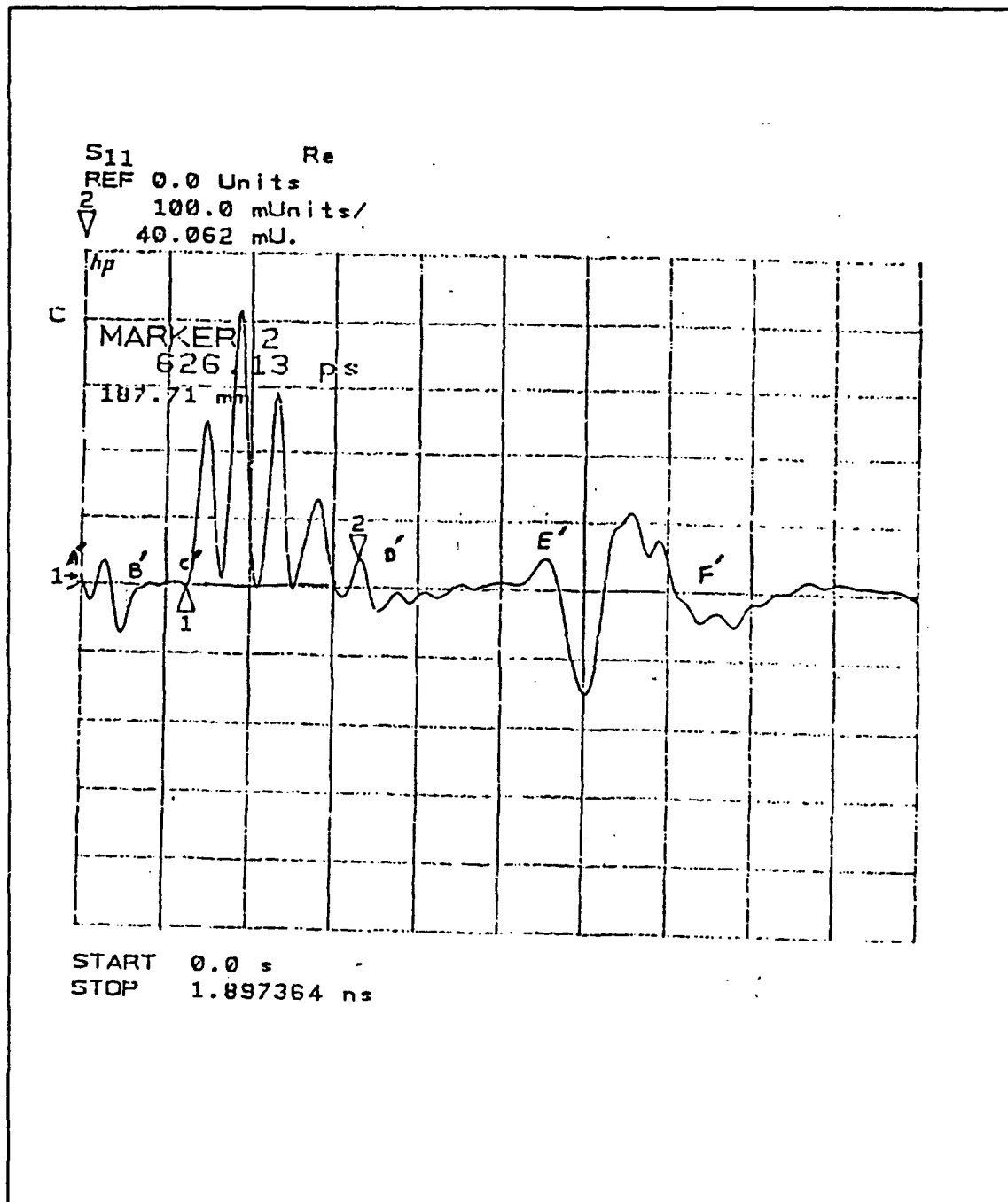


Figure 24. Total return loss TDR of antenna No.2C

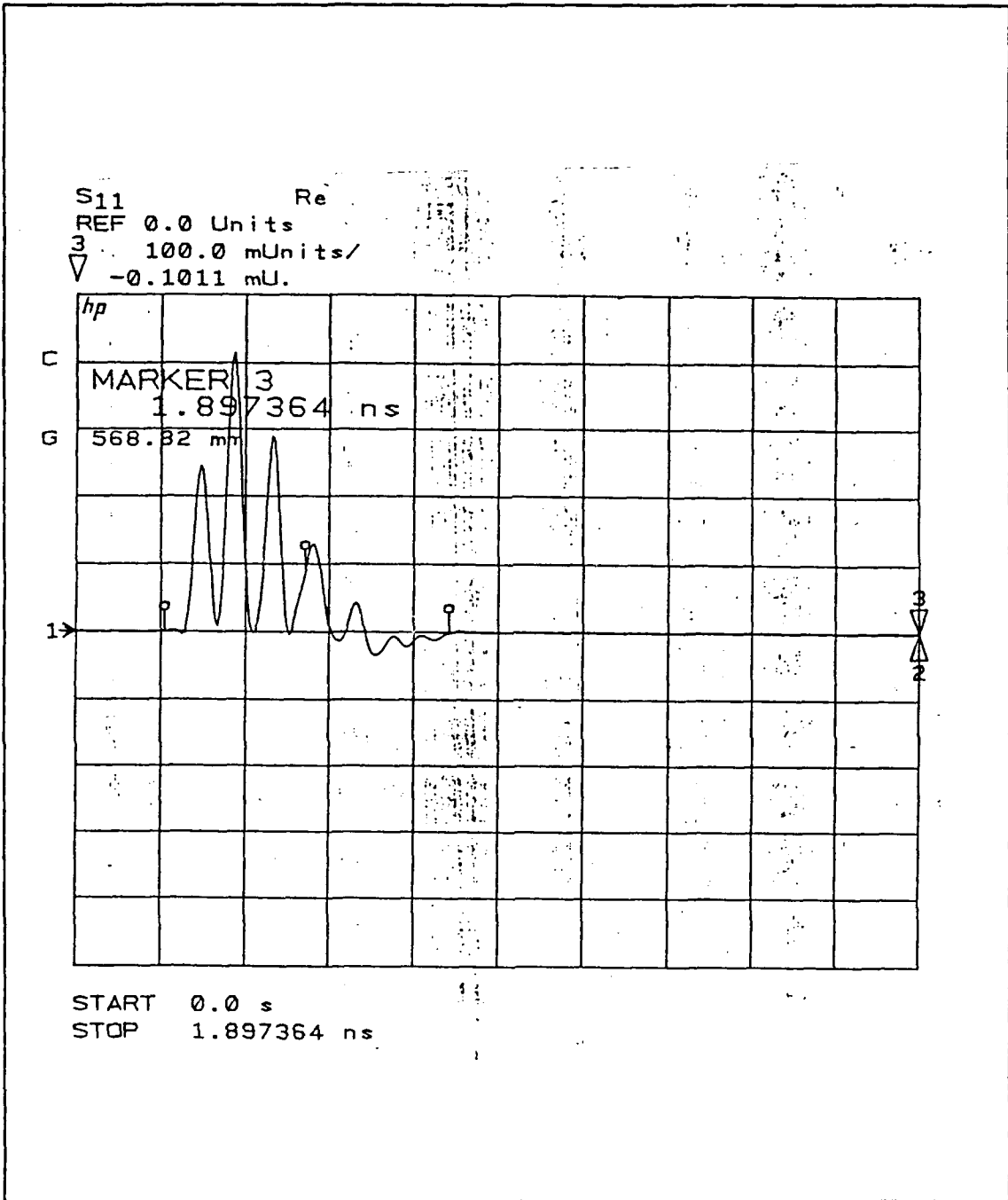


Figure 25. Return loss TDR of antenna No.2C due to reflections at the junction of the stripline and the BSL

B. EFFECT OF DIELECTRIC CONSTANT AND ANTENNA STRUCTURE

1. LTSA

As it was mentioned before, the difference between antenna No.1 and No.2 is in the dielectric constant of the substrate. Antenna No.1 uses a substrate with $\epsilon_r = 6.0$ and $d = 0.635$ mm, where as antenna No.2 uses $\epsilon_r = 2.33$ and $d = 1.57$ mm.

In Fig. 26, we plot the 3-dB beamwidth and the side lobe level as a function of frequency for antennas No.1A and No.2A. In antenna No.2, both the H-plane and E-plane beamwidth decrease as the frequency increases. The 3-dB beamwidth in the H-plane of antenna No.1A remains almost constant at 38° as the frequency increases from 6 GHz to 9 GHz. However, in the case of antenna No.2A, the H-plane beamwidth decreases linearly with frequency from 70° - 30° . From Fig. 26B, we see that antenna No.2A gives slightly lower Side Lobe Level (S.L.L.) than antenna No.1A. Also we can note that for both antennas, the S.L.L. is higher in the H-plane than in the E-plane.

Both the H-plane and E-plane beamwidth change as ϵ_r changes. Side lobe level improves as the ϵ_r decreases as illustrated in Fig. 26B. Detailed plots of the radiation pattern for antenna No.2A are included in Fig. 64-68 of Appendix A. Antenna No.2A produces a more symmetric beam than No.1A.

Figure 27A shows the total return loss for antenna No.1A. It varies in the range -4 dB to -22 dB over the frequency range 4 to 9 GHz. Return loss for the designed frequency $f_o = 7.087$ GHz is -17 dB, while a lower total return loss of -22 dB occurs at 5.9 GHz. In the frequency range 7.7 to 8.3 GHz, the observed return loss is smaller than -10 dB.

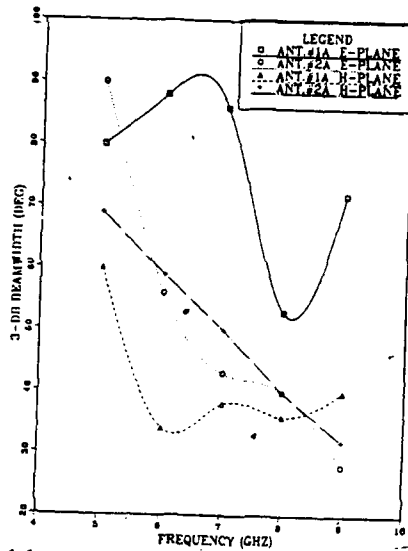
Figure 27B illustrates the total return loss for antenna No.2A. Return loss is between -5 dB and -30 dB over the frequency range 4-9 GHz. At the design frequency $f_o = 6.67$ GHz, the return loss is -8 dB. The lowest return loss of -30 dB occurs at a frequency 9 GHz. In the frequency range 8.2 to 9.4 GHz, the loss is lower than -15 dB. The next lower loss of -25 dB occurs at a frequency of 4.8 GHz. It is apparent that the lower dielectric constant substrate provides lower total return losses. Return loss in time domain is given in Fig. 28.

In Fig. 29, we compare the bilateral slot line versions (No.1B and No.2B) of antennas No.1A and No.2A. In Fig. 29A we plot the 3-dB beamwidth versus frequency while in Fig. 29B, the variation of Side Lobe Level (S.L.L.) with frequency is plotted. It is seen that the E-plane pattern is more sensitive to frequency than the H-plane. Further, the side lobe level of antenna No.1B is more or less independent of frequency beyond 7 GHz.

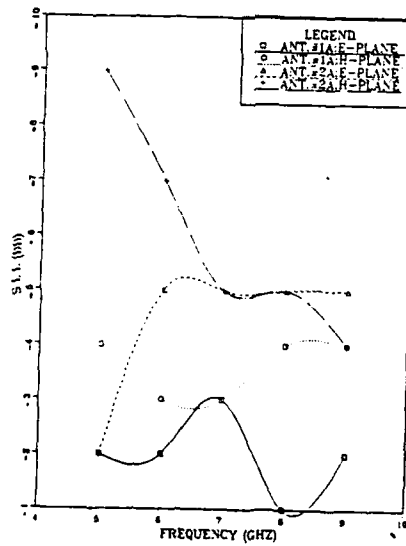
Figure 30 shows the FDR and TDR return loss of antenna No.1B. Total return loss of antenna No.1B (Fig. 30A) varies between -5 dB and -25 dB over the frequency range 4 - 8 GHz. At the design frequency $f_0 = 7.087$ GHz, the total return loss is -13 dB. A minimum return loss of -25 dB is obtained at 6.2 GHz. In contrast to antenna No.1A, lower return loss is obtained at 5.9 GHz.

Return loss data for antennas No.1C and No.1CO are shown in Fig. 31. For antenna No.1CO, the lowest total return loss of -25 dB occurs at 6.3 GHz. Figure 31B shows the total return loss of antenna No.1C. A comparison between Fig. 31A and Fig. 31B indicates that the extra substrate at the back-end does not affect the return loss. Figure 32 illustrates the TDR data of antenna No.1CO and No.1C.

To summarize, we see that lower dielectric constant provides lower total return loss. Also the extra substrate in the front-end of the antenna affects (reduces) the return loss while extra substrate in the back-end does not affect return loss and antenna performance.

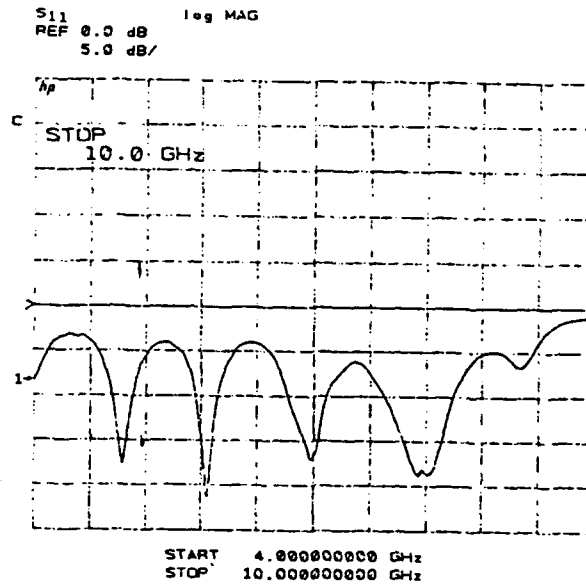


(A) 3-dB beamwidth

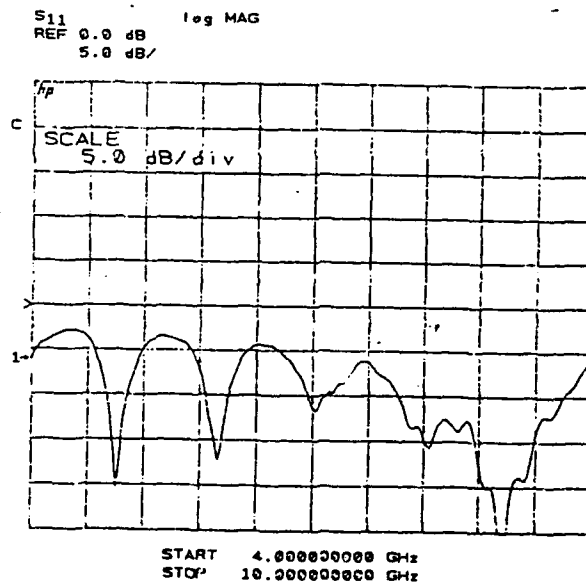


(B) Side lobe level

Figure 26. 3-dB beamwidth and side lobe level (S.L.L.) as a function of frequency: ($\epsilon_r = 6.0$ for antenna No.1A, and $\epsilon_r = 2.33$ for antenna No.2A.)

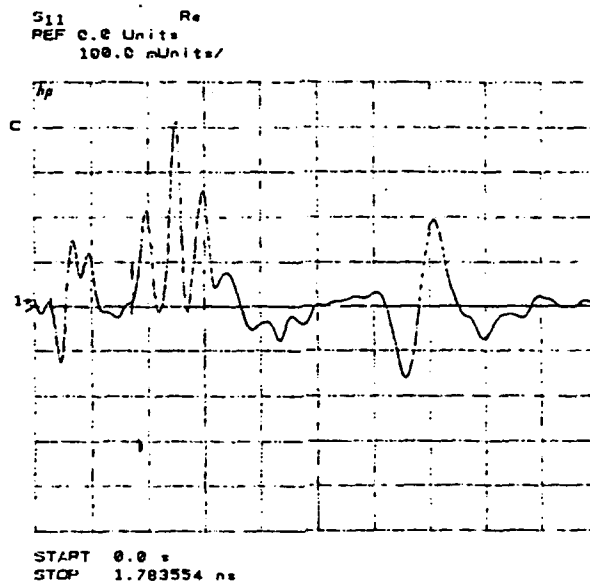


(A) FDR of antenna No.1A

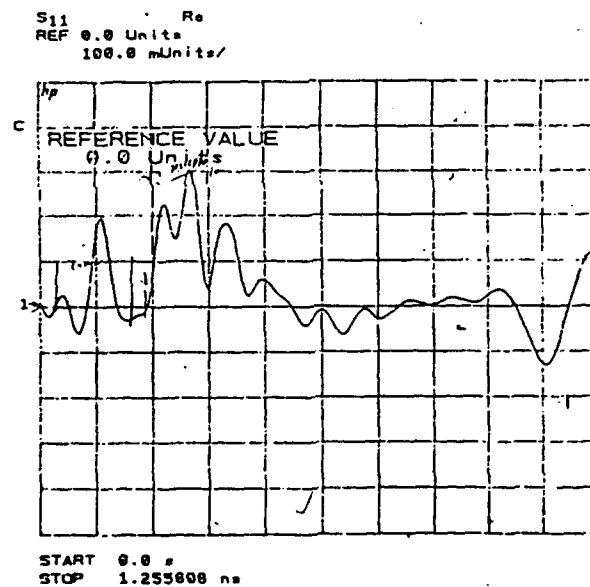


(B) FDR of antenna No.2A

Figure 27. Total return loss (FDR) as a function of frequency: ($\epsilon_r = 6.0$ for antenna No.1A and $\epsilon_r = 2.33$ for antenna No.2A)

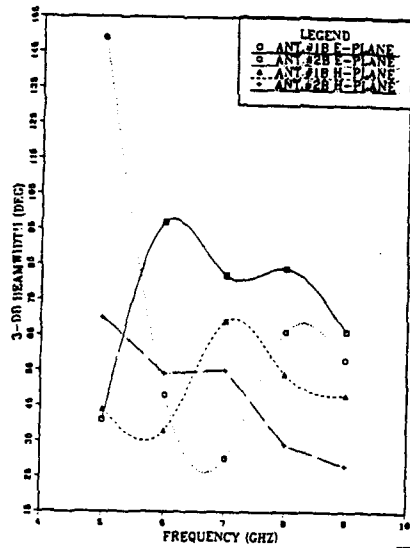


(A) TDR of antenna No.1A

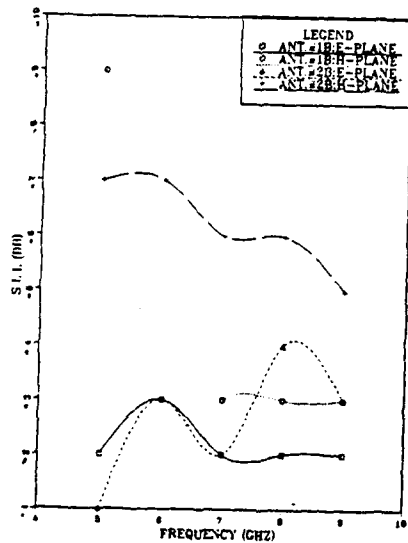


(B) TDR of antenna No.2A

Figure 28. Total return loss (TDR) as a function of frequency: ($\epsilon_r = 6.0$ for antenna No.1A, $\epsilon_r = 2.33$ for antenna No.2A.)

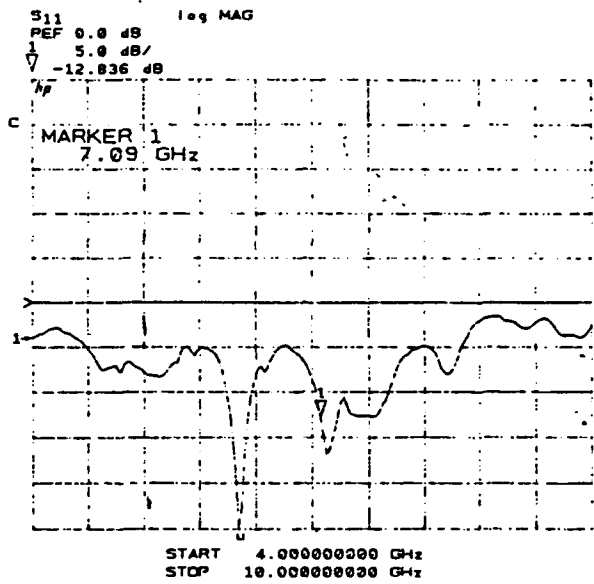


(A) 3-dB beamwidth

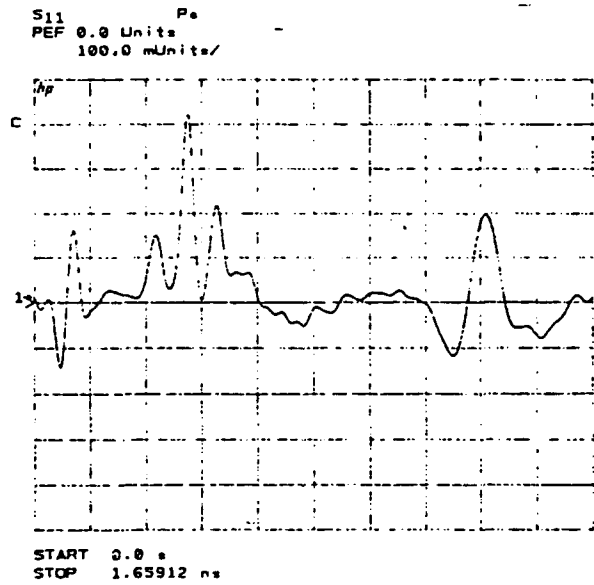


(B) Side lobe level

Figure 29. 3-dB beamwidth and side lobe level (S.L.L.) as a function of frequency: ($\epsilon_r = 6.0$ for antenna No.1B, $\epsilon_r = 2.33$ for antenna No.2B.)

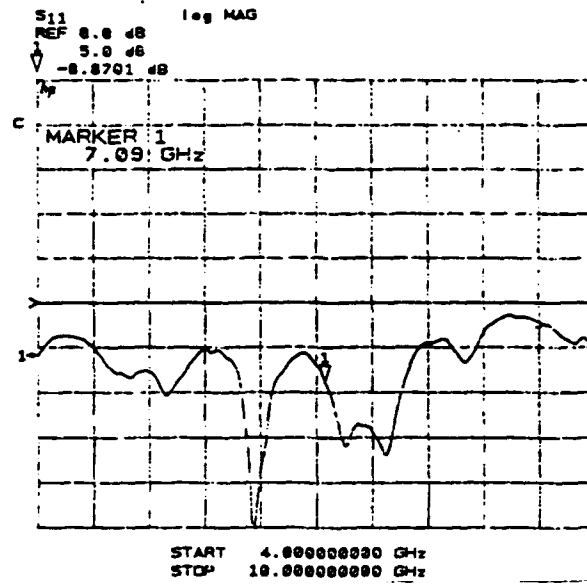


(A) FDR

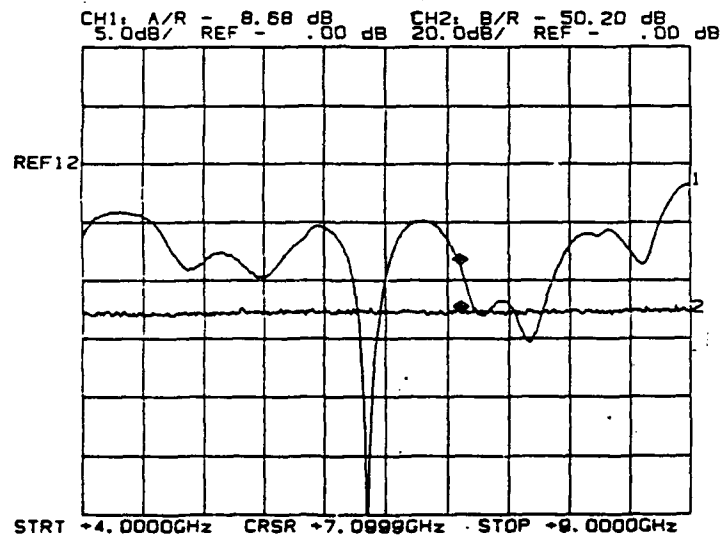


(B) TDR

Figure 30. Total return loss for antenna No. 1B

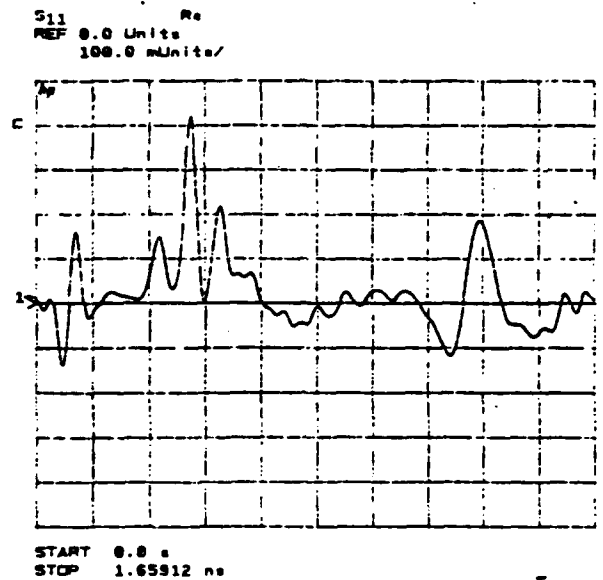


(A) FDR of antenna No.1C0

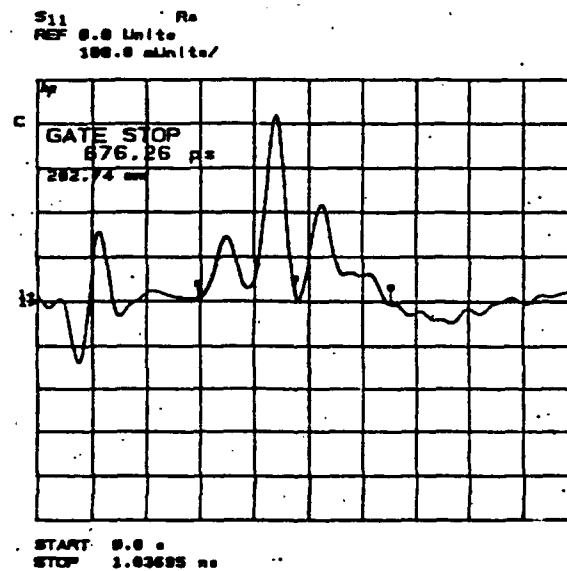


(B) FDR of antenna No.1C

Figure 31. Total return loss (FDR) as a function of frequency: ($\epsilon_r = 6.0$ for antenna No.1C0 and No.1C)



(A) TDR of antenna No.1C0



(B) TDR of antenna No.1C

Figure 32. Total return loss (TDR) as a function of frequency: ($\epsilon_r = 6.0$ for antenna No.1C0 and No.1C)

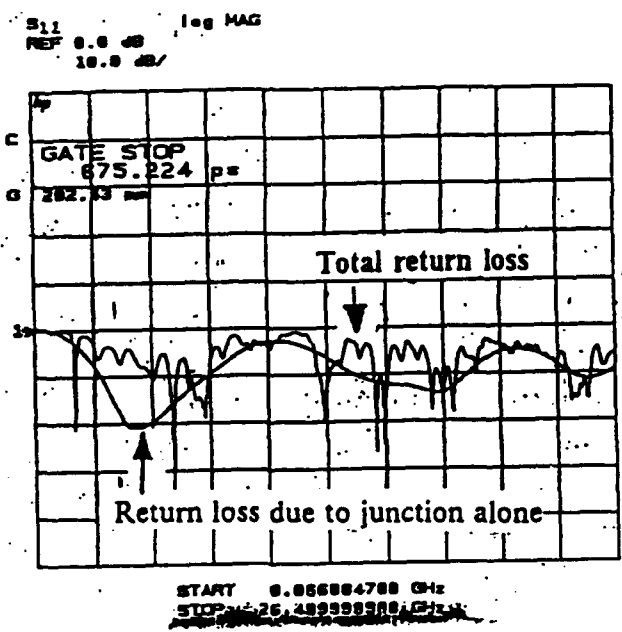
The return loss due to the stripline-slotline junction alone for antenna No.1CO is shown in Fig. 33A. In Fig. 33A, the total return loss is shown as a wiggly curve, whereas the smooth curve is due to the stripline-slotline junction. The minimum loss of -33 dB occurs at approximately 6.7 GHz, while, at the design frequency of 7.087 GHz, it is -13 dB. After cutting the extra back-end substrate from antenna No.1CO, antenna No.1C is formed. Results for this case are shown in Fig. 33B. We see from the figure that the return loss is -27 dB at 6.7 GHz. This is about 5 dB more than for case No.1CO.

In Fig. 34 we compare the radiation characteristics of antennas No.1C and No.2C. It is seen that for antenna No.2C both the beamwidth and the S.L.L. in the E-plane generally decrease as the frequency increases.

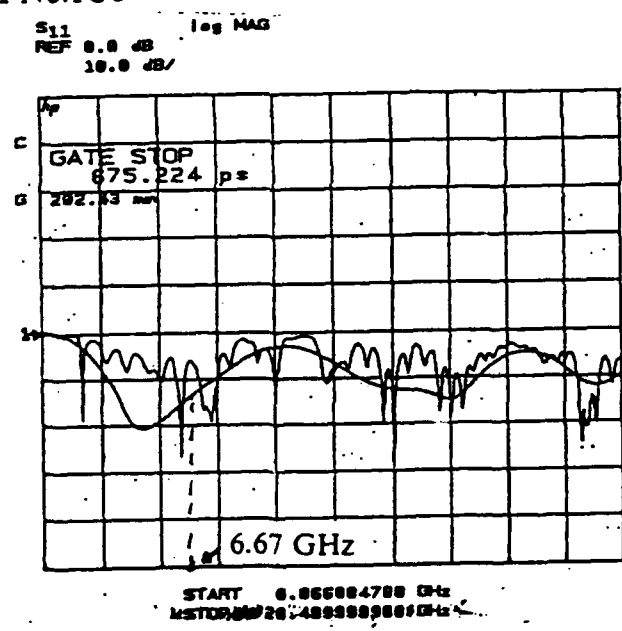
Figure 31B shows the total return loss of antenna No.1C and Figs. 35A and 35B show the total return loss of antenna No.2C. From Fig. 35A we observe that over the frequency band 5.8-9 GHz, the total return loss is less than -10 dB. The lowest loss (-25 dB) occurs at 8.8 GHz. Almost in the entire test range of 4-10 GHz, the loss remains less than -5 dB. At the design frequency of 6.67 GHz, the return loss is -12 dB. A comparison between Fig. 31B and Fig. 35A shows that antenna No.2C provides lower return loss for a wider frequency band than antenna No.1C. We can conclude that with the lower dielectric substrate ($\epsilon_r = 2.33$) a lower return loss and improved antenna performance will result. This statement is well supported by the fact that (Fig. 32) the H-plane beamwidth of No.2C is narrower than that of antenna No.1C. However in the E-plane, the beamwidths differ only slightly.

More detailed information for return loss of antenna No.2C due to stripline to slotline junction are provided by examining Fig. 35B. Figure 35B shows that in the entire test range (2.7-10.0 GHz), the return loss is less than -10 dB. At the design frequency of 6.67 GHz, the loss is -25 dB. It can be seen that antenna No.2C provides a match over a wider frequency band.

Figure 33 illustrates data for the same transition scheme as with Fig. 35B except that it is valid for $\epsilon_r = 6.0$. Comparison between these figures shows that in Fig. 33B (antenna No.1C) the return loss is suppressed below -10 dB (with a minimum of -20 dB) over the band 2.8-8 GHz, while in Fig. 35A we have a wider frequency band (2.7-10.0 GHz) over which the return loss is suppressed below -10 dB.

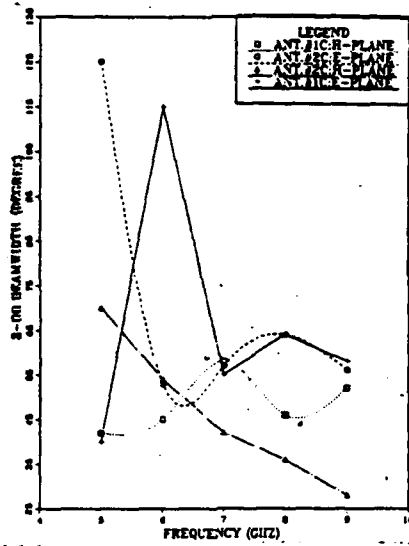


(A) Antenna No.1CO

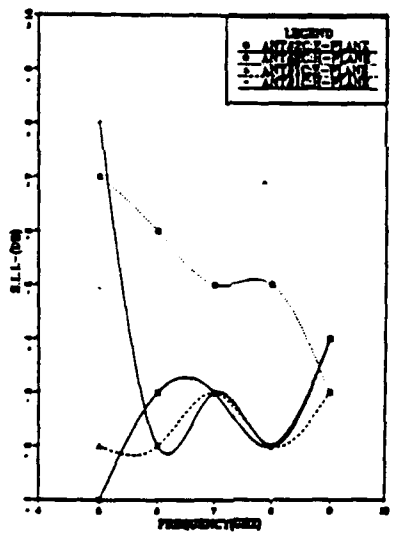


(B) Antenna No.1C

Figure 33. Return loss due to junction alone as a function of frequency: ($\epsilon_r = 6.0$ for antenna No.1CO and No.1C)

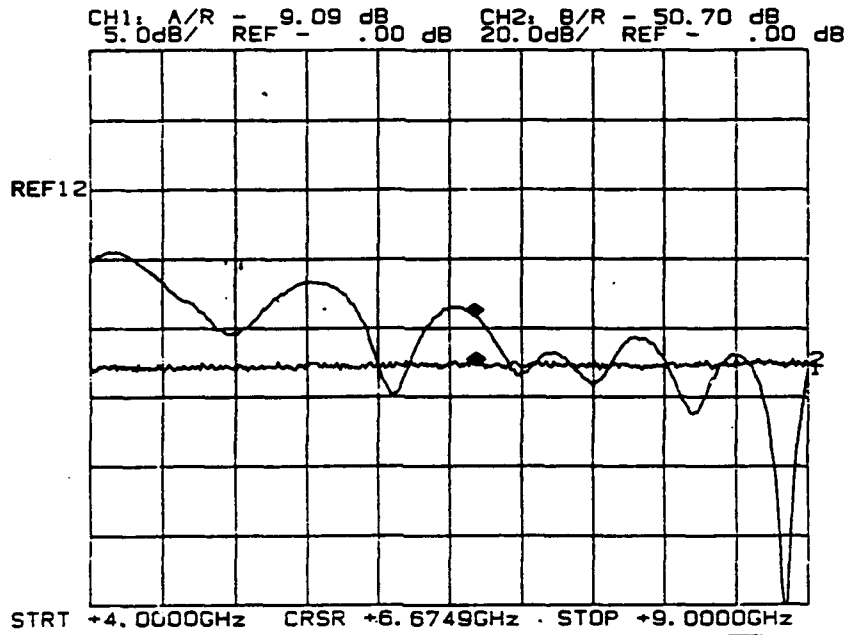


(A) 3-dB beamwidth

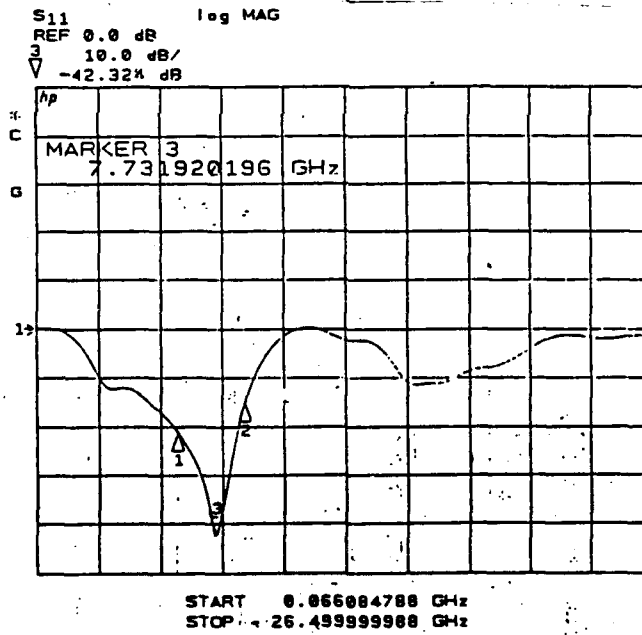


(B) Side lobe level

Figure 34. 3-dB beamwidth and side lobe level (S.L.L.) as a function of frequency: ($\epsilon_r = 6.0$ for antenna No.1C, $\epsilon_r = 2.33$ for antenna No.2C)



(A)



(B)

Figure 35. Total return loss (A) and return loss due to junction only (B) as a function of frequency: ($\epsilon_r = 2.33$ for antenna No.2C)

2. LTSA, BSL Antenna

Comparison of antenna No.1A versus antenna No.1B and No.2A versus No.2B shows the effect of antenna structure on antenna performance.

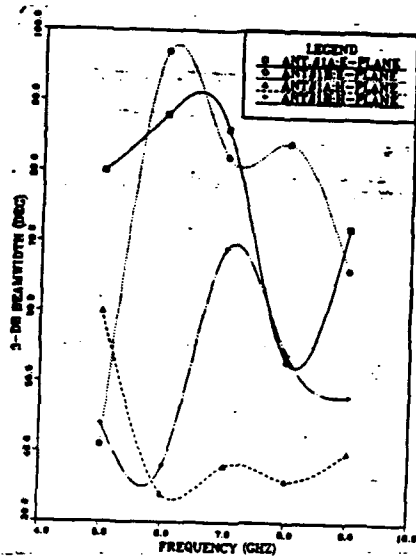
Figure 36 shows the comparison between antenna No.1A and No.1B, whereas Fig. 37 shows the comparison between antenna No.2A and No.2B. For antenna No.1B the E-plane beamwidth remains larger than the H-plane beamwidth. The E-plane beamwidth and H-plane beamwidth of antenna No.1B are larger than the corresponding beamwidths of antenna No.1A.

The H-plane beamwidth of antenna No.2B is smaller than that of antenna No.2A. However, antenna No.2A produces a more-or-less symmetric beam. It can be noted that both the E-plane and H-plane beamwidths of antenna No.2A exhibit the well-known decreasing trend with increasing frequencies. Moreover, No.2A has superior sidelobe performance in the E-plane than antenna No.2B.

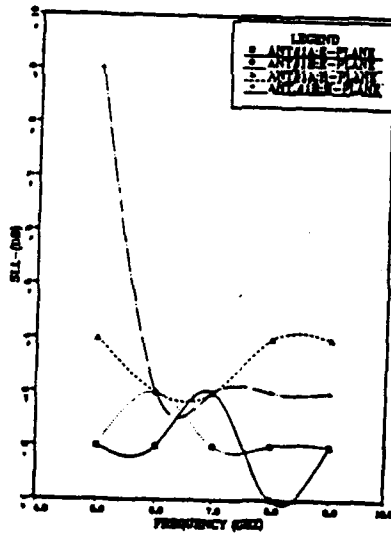
Figure 38 demonstrates the effects of changing antenna structure on the 3-dB beamwidth. Figures 44-53 present radiation patterns for antenna No.1A and No.1B and Figs. 64-73 present radiation patterns for antenna No.2A and No.2B.

Comparison of Fig. 27A and Fig. 30A demonstrates the effect of changing antenna structure (from LTSA in Fig. 27A to BSL antenna in Fig. 30A) on the return loss. From Fig. 27A it can be seen that we have minimum return loss approximately every 1 GHz (wavelength at which corresponds to three times the antenna length), starting from 4.9 GHz. In general, the return loss of antenna No.1A is larger than that of No.1B. As expected a change in antenna structure results in a change in return loss.

Comparing the radiation pattern of antennas No.2B (Figs. 69-73) and No.1B (Figs. 49-53) shows that the H-plane and E-plane patterns of antenna No.2B are better than those of antenna No.1B. Change of dielectric constant ϵ , from 6.0 to 2.33 improves the beamshape of the radiation pattern and decreases the side lobe level.

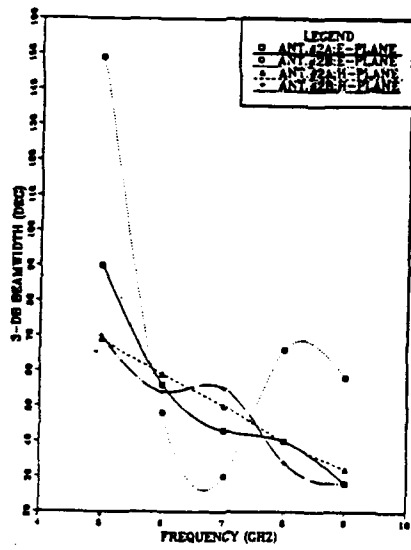


(A) 3-dB beamwidth

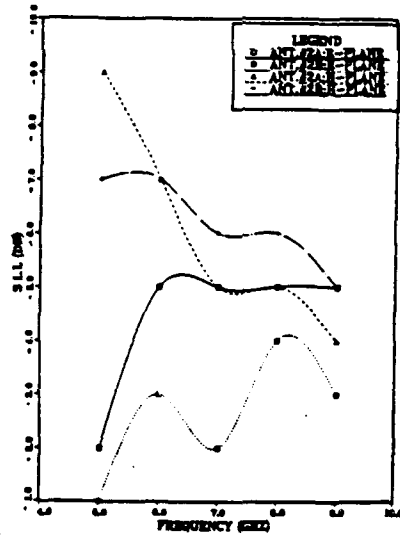


(B) Side lobe level

Figure 36. 3-dB beamwidth and side lobe level (S.L.L.) as a function of frequency: ($\epsilon_r = 6.0$ for antenna No.1A and No.1B)

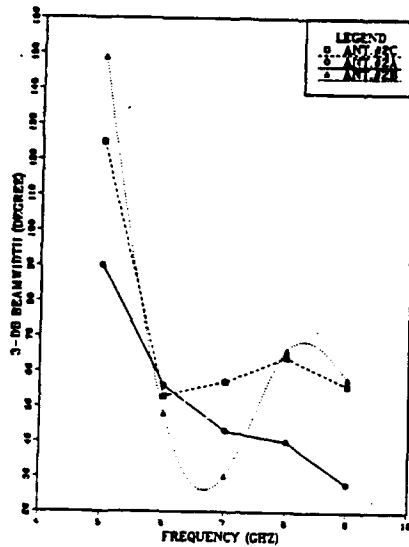


(A) 3-dB beamwidth

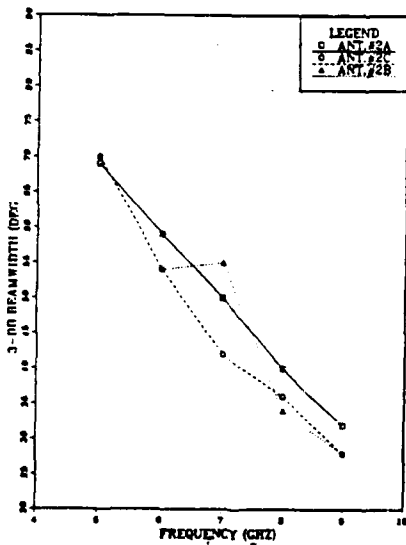


(B) Side lobe level

Figure 37. 3-dB beamwidth and side lobe level (S.L.L.) as a function of frequency: ($\epsilon_r = 2.33$ for antenna No.2A and No.2B)



(A) E-plane



(B) H-plane

Figure 38. 3-dB beamwidth as a function of frequency: ($\epsilon_r = 2.33$ for antenna No.2A, No.2B and No.2C)

3. BSL ANTENNA

The effect of the extra dielectric substrate together with the use of different dielectric substrates is seen from the comparison between antenna No.1B and No.1C, and between antenna No.2B and No.2C. BSL antenna behavior as a function of extra dielectric substrate is characterized in Fig. 39, for antennas No.1B and No.1C. In Fig. 40, No.2B and 2C are compared. We observe that the extra dielectric substrate in both of front and back-end of the antenna reduces antenna performance. In the case of antenna No.2C, the E-plane beamwidth is wider than the H-plane beamwidth, while in the case of antenna No.2B, the E-plane beamwidth becomes narrower than the H-plane beamwidth in the region 6-7 GHz. In the case of antennas No.1B and No.1C we note that the absence of extra substrate had the effect of narrowing the E-plane beamwidth of antenna No.1C compared to that of antenna No.1B. At the designed frequency, antenna No.1C has an E-plane beamwidth that is 27° narrower than that of antenna No.1B. Also its H-plane beamwidth is 11° narrower than that of No.1B. As the frequency increases, the difference in beamwidth between the two types of antenna becomes smaller and at frequency 8 GHz the difference is close to 8° . Again at 9 GHz, antenna No.1C has a wider beamwidth than antenna No.1B. Return loss effects of extra substrate are illustrated in Fig. 30A and Fig. 31B. Figure 31B shows that for antenna No.1C, in the overall band of 4-9 GHz, we have an improvement in return loss of approximately 2 dB than that of No.1B. In conclusion, we have an improvement in the antenna radiation pattern after the extra substrate is removed.

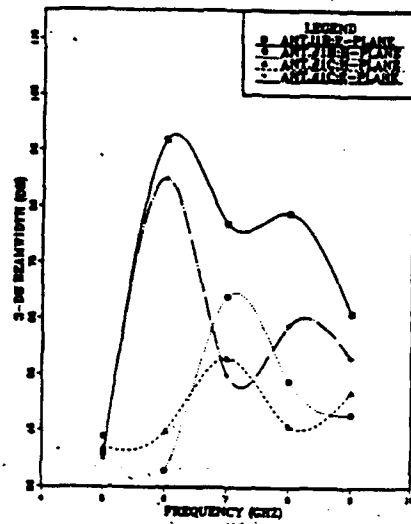
C. EFFECT OF CHARACTERISTIC IMPEDANCE

The only difference between antennas No.1C and No.3C is the value of the characteristic impedance Z_{BSL} . Antenna No.1C has a Z_{BSL} of 70 ohms and No.3C has a Z_{BSL} of 50 ohms. Figure 41 shows the effect of different bilateral slotline impedance. In the E-plane beamwidth, the experiments reveal a narrower beamwidth of antenna No.1C over the entire frequency range. At the designed frequency $f_o = 7.087$ GHz, the difference is as large as 31° . The H-plane beamwidth of antenna No.1C at 7 GHz and at 8 GHz are narrower than those of antenna No.3C. At the designed frequency $f_o = 7.087$ GHz, the difference is 17° . At most frequencies, antenna No.1C is superior to antenna No.2C as it can be seen from radiation patterns (Fig. 59-63 and Fig. 74-78).

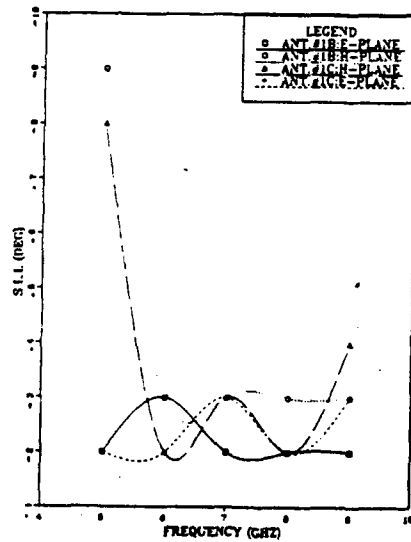
A comparison between Fig. 31 and Fig. 33B, with Fig. 35 and Fig. 42 shows that return loss is affected by changes in slotline characteristic impedance. Return loss for antenna No.3C from the stripline slotline junction alone is illustrated in Fig. 42B. It is

observed from Fig. 33B that antenna No.1C gives a lower return loss over a wide frequency band 2.7-8 GHz. Antenna No.3C junction gives a higher return loss at some frequencies as depicted in Fig. 42. The total loss of antenna No.1C at a frequency of 6.4 GHz is -28dB, while No.3C produces -12dB. Comparison shows that the transition scheme from 50 ohm to 70 ohm is superior to the 50 ohm to 50 ohm scheme. TDR plots for antenna No.3C are given in Fig. 43.

To conclude, antenna No.1C, which has $Z_{BSL} = 70$ ohm and $Z_{ST} = 50$ ohm, behaves better than antenna No.3C which has $Z_{BSL} = Z_{ST} = 50$ ohm. We would have expected better performance of No.3C if the BSL supported a TEM mode like the stripline. However, the mode inside a BSL is non-TEM, and a 50 ohm - 70 ohm transition performs better than the 50 ohm - 50 ohm transition.

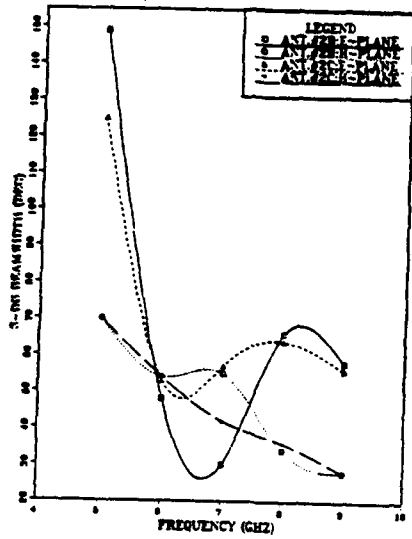


(A) 3-dB beamwidth

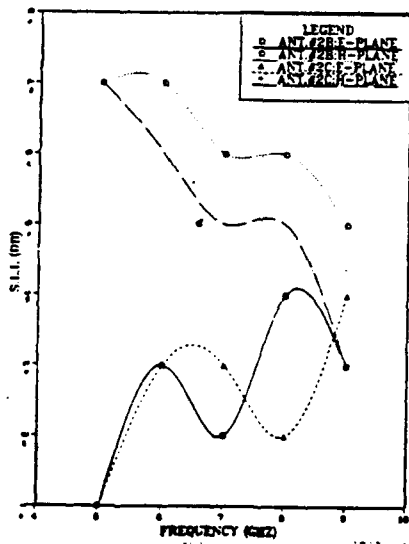


(B) Side lobe level

Figure 39. 3-dB beamwidth and side lobe level (S.L.L.) as a function of frequency: ($\epsilon_r = 6.0$ for antenna No.1B and No.1C)

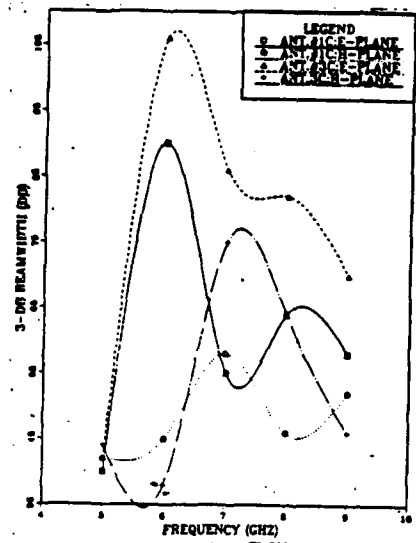


(A) 3-dB beamwidth

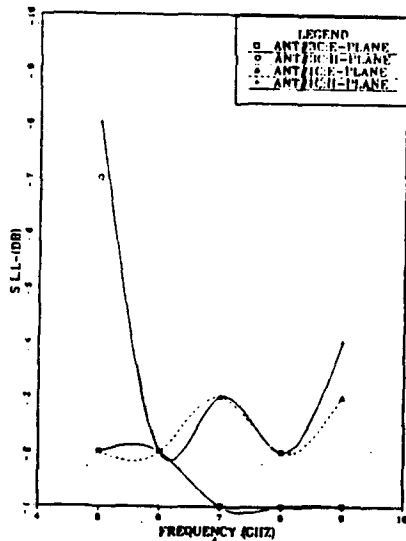


(B) Side lobe level

Figure 40. 3-dB beamwidth and side lobe level (S.L.L.) as a function of frequency: ($\epsilon_r = 2.33$ for antenna No.2B and No.2C)

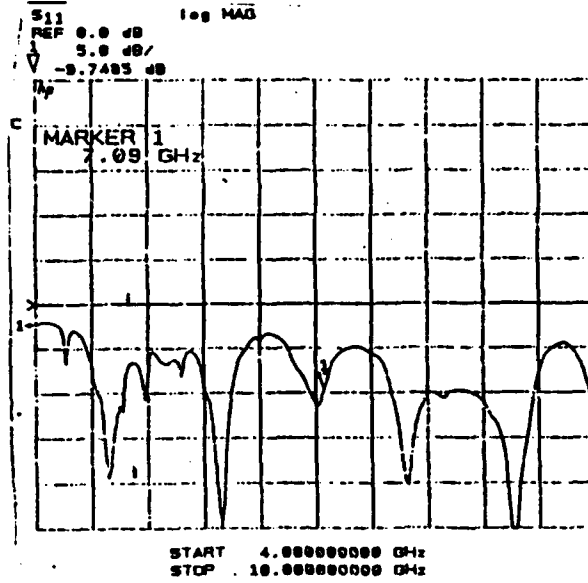


(A) 3-dB beamwidth

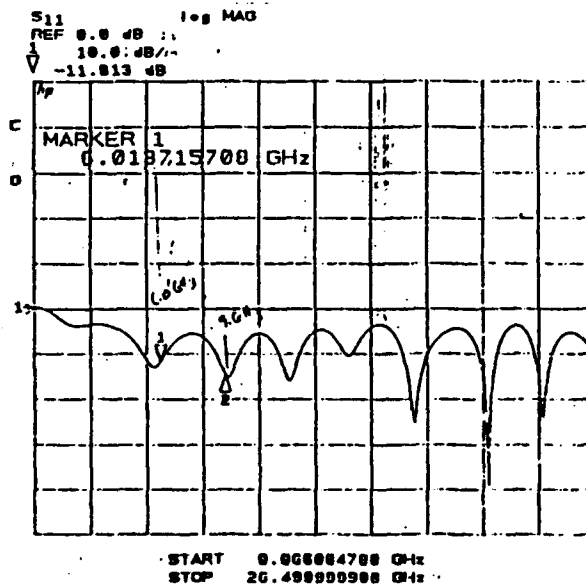


(B) Side lobe level

Figure 41. 3-dB beamwidth and side lobe level (S.L.L.) as a function of frequency: ($\epsilon_r = 6.0$ for antenna No.1C and No.3C)

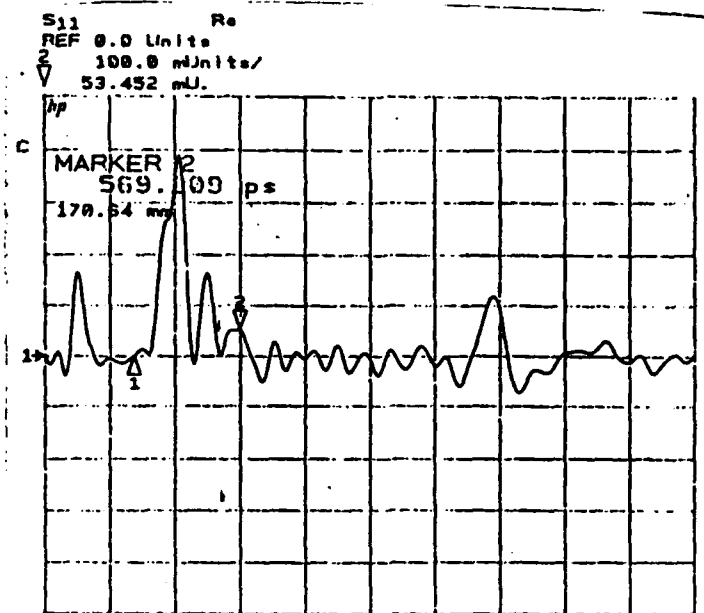


(A)

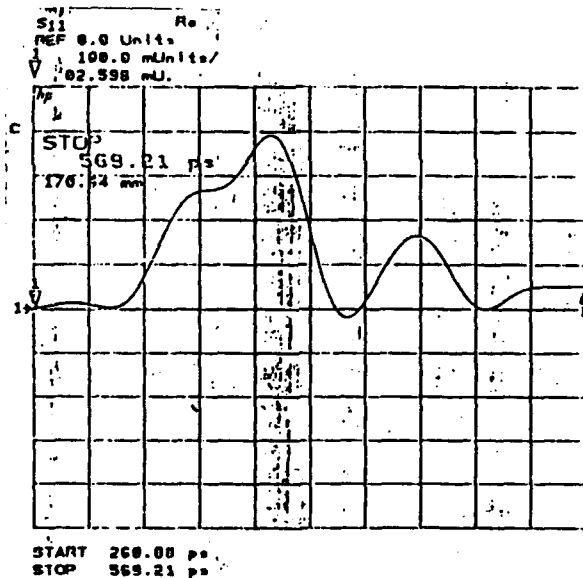


(B)

Figure 42. FDR plots for antenna No.3C: (A) Total return loss and (B) return loss due to junction alone



(A)



(B)

Figure 43. TDR plots for antenna No.3C: (A) Total return loss and (B) return loss due to junction alone

VI. SUMMARY AND CONCLUSION

A new mm-wave planar antenna, the Bilateral Slot Line (BSL) antenna, has been designed and tested. As expected, it behaved as an end-fire antenna with relatively narrow beamwidth, symmetric radiation pattern, and low return loss. Totally seven Linearly Tapered Slot and Bilateral Slot Line antennas were built and tested in order to investigate the near-field and far-field effects of changing substrate dielectric constant, antenna structure and Bilateral Slotline characteristic impedance. The LTSA's were built by linearly tapering the slotline over a length of 2λ , from the feed-end, so as to make the slotline width at the front-end equal to 0.4λ . The BSL antenna, consisting of a double-sided slotline, was fabricated by arranging together two identical LTSA's one on top of the other without any lateral displacement [Ref. 4].

The major design consideration, the feeding structure, has been studied and experimentally tested. A wideband feeding scheme has been designed to feed the LTSA and BSL antennas. In the case of BSL, the antennas were fed by a non-radiating stripline. A stripline-to-slotline transition scheme was fabricated on a low $\epsilon_r = 2.33$ and medium $\epsilon_r = 6.0$ dielectric constant and utilized throughout this work. Two different broadband stripline-to-slotline configurations were examined. The first utilized a 50 ohm stripline characteristic impedance to 70 ohm bilateral slotline characteristic impedance, and the second one used a 50 ohm stripline characteristic impedance to 50 ohm slotline characteristic impedance. Details of these transition schemes are given in Chapters 4 and 5. We saw in Chapter 3 that the use of bilateral slotline partially simplifies the difficulty related to fabricating narrow slot on low dielectric constant substrates [Ref. 4]. In the case of stripline, the ratio $\frac{W_{ST}}{2d}$ should be less than 1.0 in order to achieve a Z_{ST} in the range of 50 – 80 ohms.

We noted in Chapter 5 that using smaller ϵ_r improves antenna performance. Also, the extra substrate in front-end of the antenna increases the return loss compared to an antenna without the extra substrate.

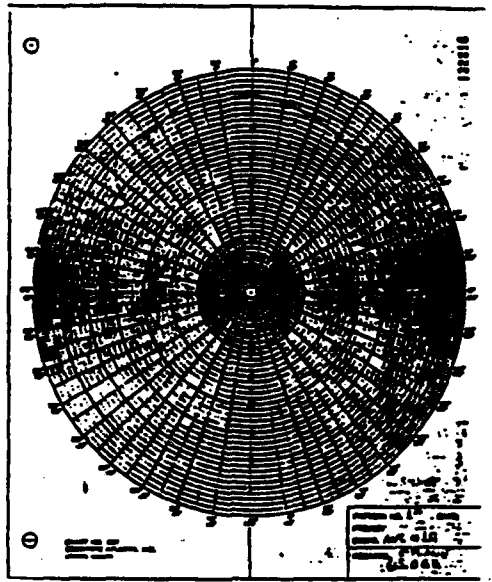
Lowest return loss was noticed in antenna No.2C where we had a wideband transition scheme ($Z_{ST} = 50$ ohms to $Z_{BSL} = 70$ ohms with $\epsilon_r = 2.33$). A low dielectric substrate simplifies the impedance matching problem at the junction and a 50 ohms stripline to 70 ohms bilateral slotline transition is suggested.

In general, comparing the three BSL antennas, No.1C, No.2C, and No.3C, the impedance matching is better in antenna No.2C ($Z_{ST} = 50$ ohms, $Z_{BSL} = 70$ ohms, $\epsilon_r = 2.33$), followed by No.1C ($Z_{ST} = 50$ ohms, $Z_{BSL} = 70$ ohms, $\epsilon_r = 6.0$) and then by No.3C ($Z_{ST} = Z_{BSL} = 50$ ohms, and $\epsilon_r = 6.0$).

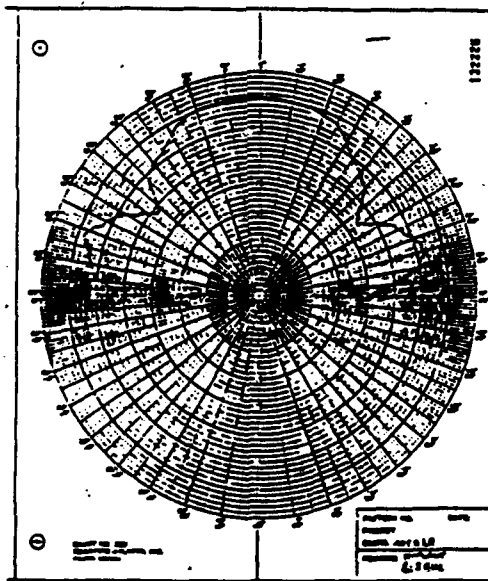
In the present work photolithographical method was used since it is economical and provides high accuracy. Helpful design data for stripline, slotline characteristic impedance, and effective dielectric constant were presented in Chapter 3. The design guidelines described can be used to design Tapered Slot or BSL antenna with any tapered shape.

APPENDIX A. LTSA AND BSL ANTENNA RADIATION PATTERNS

Figures were organized in such way so that each figure contains the E-plane and H-plane of same antenna for the same frequency. Figures 44-63 show obtained patterns for antenna No.1, Figs. 64-78 for antenna No.2, and Figs. 79-83 for antenna No.3.

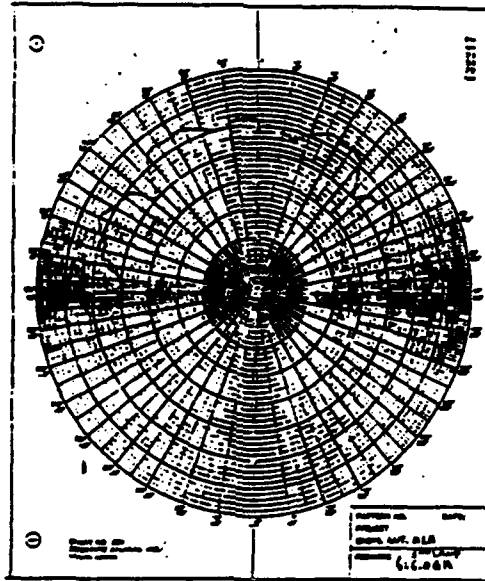


(A). E-plane

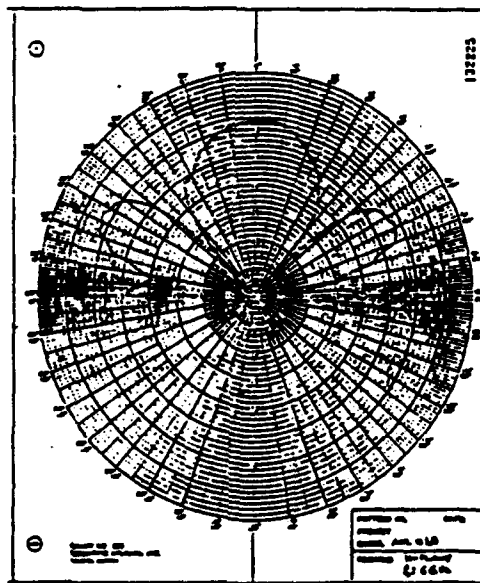


(B). H-plane

Figure 44. Radiation patterns of antenna No.1A at 5 GHz

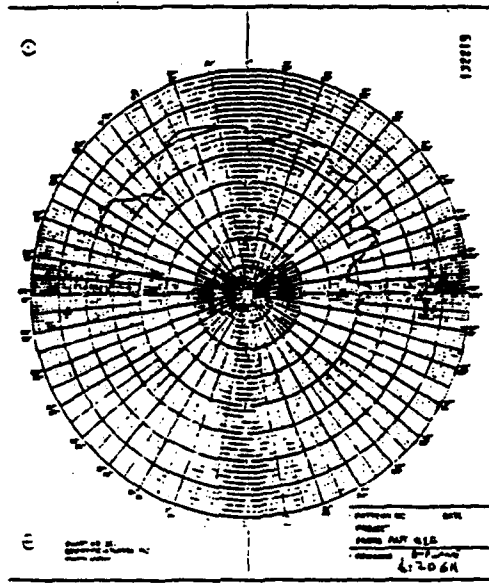


(A). E-plane

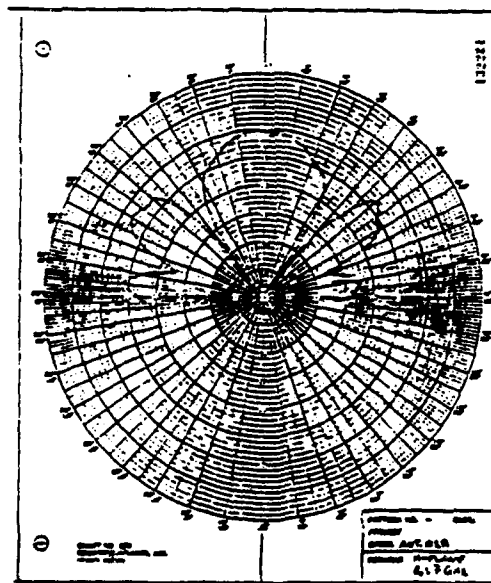


(B). H-plane

Figure 45. Radiation patterns of antenna No.1A at 6 GHz

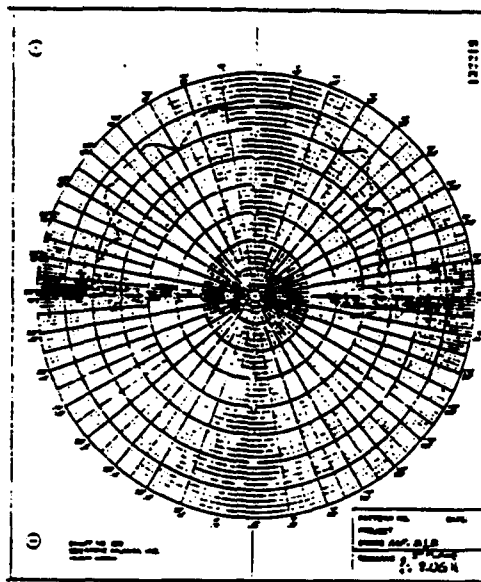


(A). E-plane

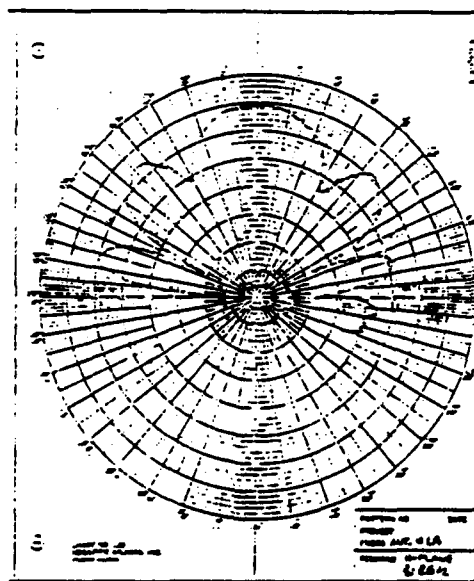


(B). H-plane

Figure 46. Radiation patterns of antenna No.1A at 7 GHz

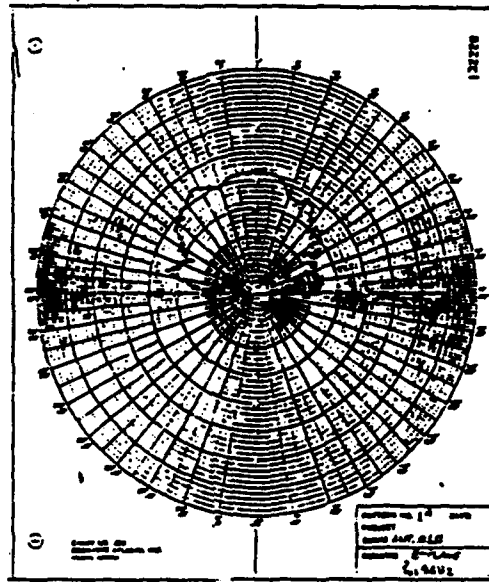


(A). E-plane

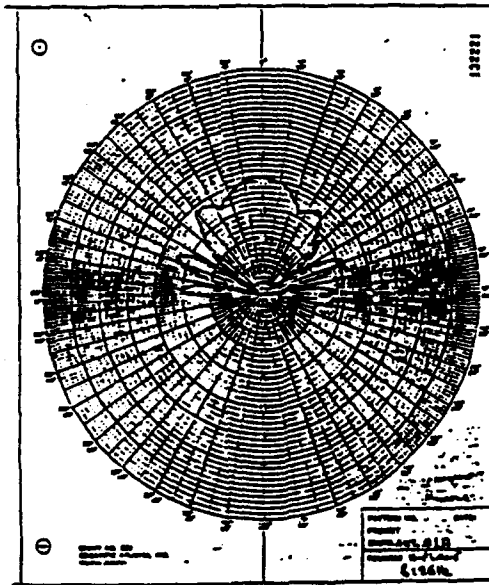


(B). H-plane

Figure 47. Radiation patterns of antenna No.1A at 8 GHz

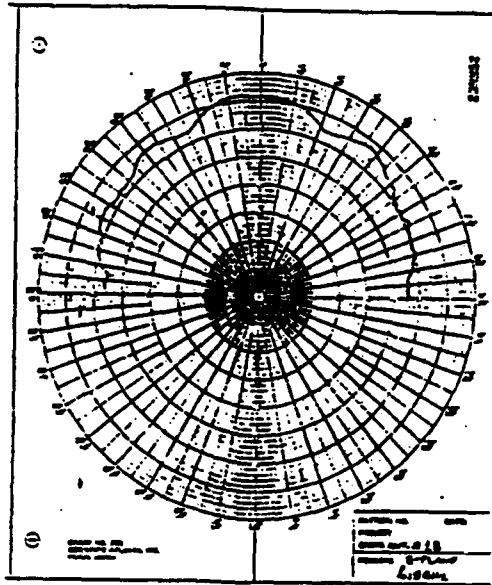


(A). E-plane

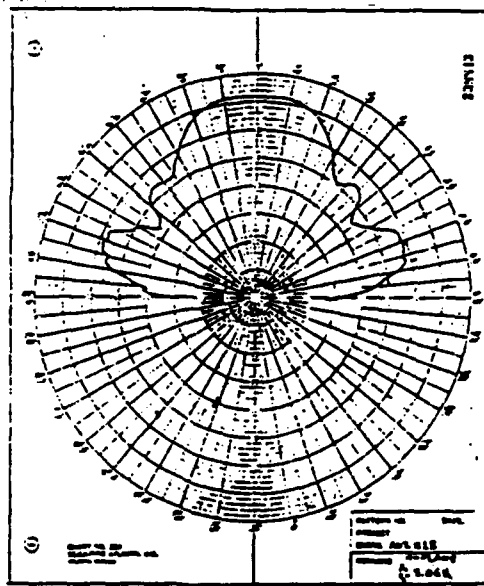


(B). H-plane

Figure 48. Radiation patterns of antenna No.1A at 9 GHz

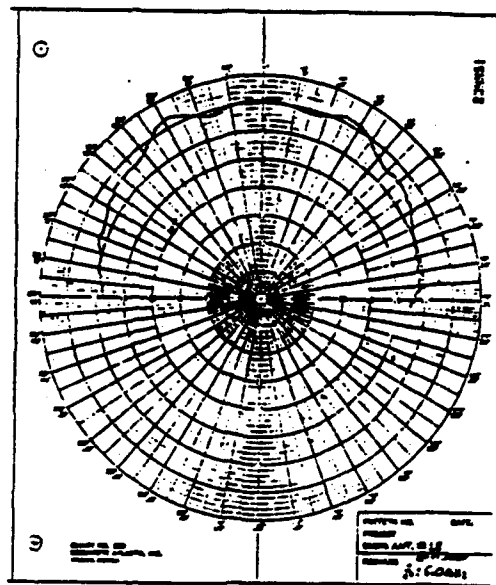


(A). E-plane

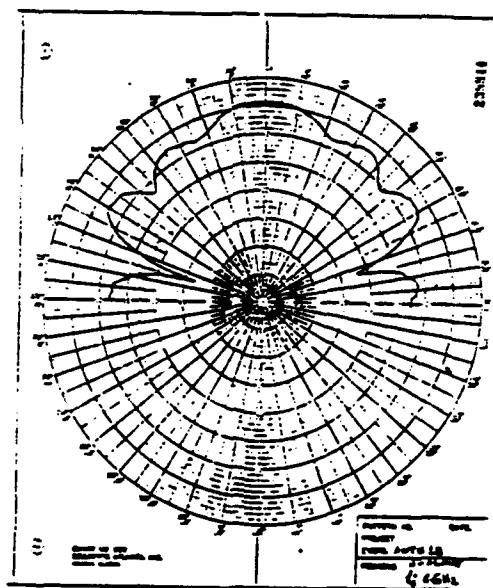


(B). H-plane

Figure 49. Radiation patterns of antenna No. 1B at 5 GHz

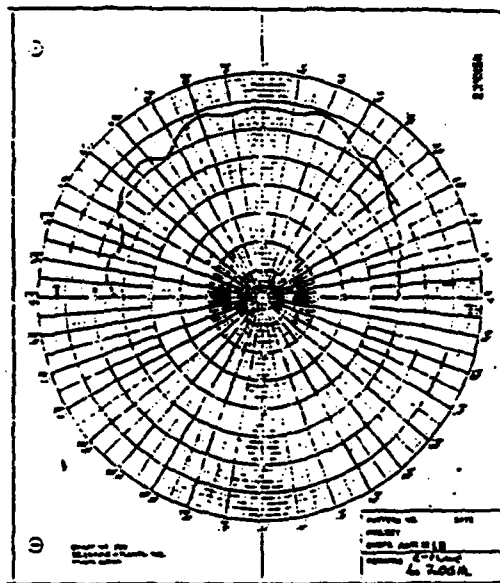


(A). E-plane

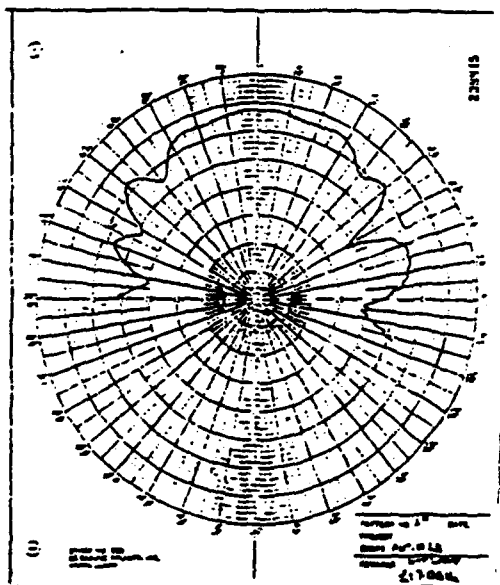


(B). H-plane

Figure 50. Radiation patterns of antenna No.1B at 6 GHz

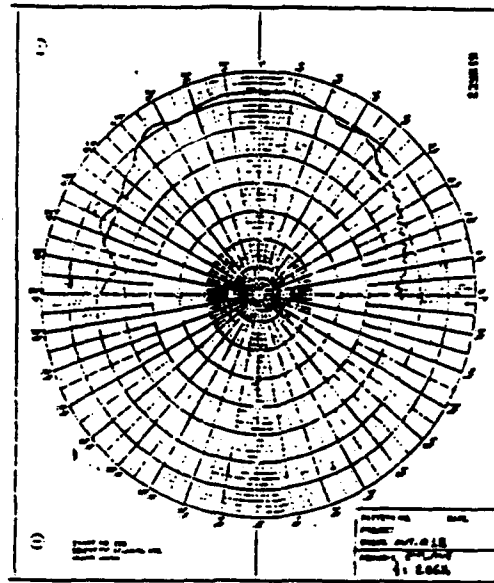


(A). E-plane

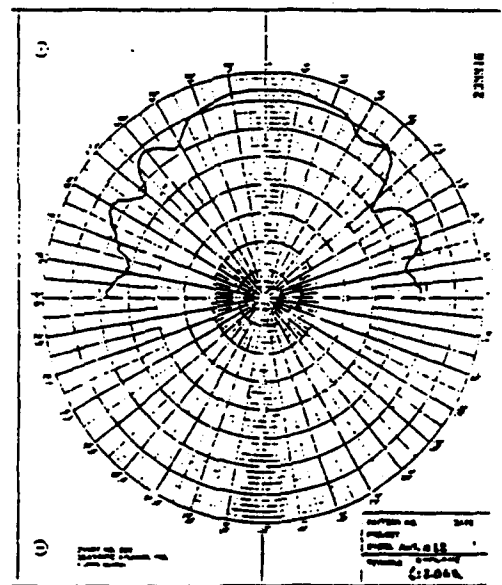


(B). H-plane

Figure 51. Radiation patterns of antenna No.1B at 7 GHz

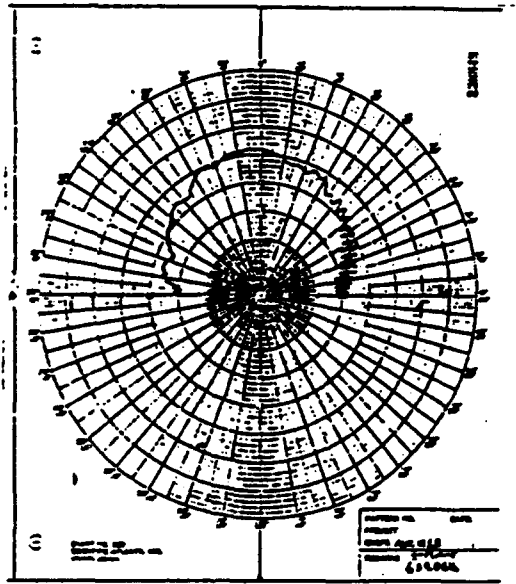


(A). E-plane

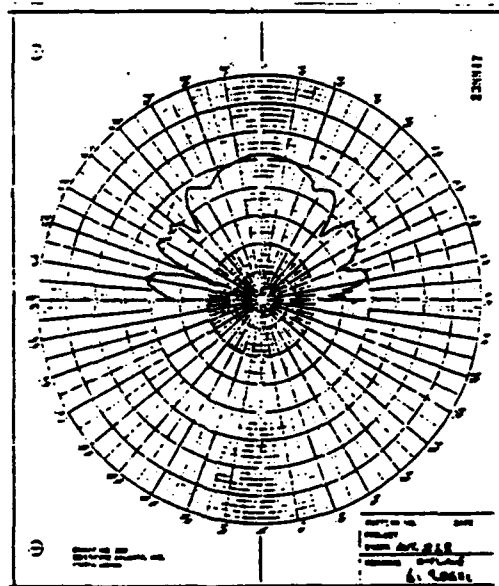


(B). H-plane

Figure 52. Radiation patterns of antenna No.1B at 8 GHz

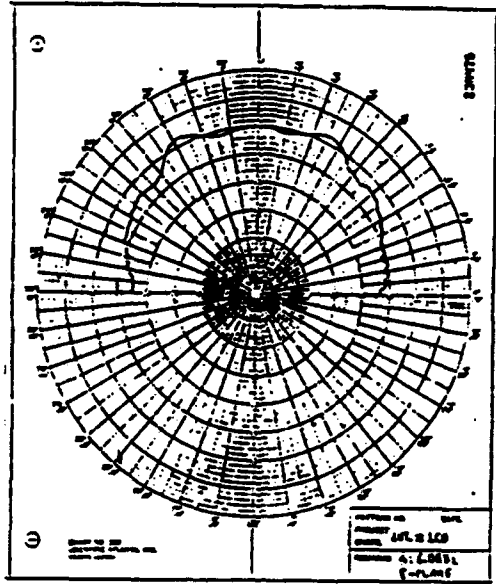


(A). E-plane

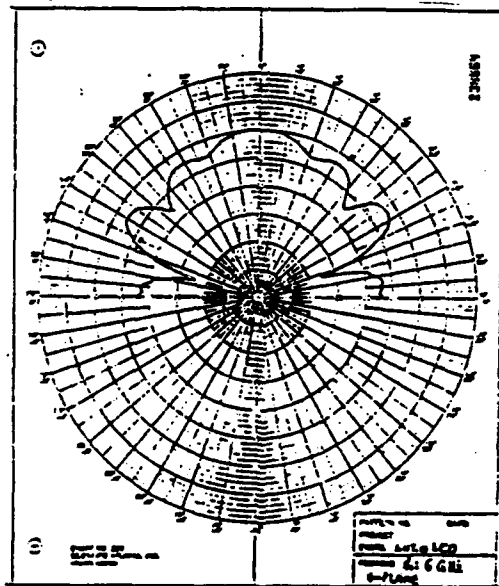


(B). H-plane

Figure 53. Radiation patterns of antenna No. 1B at 9 GHz

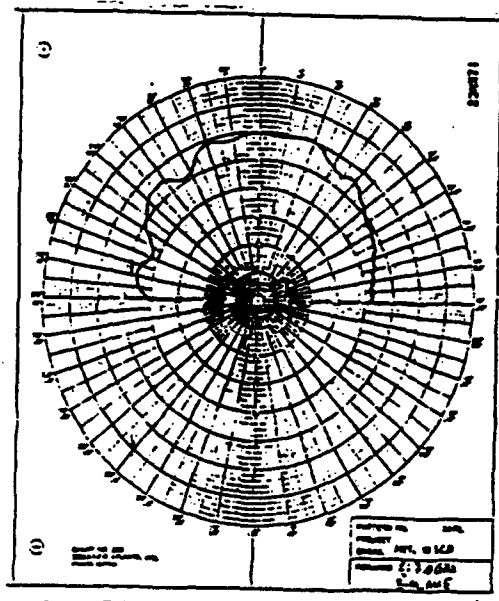


(A). E-plane

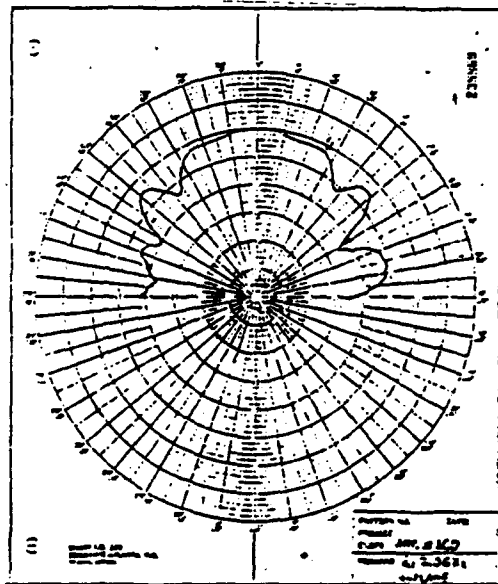


(B). H-plane

Figure 55. Radiation patterns of antenna No.1CO at 6 GHz

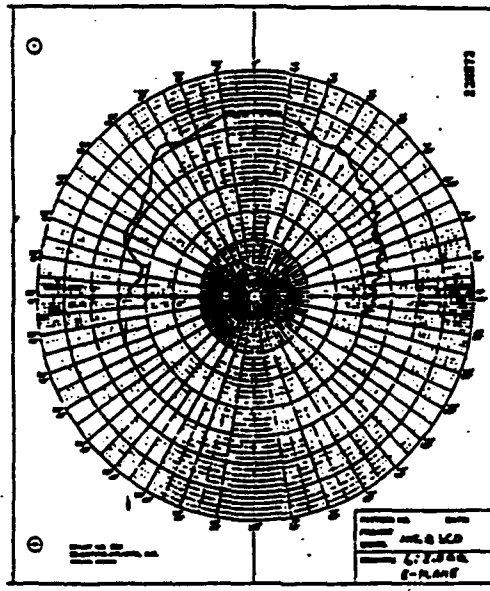


(A). E-plane

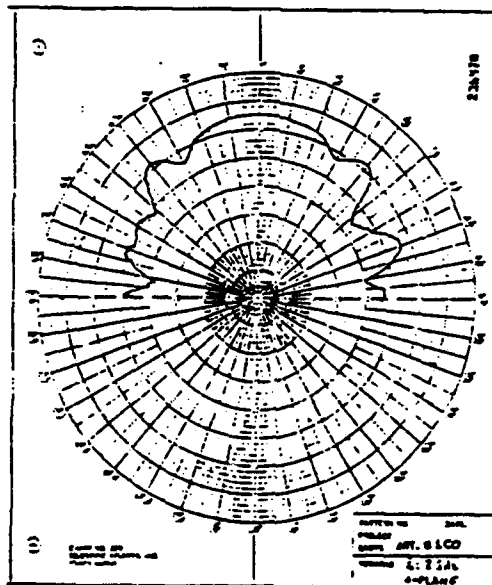


(B). H-plane

Figure 56. Radiation patterns of antenna No.1CO at 7 GHz

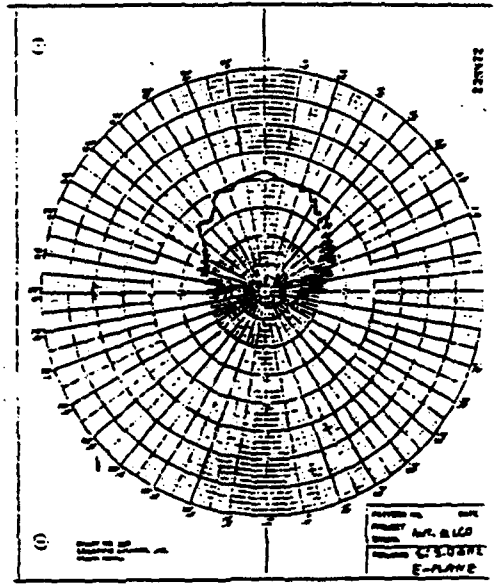


(A). E-plane

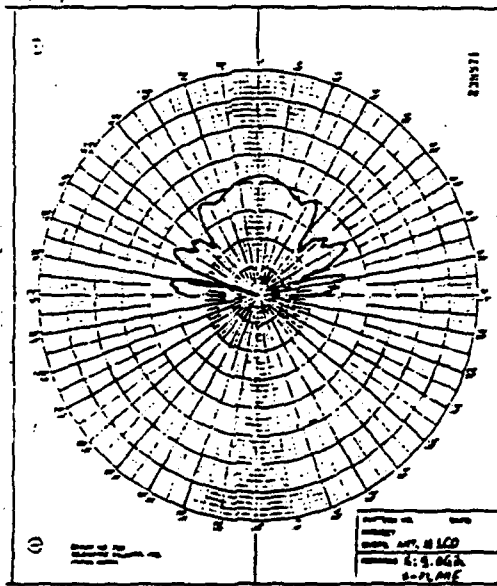


(B). H-plane

Figure 57. Radiation patterns of antenna No.1CO at 8 GHz



(A). E-plane



(B). H-plane

Figure 58. Radiation patterns of antenna No.1CO at 9 GHz

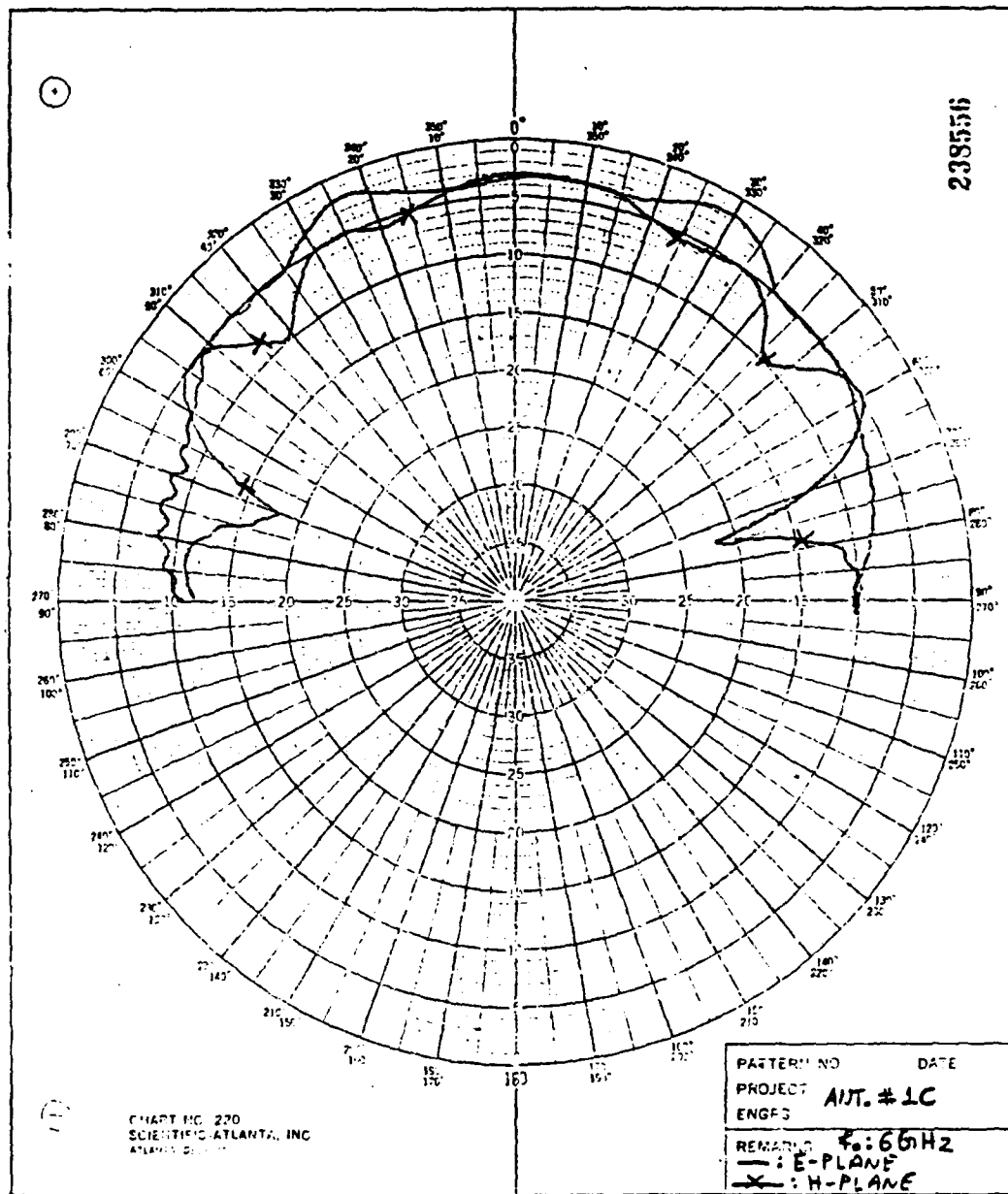


Figure 60. E-plane and H-plane radiation patterns of antenna No.1C at 6 GHz

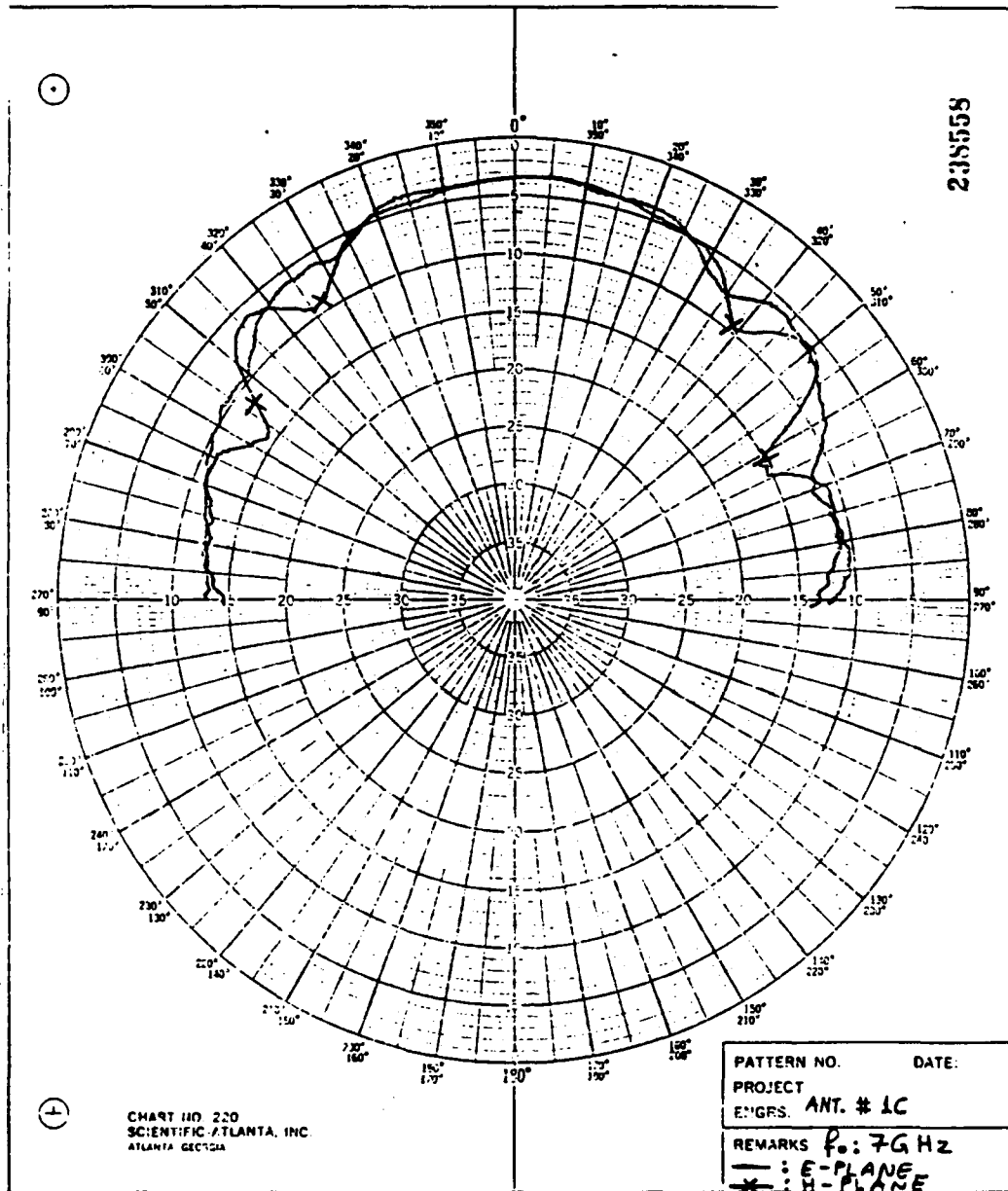


Figure 61. E-plane and H-plane radiation patterns of antenna No.1C at 7 GHz

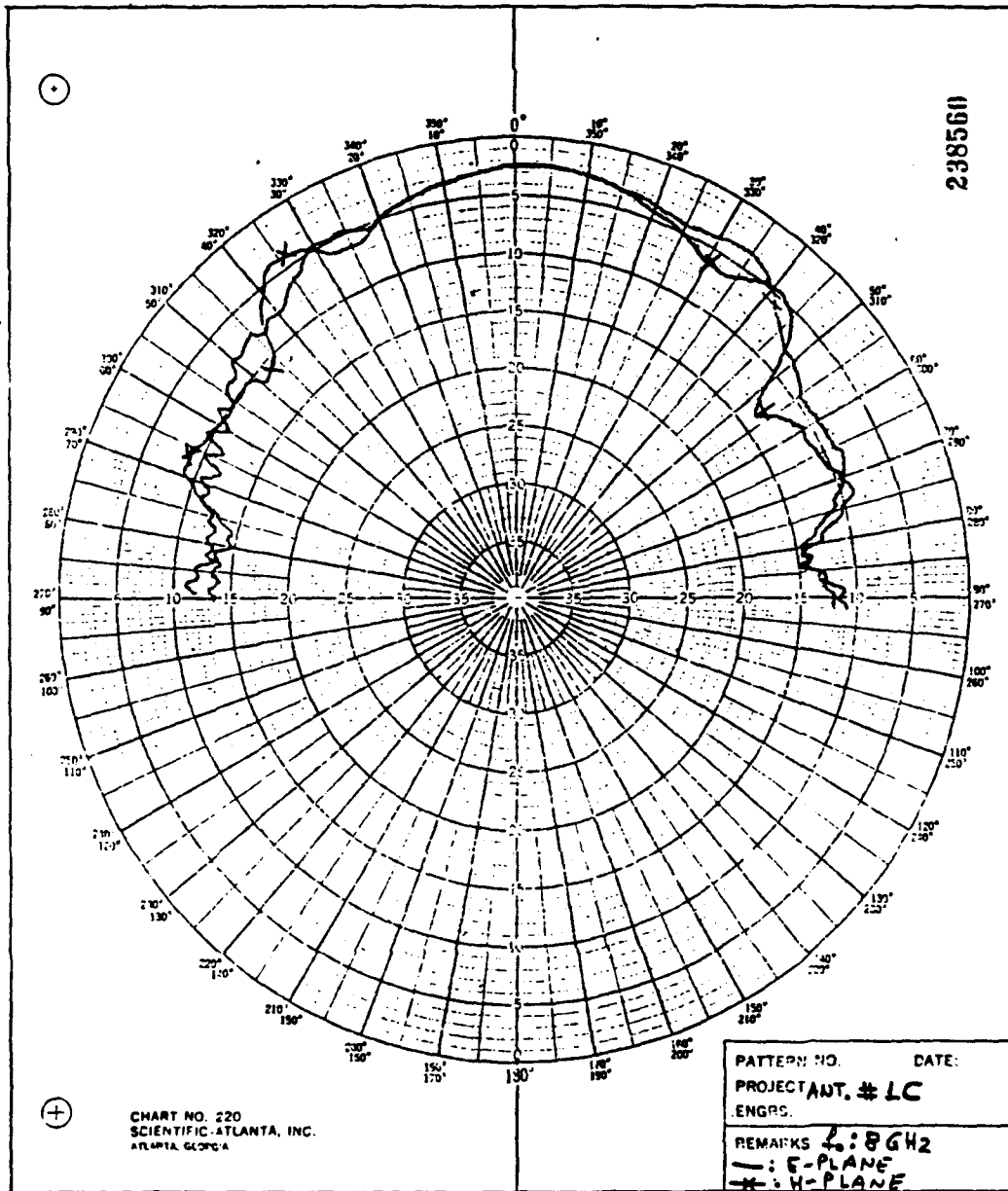


Figure 62. E-plane and H-plane radiation patterns of antenna No.1C at 8 GHz

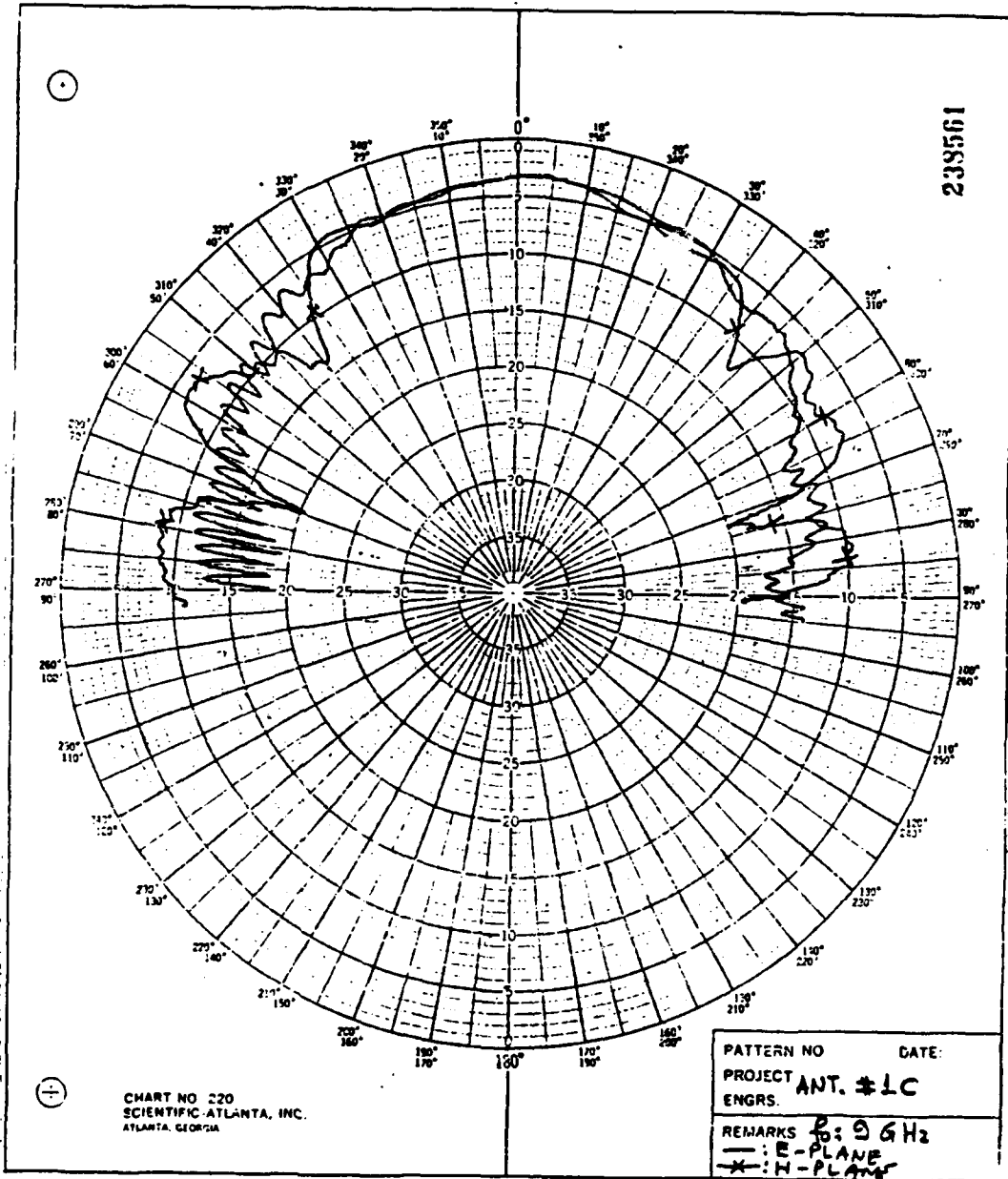
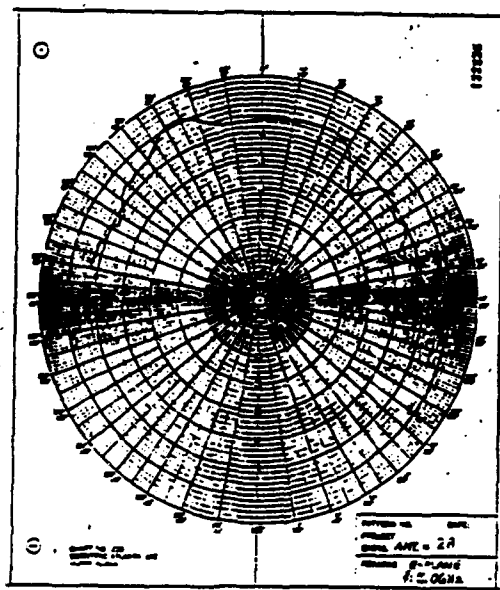
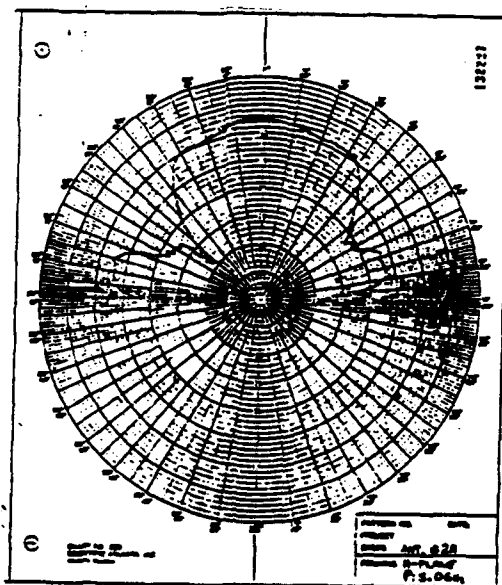


Figure 63. E-plane and H-plane radiation patterns of antenna No.1C at 9 GHz

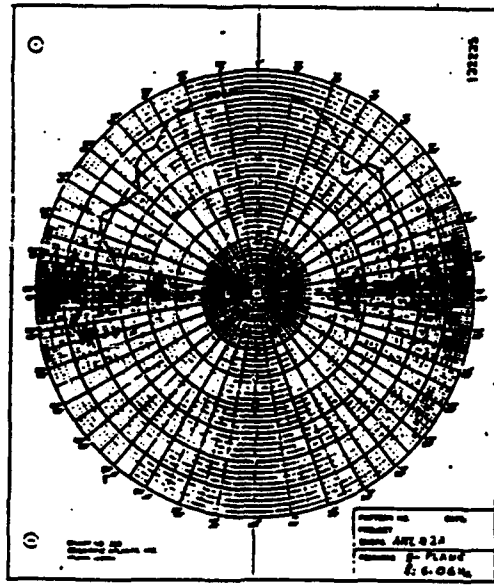


(A). E-plane

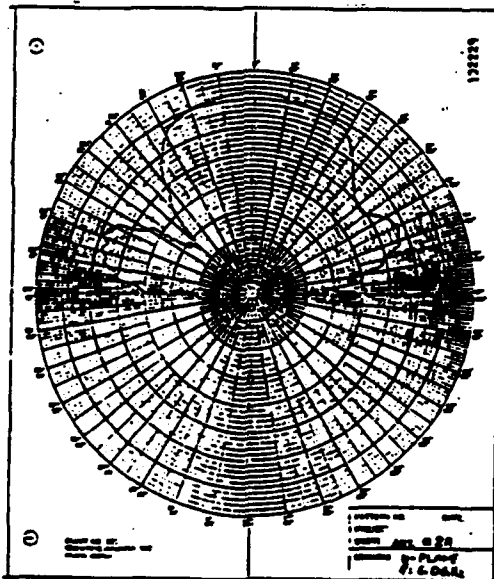


(B). H-plane

Figure 64. Radiation patterns of antenna No.2A at 5 GHz

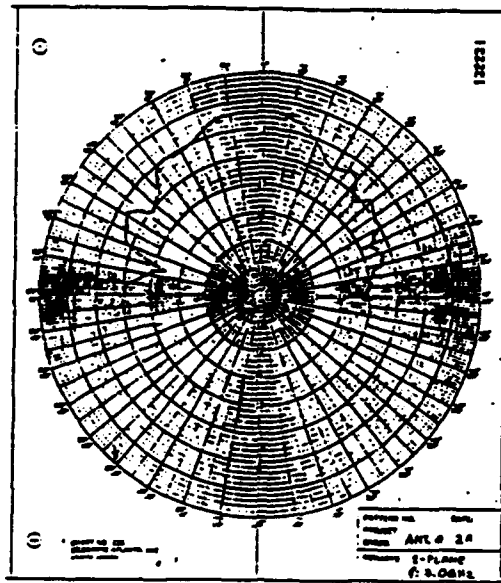


(A). E-plane

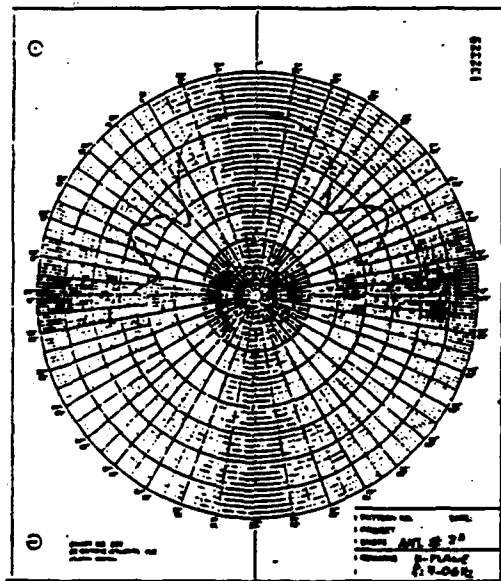


(B). H-plane

Figure 65. Radiation patterns of antenna No.2A at 6 GHz

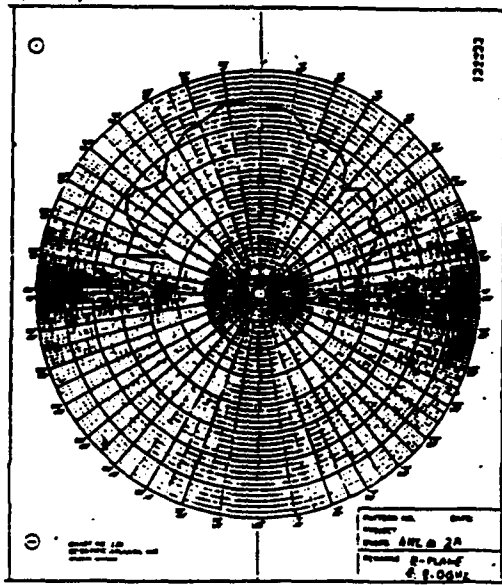


(A). E-plane

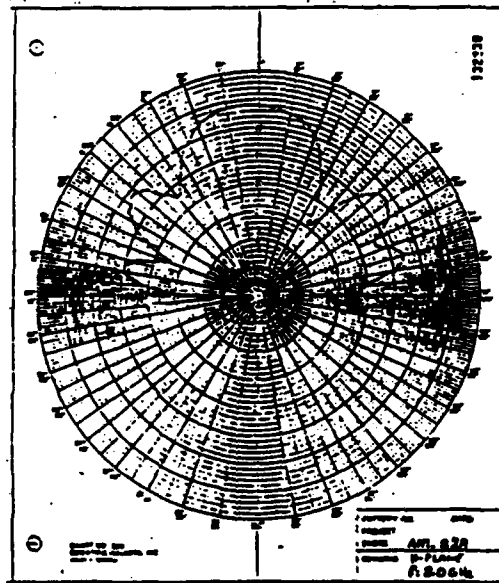


(B). H-plane

Figure 66. Radiation patterns of antenna No.2A at 7 GHz

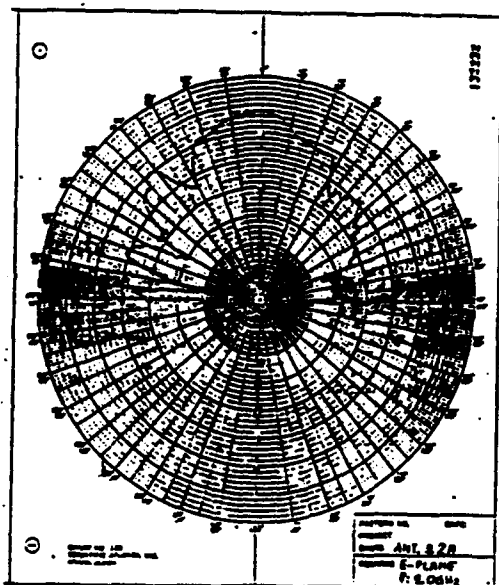


(A). E-plane

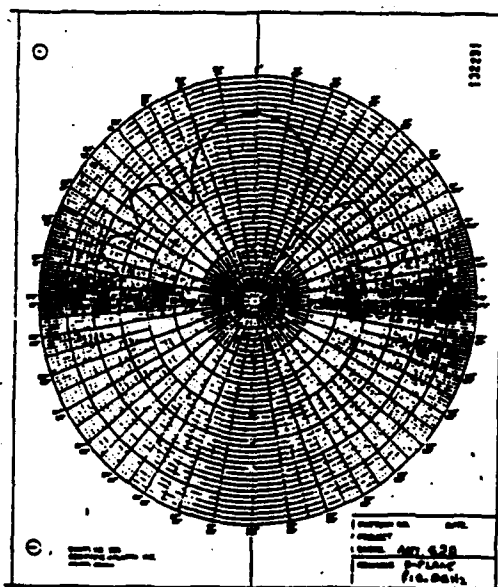


(B). H-plane

Figure 67. Radiation patterns of antenna No.2A at 8 GHz

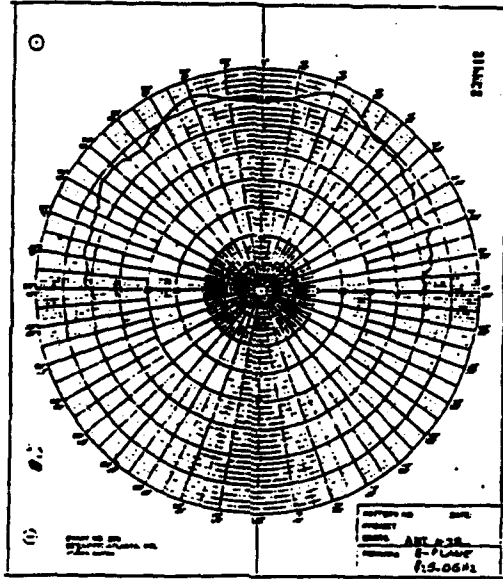


(A). E-plane

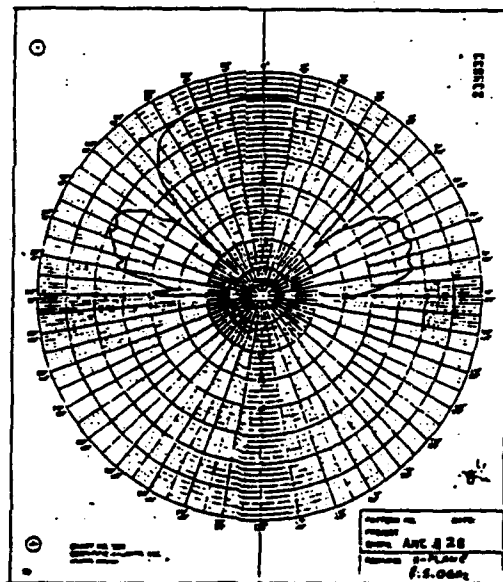


(B). H-plane

Figure 68. Radiation patterns of antenna No.2A at 9 GHz

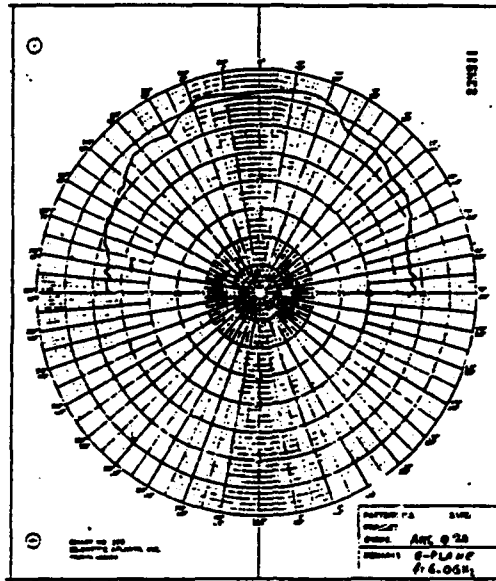


(A). E-plane

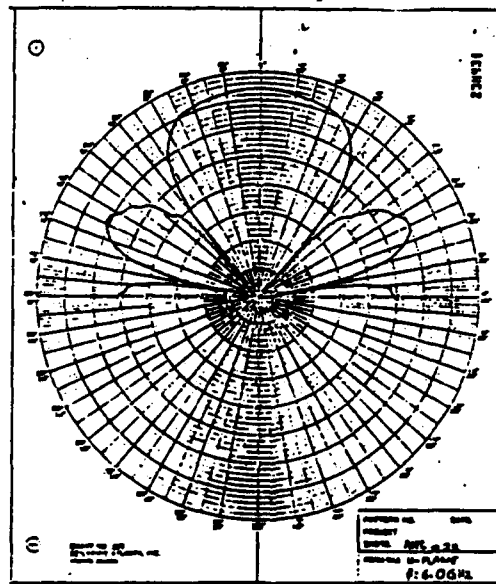


(B). H-plane

Figure 69. Radiation patterns of antenna No.2B at 5 GHz

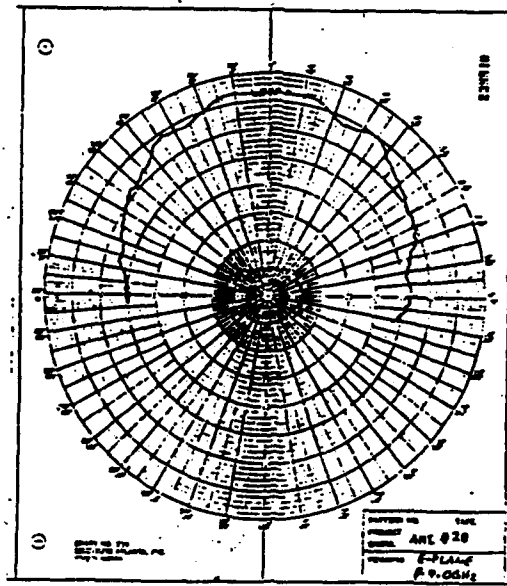


(A). E-plane

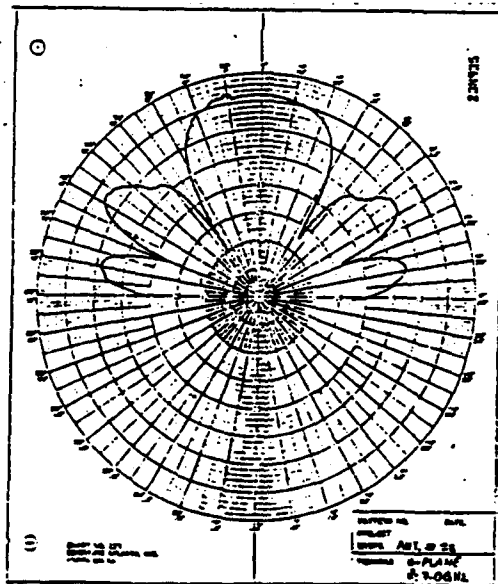


(B). H-plane

Figure 70. Radiation patterns of antenna No.2B at 6 GHz

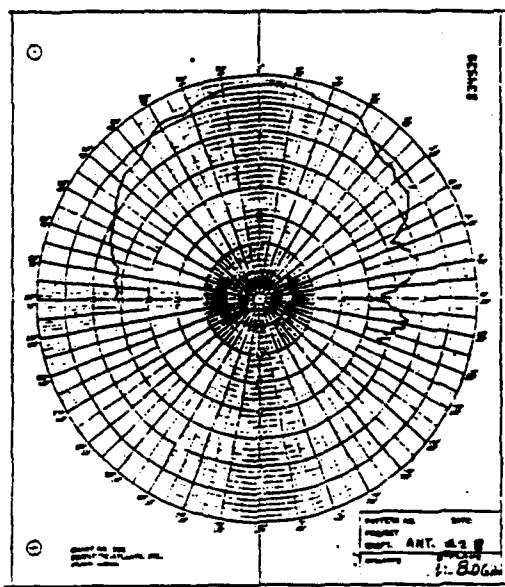


(A). E-plane

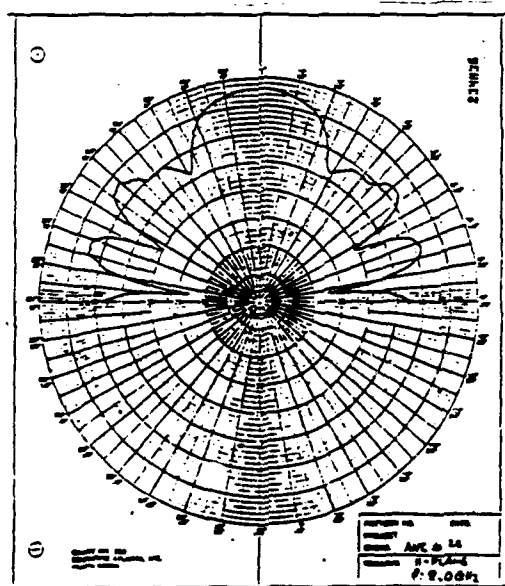


(B). H-plane

Figure 71. Radiation patterns of antenna No.2B at 7 GHz

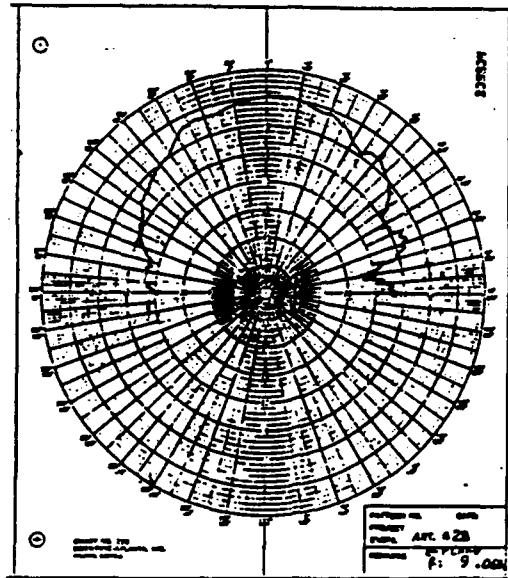


(A). E-plane

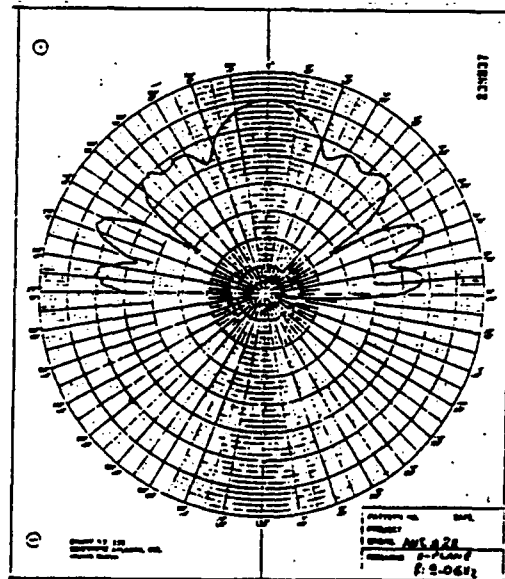


(B). H-plane

Figure 72. Radiation patterns of antenna No.2B at 8 GHz

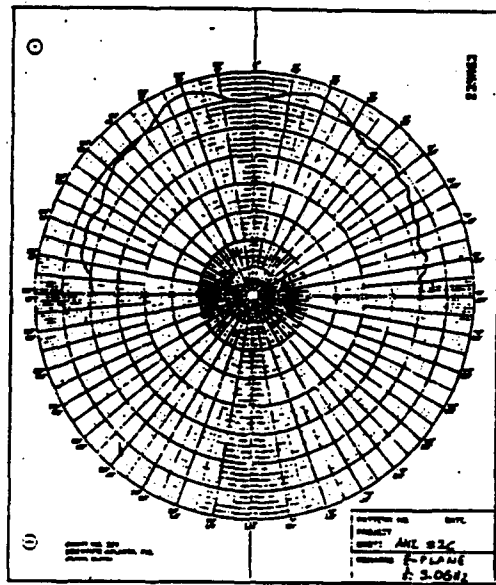


(A). E-plane

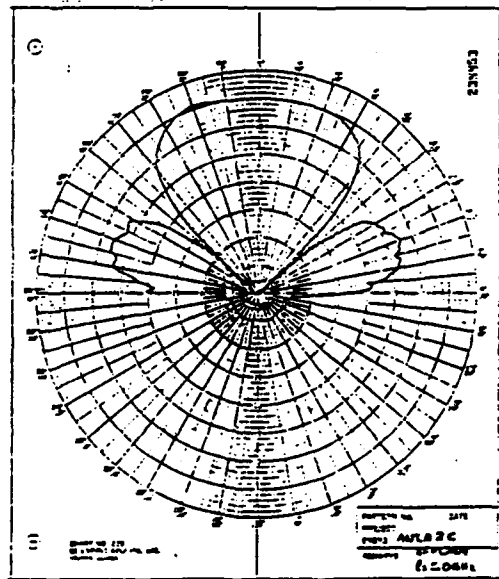


(B). H-plane

Figure 73. Radiation patterns of antenna No.2B at 9 GHz

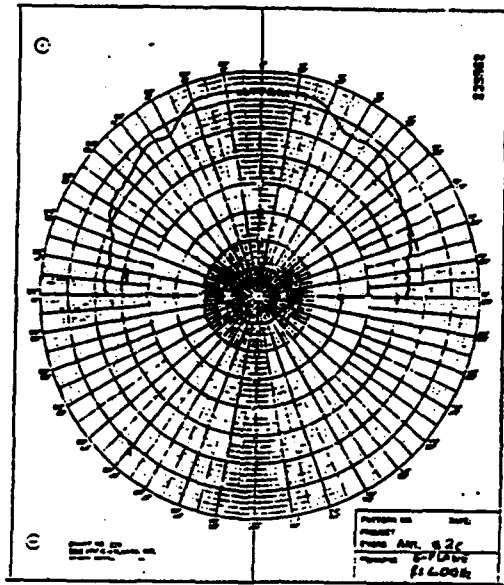


(A). E-plane

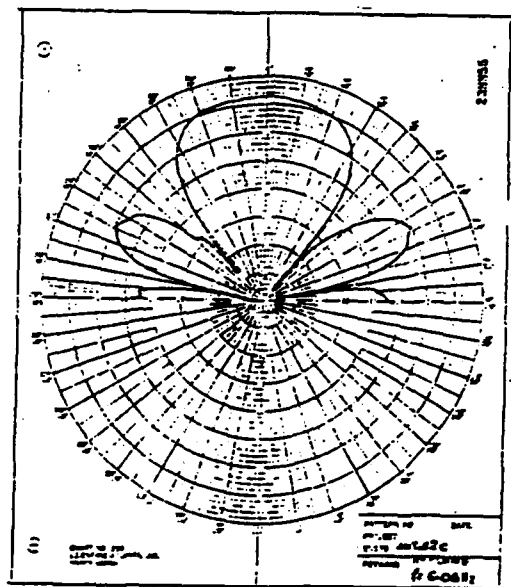


(B). H-plane

Figure 74. Radiation patterns of antenna No.2C at 5 GHz

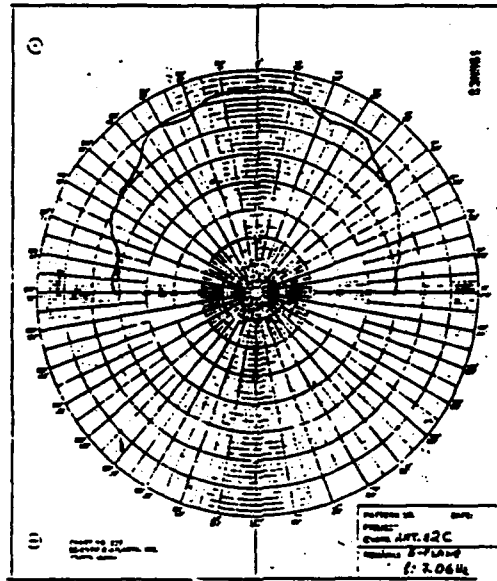


(A). E-plane

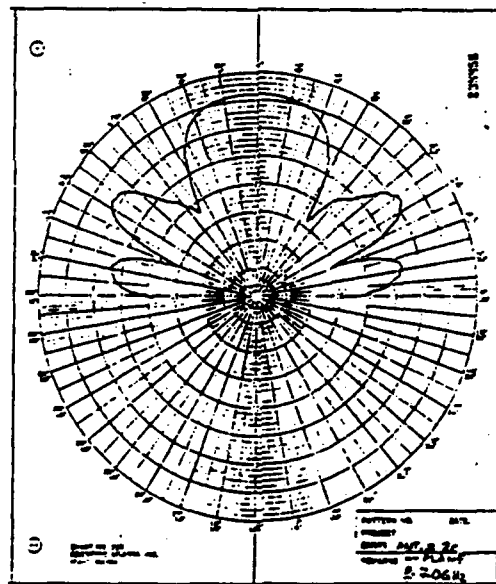


(B). H-plane

Figure 75. Radiation patterns of antenna No.2C at 6 GHz

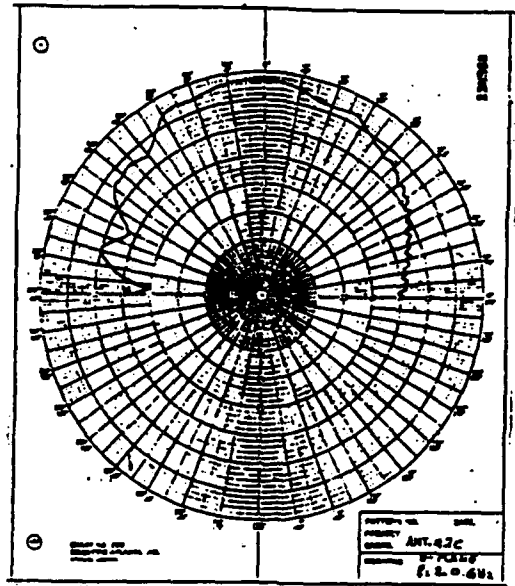


(A). E-plane

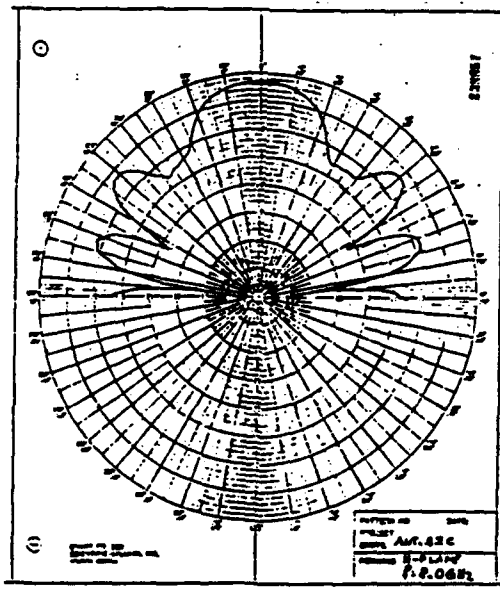


(B). H-plane

Figure 76. Radiation patterns of antenna No.2C at 7 GHz

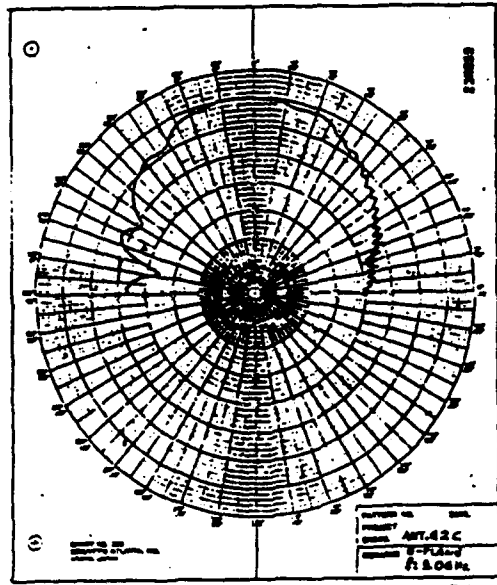


(A). E-plane

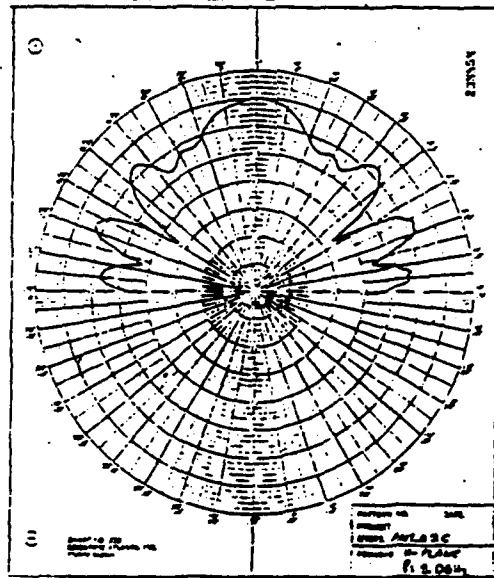


(B). H-plane

Figure 77. Radiation patterns of antenna No.2C at 8 GHz

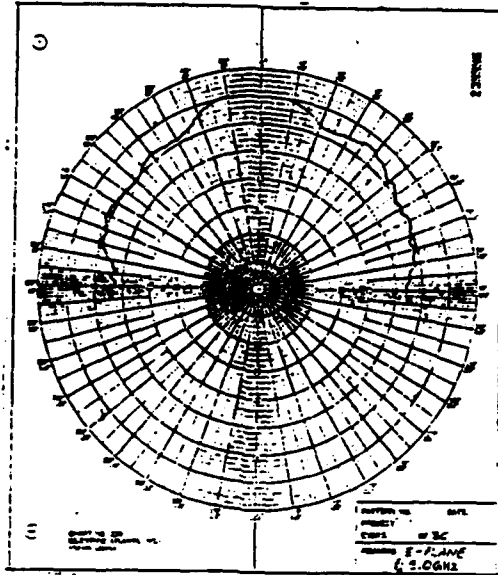


(A). E-plane

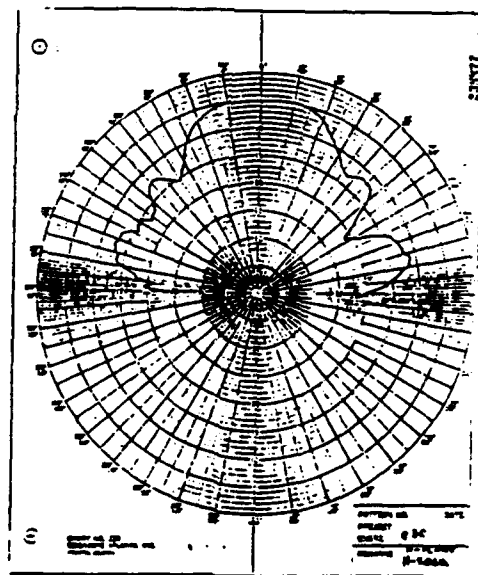


(B). H-plane

Figure 78. Radiation patterns of antenna No. 2C at 9 GHz

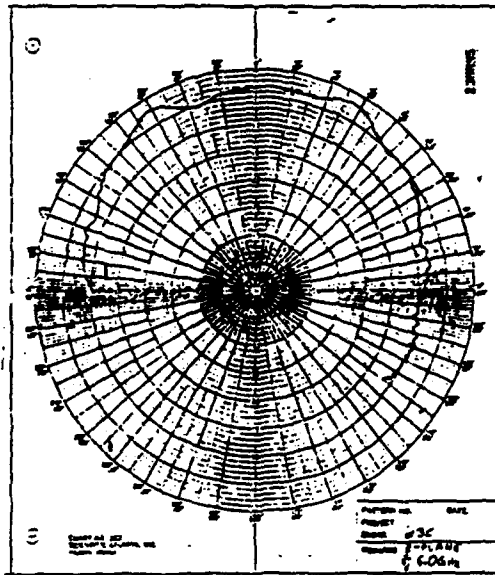


(A). E-plane

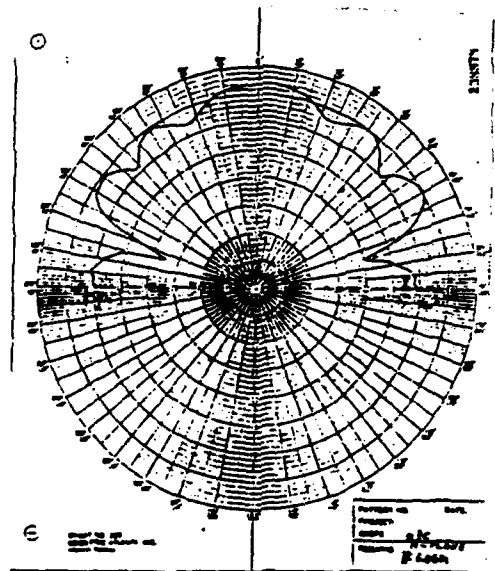


(B). H-plane

Figure 79. Radiation patterns of antenna No.3C at 5 GHz

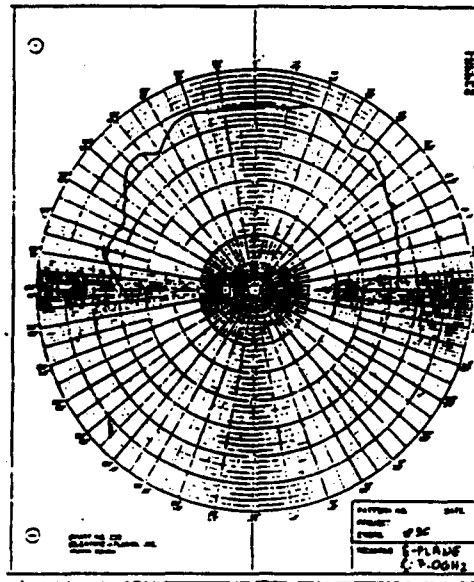


(A). E-plane

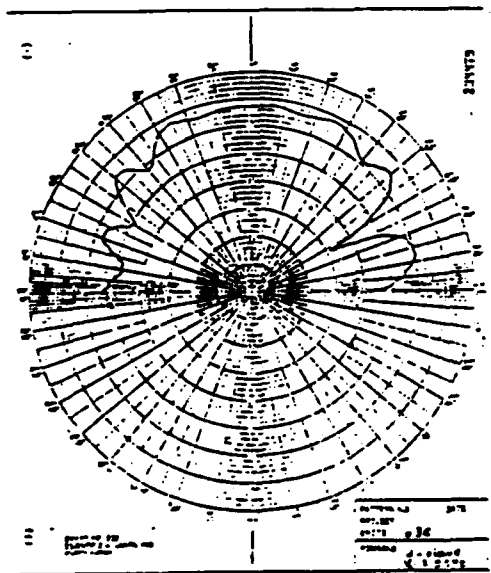


(B). H-plane

Figure 80. Radiation patterns of antenna No.3C at 6 GHz

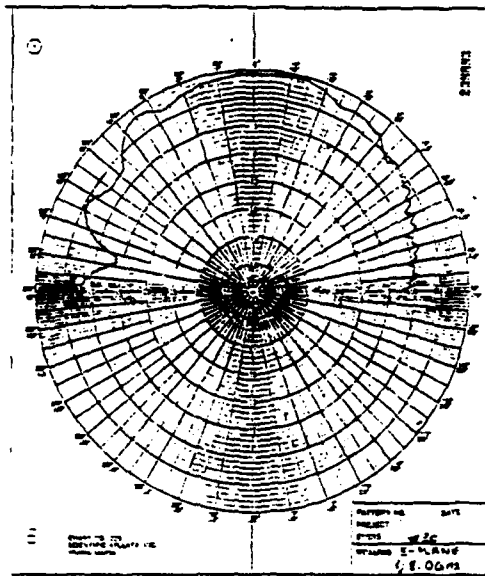


(A). E-plane

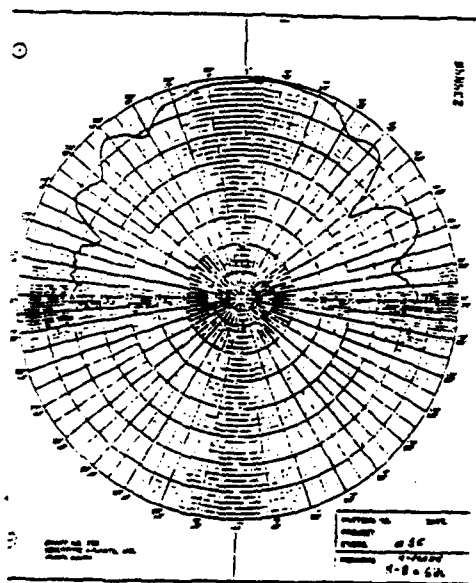


(B). H-plane

Figure 81. Radiation patterns of antenna No.3C at 7 GHz

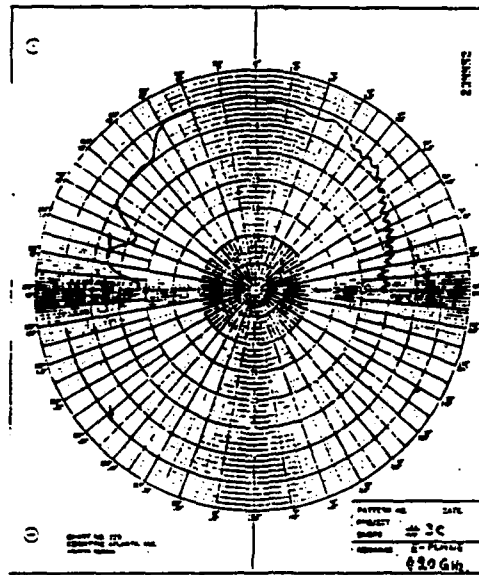


(A). E-plane

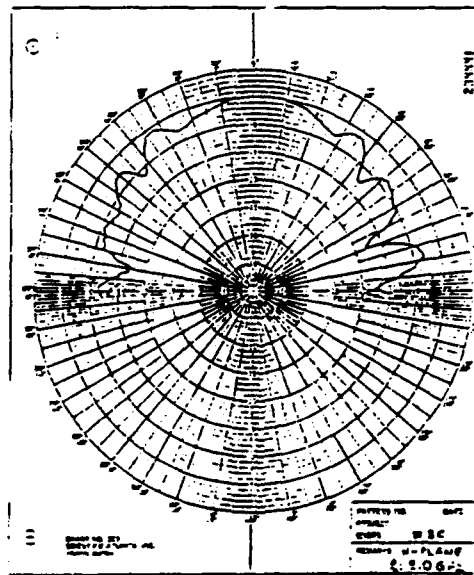


(B). H-plane

Figure 82. Radiation patterns of antenna No.3C at 8 GHz



(A). E-plane



(B). H-plane

Figure 83. Radiation patterns of antenna No.3C at 9 GHz

APPENDIX B. FORTRAN PROGRAM TO CALCULATE THE CHARACTERISTIC IMPEDANCE OF STRIPLINE

```

C$NOEXT
C   ** PURPOSE **
C   TO CALCULATE THE CHARACTERISTIC IMPEDANCE OF STRIPLINE
C   USING [Ref. 13]
C   **** VARIABLE DEFINITION ****
C   Zo: STRIPLINE CHARACTERISTIC IMPEDANCE
C   ER: SUBSTRATE DIELECTRIC CONSTANT
C   WD: STRIPLINE WIDTH OVER CONDUCTOR SPACING
C   K : k, AS IT IS GIVEN ON PAGE 10
C   K1: k', AS IT IS GIVEN ON PAGE 10
C   REAL PI,K,K1,ER,Zo,WD
C   PI=4*ATAN(1.0)
C   WRITE(4,10)
C   10 FORMAT(5X,'WD',12X,'Zo',12X,'ER',12X,'K')
C   FOR WD LESS THAN 1.0
C     DO 30 WD=.1,1.1,.1
C1  FOR WD BIGGER THAN 1.0) AND LESS OR EQUAL THAN 10.0
C1  DO 30 WD=1,10
C     DO 30 ER=2,10
C     K1=TANH(PI*WD/2)
C     K=SECH(PI*WD/2)
C     K=SQRT(1-K1**2)
C     WRITE(4,*) K
C   IF (K.GE.0. AND.K.LT.0.7)THEN
C     ZO=30.*(PI**2)/(SQRT(ER)*ALOG(2.*(1.+SQRT(K1))/(1.-SQRT(K1))))
C     WRITE(4,20) WD,ZO,ER,K1
C     WRITE(4,20) ER,ZO,WD,K
C   ELSE IF(K.GT.0.7.AND.K.LE.1) THEN
C     ZO=30.*ALOG(2.*(1.+SQRT(K))/(1.-SQRT(K)))*(SQRT(ER)**(-1.))
C     WRITE(4,20) WD,ZO,ER,ER
C     WRITE(4,20) ER,ZO,WD,K1
C   20 FORMAT(5X,4(F14.7))
C   END IF
C   30 CONTINUE
C   40 CONTINUE
C     STOP
C     END

```

LIST OF REFERENCES

1. S.N. Prasad and S. Mahapatra, *A New MIC Slot-Line Aerial*, IEEE Trans. on Antennas and Propag., Vol. AP-31, No. 3, pp. 525-527, May 1983.
2. K.S. Yngvesson, D.H. Schaubert, T.L. Korzeniowski, E.L. Kollberg, T. Thungren and J.F. Johansson, *Endfire Tapered Slot Antennas on Dielectric Substrates*, IEEE Trans. on Antennas and Propag., Vol. AP-33, No. 12, pp. 1392-1399, December 1985.
3. K.S. Yngvesson, T.L. Korzeniowski, Y.S. Kim, E. L. Kollberg and J.F. Johansson, *The Tapered Slot Antenna -A New Integrated Element for Millimeter-wave Application*, IEEE Trans. on Microwave Theory and Techn., Vol. 37, No. 2, pp. 365-374, February 1989.
4. R. Janaswamy, *Even Mode Characteristic of Bilateral Slotline*, to appear in IEEE Trans. on Microwave Theory and Tech., June 1990.
5. J.D. Dyson, *The Equiangular Spiral Antenna*, IRE Trans. Antennas and Propag., Vol. 7, pp. 181-187, April 1959.
6. U. Kotthaus and B. Vowinkel, *Investigation of Planar Antennas for Submillimeter Receivers*, IEEE Trans. on Microwave Theory and Tech., Vol. 37, No. 2, pp. 375-380, February 1989.
7. P.J. Gibson, *The Vivaldi Aerial*, Proc. of 9th European Microwave Conf. (Brighton, U.K.), pp. 101-105, 1979.
8. R. Janaswamy and D.H. Schaubert, *Analysis of the Tapered Slot Antenna*, IEEE Trans. Antennas and Propag., Vol. AP-35, No. 9, pp. 1058-1065, September 1987.
9. T. Thungren, E.L. Kollberg and K.S. Yngresson, *Vivaldi Antenna for Single Beam Integrated Receivers*, 12th Eur. Microwave Conference, Helsinki, 1982.

10. G.H. Robinson and J.L. Allens, *Slotline Application to Miniature Ferrite Devices*, IEEE Trans. on Microwave Theory and Tech., Vol. MTT-17, pp. 1097-1101, December 1969.
11. R. Carel, *The Characteristic Impedance of Two Infinite Cones of Arbitrary Cross-Section*, IRE Trans. on Antennas and Propag., Vol. AP-6, No. 2, pp. 197-201, 1958.
12. I.J. Bahl and R. Garg, *A Designer's Guide to Stripline Circuits*, Microwaves, pp. 90-96, January 1978.
13. S.B. Cohn, *Characteristic Impedance of Shielded Strip Transmission Line*, IEEE Trans. on Microwave Theory and Tech., Vol. MTT-2, pp. 52-55, July 1954.
14. M. Abramovitz and I.A. Stegun, *Handbook of Mathematical Functions*, Dover publication, Inc., New York 1970.
15. R. Janaswamy, *Moment Method for Bilateral Slotline*, Unpublished notes, Naval Postgraduate School, 1989.
16. A. Erdelyi (Editor), *Tables of Integral Transforms*, McGraw-Hill, New York, 1954.
17. I.S. Gradshteyn and I.M. Ryzhik, *Tables of Integrals, Series, and Products*, Academic Press Inc., Florida, 1980.
18. T.L. Korzeniowski, D.H. Schaubert and K.S. Yngvesson, *Imaging System at 94 GHz Using Tapered Slot Antenna Elements*, presented at 8th International Conf. on Infrared and mm Waves, Miami, December 1983.
19. H. Howe, Jr, *Stripline Circuits Design*, Microwave Associates, Burlington, Mass. Artech House, Dedham, Massachusetts 1973.
20. J.S. Jeong, *An Evaluation of Coplanar Line for Application in Microwave Integrated Circuitry*, Master's thesis, Naval Postgraduate School, Monterey, California, December 1988.

INITIAL DISTRIBUTION LIST

	No. Copies
1. Defense Technical Information Center Cameron Station Alexandria, VA 22304-6145	2
2. Library, Code 0142 Naval Postgraduate School Monterey, CA 93943-5002	2
3. Chairman, Code EC Naval Postgraduate School Department of Electrical and Computer Engineering Monterey, CA 93943-5000	1
4. Chairman, Code MA Naval Postgraduate School Department of Mathematics Monterey, CA 93943-5000	1
5. Director, Research Administration, Code 012 Naval Postgraduate School Monterey, CA 93943-5000	1
6. R. Janaswamy, Code EC/Js Naval Postgraduate School Monterey, CA 93943-5000	4
7. B. Neta, Code MA/Nd Naval Postgraduate school Monterey, CA 93943-5000	1
8. Mr J. Mosko, Code 35203 RF Development Division Naval Weapons Center China Lake, CA 93555	1
9. Georgios Lambrakakis Faidonos 36 Agios Dimitrius 172 36 Athens, Greece	4
10. Embassy of Greece Naval Attache 2228 Massachusetts Ave., N.W. Washington, D.C. 20008	5

11. Mr. E. Papatiriu 1
SMC-2725
Naval Postgraduate School
Monterey, CA 93943-5000
12. Mr. C.B. Cameron 1
1139 Leahy Rd.
Monterey, CA 93940-4813
13. Mr. S. Konidaris 1
SMC-1788
Naval Postgraduate School
Monterey, CA 93943-5000
14. Mr. Seo, Yong Seok 1
975-17 Bangbae 2 Dong Kangnamgu
Seoul
KOREA
15. Mr. G.F. Mikucki 1
Government Electronic System Division
General Electric Company
Moorestown, NJ 08057